The Effect of Microstructural Defects and Geometrical Features on Fatigue Behavior of Superelastic Nitinol Wires

Parisa Shabani Nezhad
Marquette University

Recommended Citation

Shabani Nezhad, Parisa, "The Effect of Microstructural Defects and Geometrical Features on Fatigue Behavior of Superelastic Nitinol Wires" (2023). *Dissertations (1934 -)*. 3030.
https://epublications.marquette.edu/dissertations_mu/3030

THE EFFECT OF MICROSTRUCTURAL DEFECTS AND GEOMETRICAL FEATURES ON FATIGUE BEHAVIOR OF SUPERELASTIC NITINOL WIRES

by:

Parisa Shabani Nezhad

A Dissertation submitted to the Faculty of the Graduate School,
Marquette University,
in Partial Fulfillment of the Requirements for
the Degree of Doctor of Philosophy

Milwaukee, Wisconsin

August 2023

ABSTRACT

THE EFFECT OF MICROSTRUCTURAL DEFECTS AND GEOMETRICAL FEATURES ON FATIGUE BEHAVIOR OF SUPERELASTIC NITINOL WIRES

Parisa Shabani Nezhad

Marquette University, 2023

Nitinol is an alloy of nickel and titanium, which exhibits outstanding functional properties, such as shape memory and superelastic behavior. Superelastic nitinol wires exhibit recoverable strains that are significantly greater than traditional alloys. In most of its applications, nitinol is exposed to cyclic loads, which results in functional and/or structural fatigue that ultimately leads to failure. The classical fatigue theories do not appropriately address the fatigue performance of superelastic nitinol due to the complex nature of the martensitic transformation. It has been shown that the main fatigue crack initiation sites, other than surfaces, are microstructural inhomogeneities such as voids and non-metallic inclusions. The effect of wire size on fatigue performance of superelastic nitinol is not clearly understood. In this research, nitinol wires with three different sizes are subjected to microstructural analysis and low-cycle fatigue tests to understand the effect of wire size on their phase transformations and fatigue life. For this purpose, advanced non-destructive characterization techniques such as X-ray microtomography (μCT) and far-field High Energy Diffraction Microscopy (ff-HEDM) were utilized. This allows for the acquisition of a comprehensive 3-D map of the distribution of microstructural defects within a material, determination of the crystallographic orientation of the material surrounding these defects, as well as the lattice strain of the grains before and during fatigue testing.

This study indicated that the superelastic properties and fatigue response of the nitinol wires is strongly influenced by their size and microstructure. Comparing the fatigue data of the wires and analyzing the macroscopic scale results of the 3-D Digital Image Correlation (DIC) technique revealed that the smaller wires exhibited a better functional performance, although they were more vulnerable to surface defects. Conversely, larger wires experienced a more significant microstructural damage during cycling, which was linked to their cooling rate effects. Overall, the results of this research suggest that wire size and microstructure are crucial factors that must be carefully controlled in the design and development of nitinol-based devices.

ACKNOWLEDGMENTS

Parisa Shabani Nezhad

I would like to express my sincere appreciation to my PhD supervisors, Dr. Dinc Erdeniz and Dr. John A. Moore, for their guidance and support throughout my doctoral studies. I am truly grateful for their advice and support through all stages of this research. I also thank Dr. Raymond Fournelle and Dr. Le Zhou for their continuous availability in the lab, as well as their valuable assistance and guidance during the experimental section of my work. I am truly grateful for their contributions and support. I would also like to thank Dr. Andrew Sen for his valuable input and expertise on my committee.

I am grateful to Dr. John Borg, Dr. Allison Murray, Dr. Lobat Tayebi, Dr. David Berzins, Dr. Sergey Lindeman, and Dr. Philip Voglewede for generously allowing me to use their lab facility. Special thanks to the staff of the Advanced Photon Source (APS)-Argonne National Laboratory, specially Jun-Sang Park, Peter Kenesei, and Hemant Sharma for their valuable assistance and expertise during my research.

This research project was supported by the National Science Foundation (NSF) #CMMI-1934753 awarded to Marquette University, and Arthur J. Schmitt Leadership Fellowship, which provided the necessary resources to conduct the experiments.

Finally, I want to thank my husband, Johannes, for his love and support throughout my doctoral journey. His encouragement gave me the strength to overcome the challenges of research and writing. I am deeply grateful to have him by my side.

TABLE OF CONTENTS

LIST OF TABLES

LIST OF FIGURES

1 OVERALL MOTIVATION AND BACKGROUND

1.1 Introduction

This study is focused on the effect of geometry and microstructural features on the fatigue performance of superelastic nitinol wires. This work is presented in five chapters. The first chapter includes an overall background on nitinol and significance of studying the effect of wire size and the fatigue behavior of superelastic nitinol wires. The second chapter is focused on the effect of geometry and compares the structural and functional fatigue of the wires with different wire sizes. In the third chapter, 3-D X-ray diffraction techniques were used to study the phase transformations and functional fatigue behavior of the material, with focus on the microstructural damage accumulation during cycling. In the fourth chapter, a 3-D digital image correlation (DIC) technique was used to study the effect of wire size on the inhomogeneous transformation in macro-scale level. Ultimately, the fifth chapter is dedicated to the overall conclusion of the previous chapters.

1.2 Superelastic Nitinol

Nitinol is a near equiatomic alloy of nickel and titanium that exists within a narrow composition range (49%-51at.%) at low temperatures (1). It is characterized by its high strength at room and elevated temperatures (2), low modulus of elasticity (3), moderate density (2), reasonable impact resistance (2) and ductility (4), good high cycle fatigue properties (5), biocompatibility (5–8) and extraordinary mechanical vibration damping properties (2,6,7,9) that are sensitive to both composition and temperature changes

(2,4,5,7,8). These properties make nitinol an ideal choice for medical, dental, aerospace and automotive industries (10–18).

The importance of nitinol comes from its unusual properties, such as shape memory effect and superelasticity (also known as pseudoelasticity). Both properties arise from the transformation between the two phases (austenite and martensite) that it adopts within a narrow temperature window (4,10–12,19–23) Martensite is the low temperature phase with a lattice structure of B19' that is stable below the transformation temperature window, while austenite is the high temperature phase with a lattice structure of B2, stable above the transformation temperature of the material (4,11,24,25). If the application temperature is below the transformation temperature, the shape memory form of nitinol occurs, in which a previously deformed material recovers its original shape upon heating (Figure 1-1 (a)) (4,11,25). While in its superelastic form, the deformed material returns to its initial shape simply after unloading (Figure 1-1 (b)) (4,11,25). In this research, only the superelastic form of nitinol will be studied.

Superelasticity involves the stress induced transformation of austenite to martensite, followed by strain recovery upon removal of the applied stress (26–28). The superelastic alloys are capable of sustaining and recovering relatively large strains (about 8%) without undergoing plastic deformation (29).

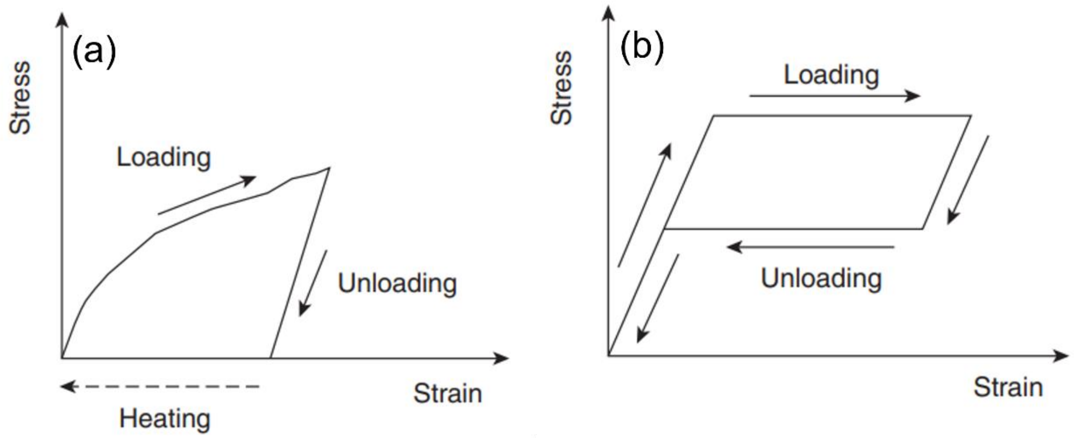

Figure 1-1- the stress-strain behavior of (a) shape memory and (b) superelastic form of nitinol (11).

Figure 1-2 shows a typical stress-strain curve of a superelastic nitinol component. Initially, the material is in the austenitic state and deforms elastically along the straight line OA under load, with the slope of the line corresponding to the Young's modulus of the austenite phase (20,24,29). Once the stress reaches a critical stress level (σ_{Ms}), the upper plateau starts, and the austenite phase isothermally transforms to martensite (29). Point B indicates the completion of the martensitic phase transformation (29). Increasing the applied load will result in elastic deformation of martensite phase. The slope of the line BC indicates the Young’s modulus of the martensite phase (20,29). If the stress exceeds σ_{y}, the martensite phase yields through a conventional dislocation glide mechanism (29–32) Upon unloading, the specimen follows the line CD. Following the reduction in applied stress, the material enters a lower plateau region, and the reverse transformation M→A begins (29). At the point E, the reverse transformation is complete, and the initial austenite phase is recovered (29). The hysteresis loop (difference between the stress-strain curve in the loading and unloading cases) indicates the energy dissipation of the process, or latent heat of the transformation (29,33,34). The ability of the material to undergo internal crystalline transformations is reflected in the hysteresis loop (29).

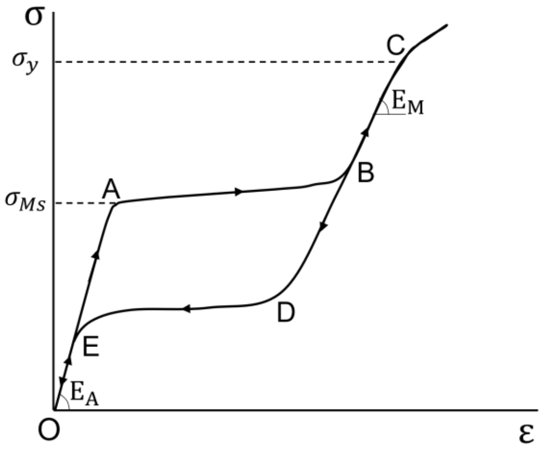

Figure 1-2- A typical stress-strain curve of superelastic nitinol, adapted from M. Schwartz (29).

There are 4 temperatures associated with the phase transformation in nitinol (29–31,35): (i) Martensite start temperature (M_s), the temperature in which martensite starts to form from austenite. (ii) Martensite finish temperature (M_f), the temperature in which the austenite to martensite transformation finishes, and the microstructure is 100% martensite. (iii) Austenite start temperature (A_s), the temperature in which austenite starts to form from martensite. (iv) Austenite finish temperature (A_f), the temperature in which the martensite to austenite transformation finishes, and the microstructure is 100% austenite. The phase transformation occurs over a certain temperature range, where the superelastic hysteresis loop appears in the stress-strain curve of the nitinol. This temperature range is shown in Figure 1-3 (a). Below this range, residual strain is still present after the stress is withdrawn, as illustrated in Figure 1-3 (b). Figure 1-3 (c) displays the superelastic behavior of the material at the temperature of $\mathrm{A_f}$. As the application temperature reaches to $\mathrm{A_f}$, the material exhibits an ideal superelastic behavior with no residual strain upon unloading. Above temperature $\mathrm{M_d}$, the stress-induced martensitic transformation is no longer possible (36,37). Above the superelasticity range ($\mathrm{A_f}$ -$\mathrm{M_d}$), the austenite phase exhibits elastic-plastic behavior as a conventional metal (37–40), shown at Figure 1-3 (d).

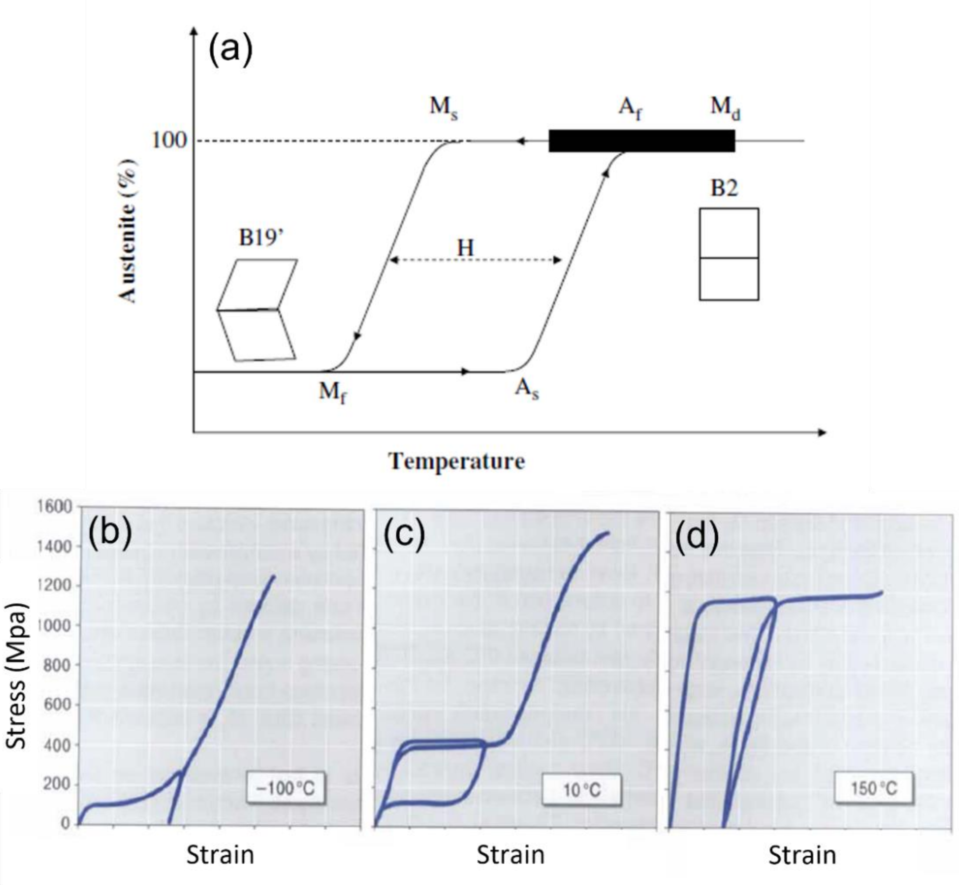

Figure 1-3-(a) Phase transformation temperature range in superelastic nitinol (38), stress-strain curve of a nitinol sample with A_f=10̂C and M_d=150̂C (b) below the superelastic temperature range, (c) around Af, (d) at the temperature of Md (37).

Subsequently, to attain superelastic behavior at the room and body temperature, the austenite finish temperature must be below room temperature (10,37,41,42). Employment of stress at a temperature close to $\mathrm{A_f}$ will result in reorientation of atoms and formation of stress induced martensite (SIM) at elevated temperatures. Since martensite is unstable at the elevated temperatures, the specimen returns to its original shape after removing the external load (38,43,44).

1.3 Problem Description

In the case of the superelastic nitinol, it has been reported that each product form (wires, tubes, sheets, and foil) has a unique characteristic texture (45). In fact, each product, composition and set of process parameters must be individually tested and analyzed to provide accurate fatigue life data (46). Among all the forms, nitinol wires have found developing applications in medical woven or braided textiles. These textiles deliver high drapability and can mimic the structure of the natural arteries and tendons (47–52). According to Norwich et al, the independence of fatigue life from wire diameter may not hold true for nitinol, and the smaller wires demonstrate a higher rate of fatigue survival (46). However, they did not provide specific details on functional or structural fatigue, or the impact of internal defects and damage accumulation on phase transformation in wires of different sizes. Chapter 2 will delve into the effect of wire size on functional and structural fatigue of superelastic nitinol wires, providing more detailed discussions on these topics. Other than that, it has been reported that in the wire specimens, the fatigue properties of the wires are controlled by surface stress concentrations which are mostly introduced by the wire drawing process (53). In general, the small sized wires mostly are subjected to heavy sequential drawing and are more prone to have surface stress concentrations (53). However, it is not clear how the surface defects and wire processing affect the interplay between the functional and structural fatigue of the superelastic materials. More data needs to be collected to determine the significance of the wire diameter on the fatigue performance of nitinol and the failure mechanisms that drive the fatigue failure.

The effect of wire size on fatigue performance of superelastic nitinol is one of the factors that has received less attention and is not clearly understood. In this research, the effect of wire size on fatigue behavior of superelastic nitinol wires will be investigated in detail, to identify the determining factors in the functional and structural fatigue of the material. The proposed work will fill the knowledge gaps and advance the current understanding of fatigue behavior in superelastic nitinol wires with respect to wire size.

1.4 Motivation

In many of its applications, nitinol is subjected to cyclic deformations or stresses. Nitinol-based medical devices may undergo millions of cycles throughout their lifespan due to respiratory or cardiac cycles (54). Fatigue damage caused by cyclic loading reduces the useful life of nitinol, which can have complex adverse outcomes in biomedical devices and aerospace applications (55–57). Fatigue is often the major failure mode for such components (17,18,58).

The Paris-Erdogan law (equation 1-1) has been frequently used to assess the remaining life of the metallic components (59).

$$\frac{\mathrm{da}}{\mathrm{dN}} = \mathrm{A} \cdot (\Delta\mathrm{K})^{\mathrm{m}} \qquad 1\text{-}1$$

This equation describes the crack growth rate by relating the crack length (a) to the change in stress intensity factor ($\Delta\mathrm{K}$) after N cycles, where A and m are constants. It has been shown that austenite and martensite have different stress intensity factors and crack growth rates (10,60,61). Therefore, in a mixed state microstructure, the Paris law does not accurately predict the crack growth rate (60).

The Coffin-Manson law (equation 1-2) is another classical fatigue theory that relates the number of cycles to failure ($\mathrm{N_R}$) to the amplitude of the cyclic plastic deformation ($\Delta\varepsilon_{\mathrm{p}}$), where C and β are the material constants (62,63).

$$N_R . \Delta\varepsilon_p^{\beta} = C \qquad 1\text{-}2$$

The β (fatigue ductility exponent) in this equation is an indicator of the change in the plastic strain (62,63). Although the plasticity and superelasticity are interdependent in superelastic nitinol (64), before the transformation is complete, the plastic strain is insignificant compared to the high strain of the phase transformation (58). Therefore, the Coffin-Manson law does not properly describe the strain associated with the phase transformation in superelastic nitinol.

Basquin equation (equation 1-3) is another power law similar to the Coffin-Manson law that is used to analyze the fatigue data of elastic region of the engineering materials (58,65). Similar to the Coffin-Manson law, $\mathrm{N_R}$ denotes the number of cycles to failure, and C and β are material constants.

$$N_R . \Delta\varepsilon_e^{\beta} = C \qquad 1\text{-}3$$

Basquin equation models classical fatigue for linear elastic metals and corresponds to elastic deformation of a single-phase material (58,65), so it does not predict the fatigue behavior of nitinol in the plateau region.

Bonsignore concluded that the strain limit diagrams are not reliable to predict the fatigue behavior of superelastic nitinol components (66). The fatigue performance of superelastic nitinol depends on the exact composition, heat treatment history, processing history, sample geometry and surface conditions of the component (66). The material composition, loading condition, and process history are unlikely to match the published papers (66).

Therefore, these models are not designed to account for the phase transformation under load and the high strain of the martensitic transformation. The fatigue behavior of superelastic nitinol involves more complexities compared to other traditional metal alloys, which arise from its martensitic transformation (58,67,68). Therefore, these theories may not accurately predict the fatigue behavior of superelastic alloys (58,69–71).

To study the fatigue behavior of polycrystalline nitinol, it is essential to understand the deformation and damage mechanisms at the grain size level, which can vary significantly from grain to grain (72).

Therefore, in this research, far-field high energy diffraction microscopy (ff-HEDM) technique and micro-computed tomography (μ-CT) were utilized to gain a comprehensive understanding of the deformation and damage mechanisms in polycrystalline nitinol under cyclic loading, including the initiation and propagation of cracks, the evolution of microstructure, and the role of crystallographic texture and grain boundaries in fatigue behavior. This information can be used to improve the design and performance of nitinol-based devices and components.

1.5 Contribution to the Field

With respect to standards and material production, the manufacturers of nitinol follow the standards set by ASTM International (ASTM F2063) (66,73), which covers the physical, mechanical, chemical, and metallurgical requirements for wrought nickel-titanium bar, flat rolled products, and tubes that nominally contains 54.5 wt.% to 57.0 wt.% nickel (73). The scope of this standard does not include the required precision to guarantee the shape memory or superelastic features of the product (73). It has been known that the superelastic properties and transformation temperature of nitinol are extremely sensitive to its chemical composition (22,74,75). A 1% change in the chemical composition will result in 10°C change in the transformation temperature (75). The standard does not refer to any material geometry or processing methods such as drawing, rolling, or forming, despite their significance in determining the mechanical properties of the material (73). Concerning the ASTM standards, it is critical that the nitinol specification contain adequate information to tolerably meet the needs of the product.

Studying the effect of wire diameter on the fatigue behavior of superelastic nitinol wire is essential for improving the design and performance of the nitinol-based devices. This research can provide insights into how the size of nitinol wire affects its functional and structural fatigue, enabling researchers to optimize the wire size for specific applications and development of new nitinol-based technologies. By gaining a comprehensive understanding of the effect of wire size on the fatigue behavior of superelastic nitinol wire, researchers can enhance the reliability and durability of devices made of superelastic nitinol wire, particularly those subject to cyclic loading, such as medical implants and aerospace structures.

2 COMPARISON OF FATIGUE PERFORMANCE IN SUPERELASTIC NITINOL WIRES OF DIFFERENT SIZES

2.1 Introduction

The size and location of a flaw can significantly affect the fatigue performance of a material (14,54,82,66,68,76–81). Even small flaws can act as stress concentration points, leading to fatigue crack initiation and propagation (83,84). It has been shown that the processing methods such as wire drawing can introduce microstructural defects to the material (85,86). Due to the impact of flaw size and location on fatigue performance, it is essential to consider the effect of the material processing methods that introduce defects to the material.

This chapter focuses on the functional and structural fatigue of superelastic nitinol wires. Three wires with different diameters were analyzed microstructurally and subjected to low-cycle fatigue tests to determine the effect of internal microstructure on fatigue performance of the wires.

2.1.1 Literature Review

Unfortunately, nitinol devices may suffer from several forms of fatigue damage that range from component shape change to catastrophic fractures (41). One should distinguish between structural fatigue and functional fatigue of nitinol. The structural fatigue concerns local work-hardening and accumulation of microstructural damage, crack initiation and propagation until the failure in a conventional sense (58,83,87–89), while the functional fatigue is related to the changes in the transformation temperatures, transforming volume reduction, and degradation of thermomechanical or superelastic response of the material (58,83,87–89).

Martensitic transformation of nitinol is ideally reversible. However, with increasing cycles, the residual plastic strain in the unloaded state increases (60,68,87,90–92). As shown in Figure 2-1, increasing the number of cycle results in changes in the transformation stress range, the area of the hysteresis loop and the residual strain, which correspond to a degradation of the functionality of superelastic nitinol (68,87,89,93).

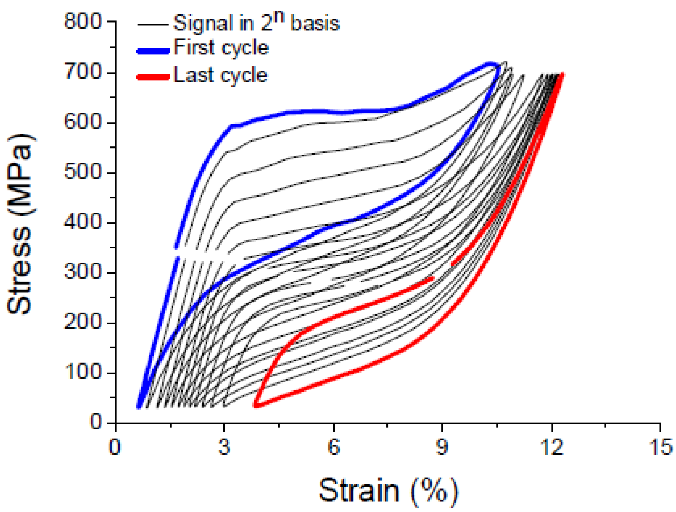

Figure 2-1-Evolution of the fatigue behavior of superelastic nitinol under tension-unloading condition (93).

Microscale material defects, such as inclusions (including both Ti_4Ni_2Ox oxides and TiC carbides) are typically inherent to the material and can be introduced during the manufacturing process (14). During the wire drawing process, longitudinal inclusions may break up into smaller pieces, which can then form stringers along the wire drawing direction (46,94). Defects inherited from production process negatively impact the material's mechanical resistance, particularly regarding fatigue (95). In many cases, the fracture surfaces exhibit non-metallic inclusions at the crack initiation point (15,68,100–102,76,78–80,96–99). The crack nucleation period may be suppressed, depending on the size, location, and morphology of the inclusion (95). Besides, the stress field and local stress concentration around the inclusion assist the martensitic transformation (83,84,103). Thus, the shape, size, distribution, and location of inclusions should be determined to predict the stress distribution around the inclusions and the fatigue failure mode. The microstructural defects may induce multiaxial stress states that result in activation of multiple martensite variants (different crystallographic orientations) in their vicinity (104). Microstructural characterization techniques can identify and analyze microstructural defects, such as cracks, voids, and inclusions, to enhance our understanding of material fatigue failure (81).

Extensive studies have been conducted to investigate the size effect on the fatigue behavior of metallic components. Scheiner et al (105) conducted research on the fatigue behavior of stainless steel and cobalt-nickel alloy wires. They studied wires with diameters ranging from 26 to 46 microns to identify the key factors affecting fatigue life. Their findings suggest that wire strands should be produced with the smallest possible diameter, without introducing structural flaws, to extend their service life (105).

Dai et al (106) conducted a study to examine the impact of thickness on the fatigue properties of polycrystalline Cu foils at micrometer scales. They maintained a consistent grain size across all foils, while the foil thickness was varying from 20 to 420µm. The study found that the surface grains are the dominant factor in controlling fatigue properties of the micrometer-scale Cu foils. When the foil thickness is approaching the grain size, the fatigue life of Cu foils strongly depends on the tensile plasticity of the foils. Overall, the study suggests that the thickness of the foil, in relation to the grain size, plays a significant role in determining fatigue properties (106).

Hofbeck et al investigated the fatigue strength of Cu and Au wires with bamboo type structures. They observed that as the wire diameter decreased, the fatigue strength increased. This increase in fatigue strength was attributed to the small slip distances that are available in thin wires (107).

Merchant et al (108) conducted a study on the fatigue performance of copper foils with thicknesses ranging from 12 to 35 µm at a wide range of strain amplitudes. They monitored the dislocation configurations to understand the mechanism behind fatigue crack propagation. The results of their study showed that the fatigue crack propagation through the foil thickness was related to dislocations and grain structure rather than the foil thickness. However, they observed that strain localization and dislocation configurations were generally observed for the bulk samples (108).

Although the fatigue behavior of wires and foils has been extensively studied in a structural sense, none of these studies have focused on the superelastic functional fatigue of the material.

Ueland et al (109) studied the cycling behavior of the oligocrystalline (polycrystal with small number of grain) in the Cu-Zn-Al shape memory wires with diameters ranging from 100 down to 20 µm. They reported that the energy dissipated per cycle increases with decreasing wire diameter (109).

Soul et al (110) investigated the damping performance of superelastic nitinol wires across a range of frequencies for two different wire diameters, 0.5mm and 2.46mm. The study found that the thinner wire had better damping capacity compared to the larger wire diameter. At low frequencies, the larger wire diameter also exhibited good hysteresis. They explained these findings by considering the balance of heat flow released by latent heat and transmitted to the surroundings (110).

Norwich et al (46) conducted research on the fatigue behavior of superelastic nitinol wires with varying diameters. All wires were drawn from the same starting material and underwent the same heat treatment procedure. The study found that the smaller wire had a better fatigue survival rate, but they did not provide details on the phase transformation and functional fatigue of the material (46).

Despite the widespread use of superelastic nitinol wires in various industries, the effect of wire size on their structural and functional fatigue has not been extensively studied. This is a critical knowledge gap, as wire diameter may significantly impact fatigue behavior. Therefore, further research is needed to fully characterize the fatigue behavior of superelastic nitinol wires with different sizes.

2.1.2 Objective and Goal

Three different sizes of nitinol wire were used to investigate the effect of wire size on the functional and structural fatigue behavior of superelastic nitinol. To manufacture the small-sized wires, the large wires go through multiple hot/cold wire drawing passes that may introduce a large number of defects into the microstructure (111–113). These microstructural imperfections may affect the structural and functional fatigue behavior of the superelastic nitinol (77,99). Besides, the fatigue properties of nitinol are very product specific. Manufacturers follow the same standard for the nitinol superelastic products (ASTM F2063), which covers a wide range of chemical compositions (54.5 wt.% to 57.0wt.% nickel) for wrought nitinol (73). However, it does not include any information about the processing and metallurgical variables of the specimens (73). As small as a 0.1% deviation in chemical composition and slight variations in the production process can result in drastic changes in the physical and mechanical properties of the material (74,75). This gap in the existing standards will adversely affect the accuracy of engineering designs. My hypothesis is that a small change in the geometry, manufacturing and processing variables may significantly affect both functional and structural fatigue of superelastic nitinol. In this work, nitinol wires with three different sizes are subjected to microstructural analysis and low-cycle fatigue tests to provide a better understanding of the effect of wire size on their functional and structural fatigue behavior. The outcome of this objective will fill the manufacturers' information gap around their acceptable tolerance. It will also help to establish a more comprehensive and accurate standard for the consistency of their future products.

2.2 Experimental Procedure

The materials selected for this study were medical grade nitinol wires, purchased from Edgetech Industries[1]. The wires were drawn and annealed based on the material specification sheet provided by the manufacturer. No information was given regarding their processing and heat treatment condition. Table 2-1 presents the information provided by the manufacturer.

Table 2-1-Material specification provided by the manufacturers

Manufacturer	Diameter (mm)	A_f (ºC)	Surface finish	Composition
Edge Tech	0.200	0 to10	oxide	55.92wt% Ni
	0.500	0 to10	oxide	55.74wt% Ni
	1.000	0 to10	oxide	55.74wt% Ni

The critical transformation temperatures of the given nitinol alloy must be determined to ensure that the material is superelastic at the preferred temperatures. As-received wire samples were subjected to thermal analysis using differential scanning calorimetry (DSC) to confirm the transformation temperatures reported by the manufacturer. 40ml aluminum crucibles were used with a Mettler-Toledo DSC (model 822e) equipped with STARe software. To minimize the effect of cutting pressure on the wires, a digital low speed diamond saw with water coolant was used to cut the wires into 4-5mm pieces that fit in the crucibles. An average load weight of 30-40mg was used for each test. The DSC tests were performed using a liquid nitrogen as a coolant and under

---

[1] https://www.edge-techind.com/

nitrogen cover gas. The testing temperatures ranged from -50 to 50°C, and the heating and cooling rate was set to 10°C/min. To measure the transformation enthalpy (latent heat of transformation) and the temperatures, a spline baseline was used to subtract the background. The software calculated the transformation temperatures and the transformation enthalpies. To ensure repeatability of the data for each wire, DSC scans were conducted three times per wire. The reported transformation temperatures and enthalpies are an average of three DSC scans.

Scanning electron microscopy (SEM) images were used to determine the number density and average size of the non-metallic inclusions of the as-received wires. The samples were prepared using standard metallographic techniques (ASTM E3-11). To avoid martensitic phase transformation during the sample preparation, a standard Al_2O_3 abrasive polishing process with minimal surface strain was applied. At least five samples were analyzed to collect statistically relevant data. To determine the number density of inclusions in each wire, a random selection of 5 SEM images with magnification of ×950 was analyzed. The number of inclusions present in each image was manually counted, and then divided by the surface area of the sample captured in the SEM figure.

Load-displacement curves of the samples were collected using a Mark10-ESM750 (displacement resolution 0.001 inch or 0.0254mm) tensile test stand. Each set of data was collected at least 3 times to ensure that it was repeatable. To obtain the best load resolution for each sample, three load cells were used. The MR01-750 (load resolution 0.5 lbf or 2.2241 N), MR01-100 (load resolution 0.1 lbf or 0.4448 N), and MR01-50 (load resolution 0.02 lbf or 0.0889 N) were used for the 1mm, 0.5mm, and 0.2mm wires, respectively. A pair of self-tightening wedge grips (Mark10- G1061-2) were used to measure the pure tensile stress of the wires and avoid the spring back and shear stresses.

The monotonic tensile tests were conducted with a cross head speed of 10mm/min until the wire failed. The upper plateau and failure stress (stress at the breaking point) of the three wires were determined from the tensile tests. Then the wires were cycled under stress-controlled conditions. To assess the upper/lower plateau stresses and shape-recovery behavior of the wires, a cycling frequency of 0.001Hz was used. The frequency was chosen reasonably small to avoid the effect of latent heat of transformation. The upper fatigue limit was set slightly above the upper plateau of the wires, and the lower limit was set at zero. Results of these low strain rate fatigue tests were used to determine the lower plateau stress of the wire. The Mark10 instrument delivered the force-displacement curves of each sample. The “engineering stress” was calculated by dividing the force (obtained from the Mark-10 device) by the initial cross-sectional area of the wires ($\sigma = \frac{F}{A}$). The “engineering strain” was calculated by dividing the displacement (obtained from the Mark-10 device) by the initial length of the wire ($\varepsilon = \frac{\Delta l}{l_0}$). The initial length of the wire (l_0) was measured as the distance between the upper and lower grips. After determining the upper/lower plateau stresses of the wires, the rest of the tests were performed with frequency of 0.1Hz.

The Mark-10 device reports the distance traveled by the upper grip during the test. However, the displacement obtained from the Mark-10 may not be accurate. Therefore, a digital image correlation (DIC) technique was used to measure the precise deformations. The DIC data was collected using a Leica M-125C microscope, mounted on a horizontal adapter. It was equipped with two high-speed Dantec cameras with a resolution of 1µm. The experimental setup can be seen in Figure 2-2.

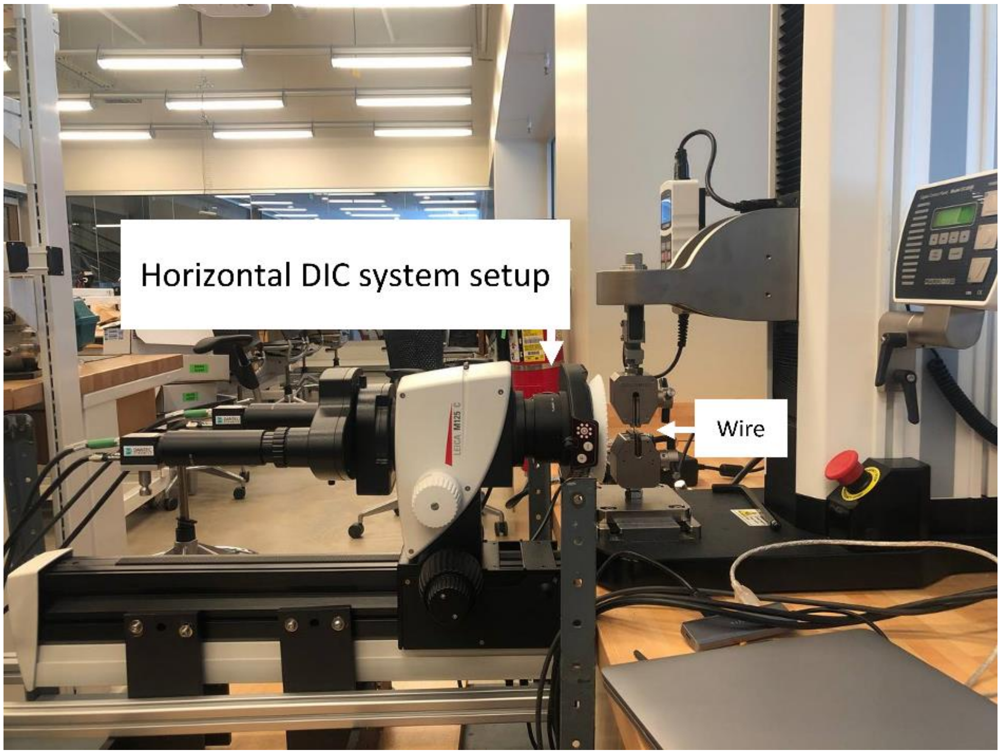

Figure 2-2- DIC system setup.

The DIC technique tracks and correlates a random pattern on the surface of an object to measure its displacement (114–116). The random pattern can either be naturally inherent surface features or an artificially added pattern (114,117). The quality of the patterns is a critical factor in determining the accuracy and reliability of the DIC measurements (118). The stability, randomness, density, and high contrast (ideally black and white) of the speckle pattern are important factors for ensuring the accuracy of displacement and strain measurements (118,119). The pattern elements should be small enough to provide high spatial resolution, but large enough to be visible under the magnification used for imaging (119).

To prepare the nitinol wires for DIC measurement, they were painted with a white Angelus acrylic leather paint. This paint provided enough flexibility and did not flake off or shed with strain changes on the surface of the wire. Then an airbrush was used to add black speckle patterns on the white background. Figure 2-3 shows the speckle pattern created on the 1mm wire before the DIC measurement.

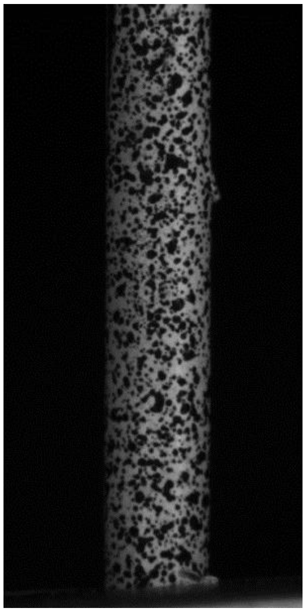

Figure 2-3- speckle pattern created on the wire surface.

Global strain is defined as the total strain experienced by the entire length of the specimen. To measure the precise global strain, the initial length of the wire was selected small enough, so the total length of the wire was within the “field of view” of the DIC cameras. For the 0.2mm and 0.5mm wires, the magnification of ×12.5 was used and the sample size (the distance between the upper and lower grips) was approximately 5mm. for the 1mm wire, the magnification of ×8 was used, with a sample size of 8mm. The fatigue testing frequency and image acquisition speed were both set at 0.1Hz. So, a total of 100 images were collected for each cycle. A displacement-controlled fatigue test was carried out on all three wires. The upper and lower fatigue limits were set slightly above the upper plateau and slightly below the lower plateau of the wire, respectively. The Istra4D V4.7 software was used for image acquisition, evaluation, visualization. Prior to the test, a calibration target was used as a reference object to define the intrinsic and extrinsic parameters of the cameras, including each camera's perspective of the object, camera‘s perspective to each other, and the global coordination system. A calibration target of 3mm was used for the 1mm wire and a 2mm target was used for the 0.5 and 0.2mm wires. Any change in image acquisition or camera settings (including magnification, focus or aperture) may change the calibration parameters and requires another calibration.

To develop the stress-strain curves with precise strain, the results of fatigue instrument (Mark-10) was matched with the DIC data. The fatigue and DIC tests were run at the same time, so their results were matched based on time compatibility. The DIC images were collected without interruption until the end of the 10th cycle. At the 20th and 50th cycles, the DIC image acquisition was started over again. After each image acquisition start up, the first image is counted as the reference point with zero strain. Therefore, strain maps of the 20th and 50th cycles do not include any residual strain of the previous cycles. Since the cycling was performed under a displacement-controlled condition, it is assumed that the upper strain remains the same. Thus, the obtained upper strains for the 20th and 50th cycles were shifted to the upper strain of the first 10 cycles for comparison.

The accuracy of the elastic modulus calculated directly from the fatigue or tensile test stand results is compromised by the inaccurate measurement of strain. Therefore, after developing the stress-strain curves with the precise DIC strain measurements, the elastic modulus of both austenite and martensite for the three different wire sizes were calculated. This was done by determining the slope of the linear section of the curves, using the SLOPE function in Microsoft Excel. To ensure repeatability, each test was repeated 3 times. The stress-strain curves were further evaluated to determine the gradual loss of functional properties of the superelastic nitinol wires. Evolution of the hysteresis shape and residual martensite were examined to distinguish the functional and structural fatigue. The area of the hysteresis loop was measured using the ImageJ image analysis software [2].

The main purpose of this study is to determine the role of the microstructural and geometrical features on the fatigue life of the superelastic nitinol wires. Many researchers have shown that the most common observed fatigue crack initiation site is a surface defect (95,120–122). To quantify the surface roughness of each sample, a confocal laser microscope was used. Each test was repeated 3-5 times to make sure that it was repeatable. To improve the surface quality, and subsequently prevent the surface crack nucleation and premature failure, the wires were electropolished prior to the fatigue

---

[2] https://imagej.nih.gov/ij/download.html

testing. The electropolishing of the nitinol wires was conducted in an electrolyte solution of 80 vol.% acetic acid (99.5-100%- Mallinckrodt Baker, Inc.) + 20 vol.% perchloric acid (60-70% solution- Mallinckrodt Baker, Inc.) (123) at room temperature. The two-electrode setup consists of Ni as counter electrode (cathode) and nitinol as working electrode (anode) (123). A current was applied to remove the initial oxide surface of the wires. It was followed by a surface treatment procedure to achieve a smooth finish surface. The experiments revealed that the electropolishing current and time vary for each wire. The parameters depend on the initial surface finish of the as-received wire and the wire size. The electropolishing current and time were determined for each wire through trial and error. Table 2-2 shows electropolishing process of each wire.

Table 2-2- surface treatment electropolishing parameters of each wire.

Diameter (mm)	Remove oxide
0.200	Current 0.4A and 15 seconds
0.500	Current 1A and 15 seconds
1.000	Current 3A and 45 seconds

Postmortem SEM analysis was conducted to identify the source of failure and characterize the failure mode for each sample. The crack propagation and rupture zone of the wires were measured using ImageJ.

The DSC tests were conducted after 500, 1000, 1500 cycles to evaluate the evolution of the transformation temperatures and functional degradation during cycling.

2.3 Results

Figure 2-4 illustrates the DSC results of the as-received wires. The transformation enthalpies (areas under the DSC peaks) of the three wires were assessed to compare their superelasticity and evaluate their functional fatigue.

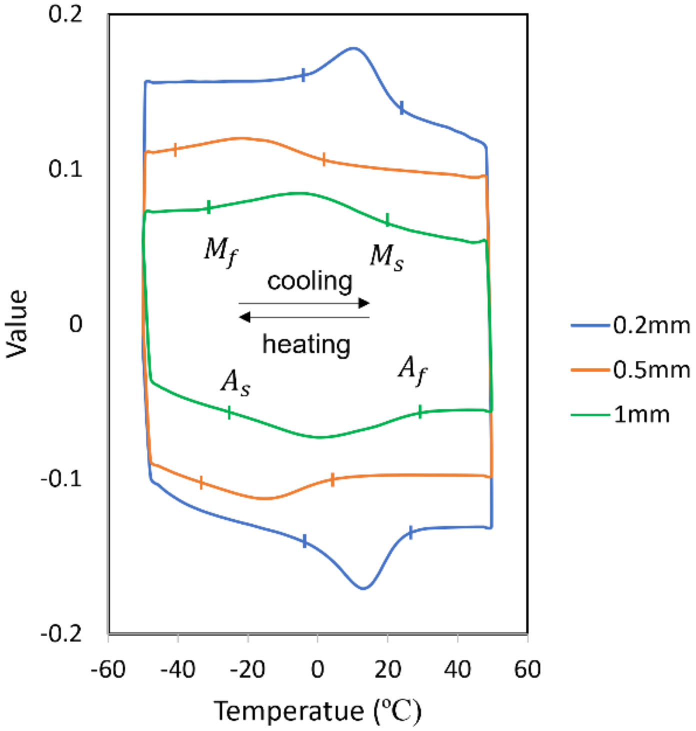

Figure 2-4-DSC of the as-received wires.

Table 2-3 shows the critical transformation temperatures and enthalpy of transformation, taken from the DSC data. The 0.2mm wire had the highest transformation enthalpy and the closest $\mathrm{A_f}$ temperature to the room temperature, while the 0.5mm wire had the lowest transformation enthalpy and the farthest $\mathrm{A_f}$ temperature from the room temperature.

Table 2-3-critical transformation temperature and enthalpy of the as-received wires.

Wire size (mm)	A_s (ºC)	A_f (ºC)	M_s (ºC)	M_f (ºC)	$E_{M\rightarrow A}$ (j/g)	$E_{A\rightarrow M}$ (j/g)
0.200	-0.63±0.36	24.05±0.18	21.26±0.0	-2.24±0.36	-2.71±0.18	2.0±0.09
0.500	-34.42±0.58	1.98±0.56	-0.79±0.94	-39.22±0.06	-0.84±0.07	0.97±0.01
1.000	-25.66±1.55	29.30±0.52	19.91±0.90	-29.48±3.22	-1.92±0.05	1.89±0.43

Figure 2-5 shows the SEM images of the three different wire sizes. The arrows denote the inclusions and microcracks that formed in the front and rear of the inclusions during the wire drawing process. The figures show that the microstructure of the 0.2mm wires contained sharp voids and cracks at the front and back of the inclusions. Some micro-voids can also be seen around the inclusions of the 0.5mm and 1mm wires. However, this microstructural feature is more prominent in the 0.2mm and 0.5mm wires.

Table 2-4 presents information on the size and density of the inclusions (the void lengths are not included in the inclusion size measurements). According to this result, the 0.2mm wire has the highest density of the microstructural defects compared to the other wires.

Figure 2-6 (a) shows the result of tensile test of the wires with three different sizes. This figure shows that the 0.2mm wire had a lower plateau stress compared to the 0.5mm and 1mm wires. Figure 2-6 (b) exhibits the first cycle of the three wires, cycled under stress-controlled condition with frequency of 0.001Hz. Based on measurements taken through crosshead motion, it can be observed in this figure that the 0.5mm and 1mm wires exhibited some residual strain at the end of the first cycle. Figure 2-6 (c) and (d) show the change in upper plateaus and the difference between the upper and lower plateaus of wires during the first 30 cycles, respectively.

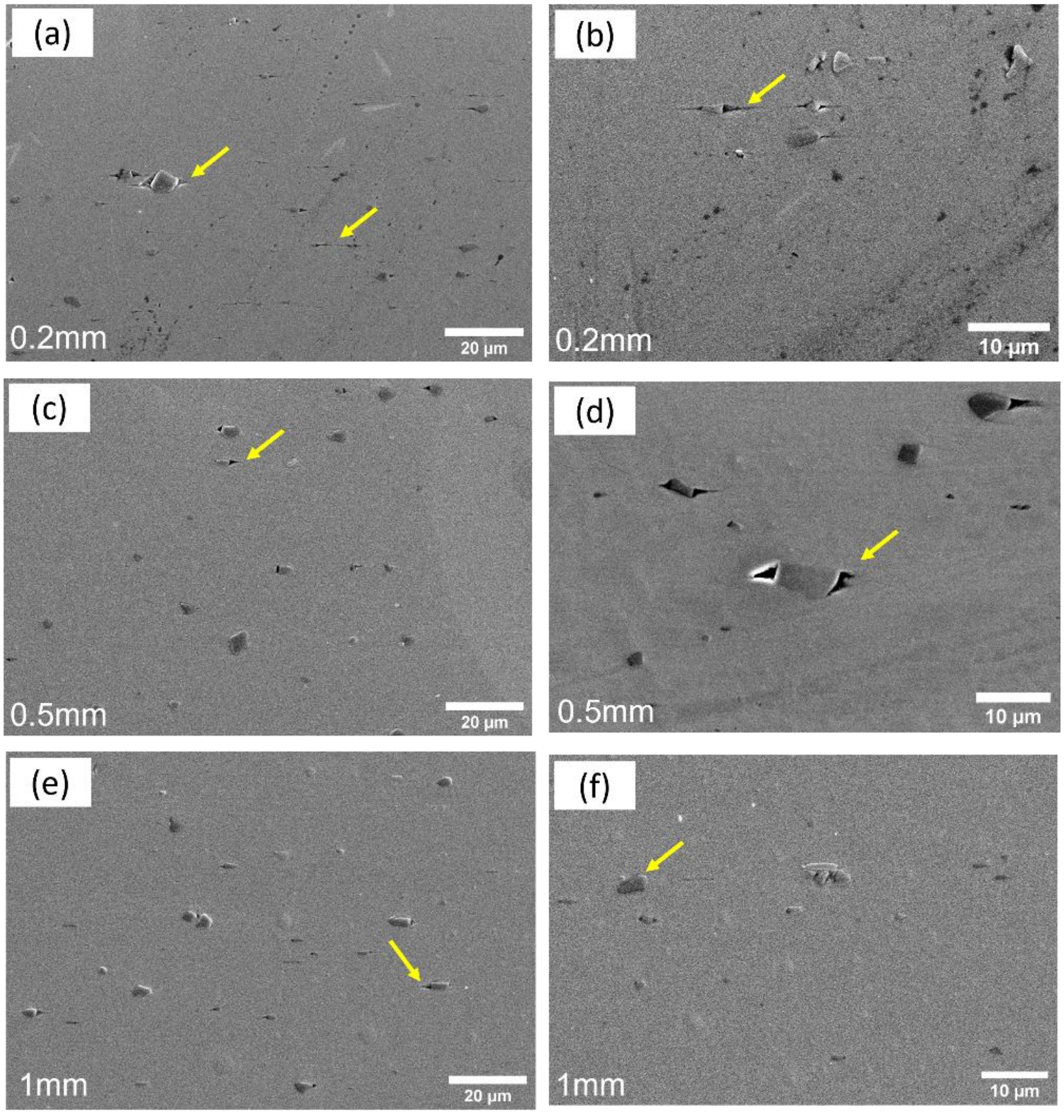

Figure 2-5-SEM images of the inclusions observed in the wires (a) and (b) 0.2mm, (c) and (d) 0.5mm, (e) and (f) 1mm, note that the drawing direction is left-right.

Table 2-4-the maximum size, average length, and density of the inclusions

wire size (mm)	Max Inclusion Length (µm)	Average Inclusion Length (µm)	Inclusion Density $([\#/m^2]\times 10^9)$
0.200	4.94	2.90 ± 0.93	5.65
0.500	7.52	3.84 ±1.80	2.52
1.000	4.62	2.58 ± 1.03	3.17

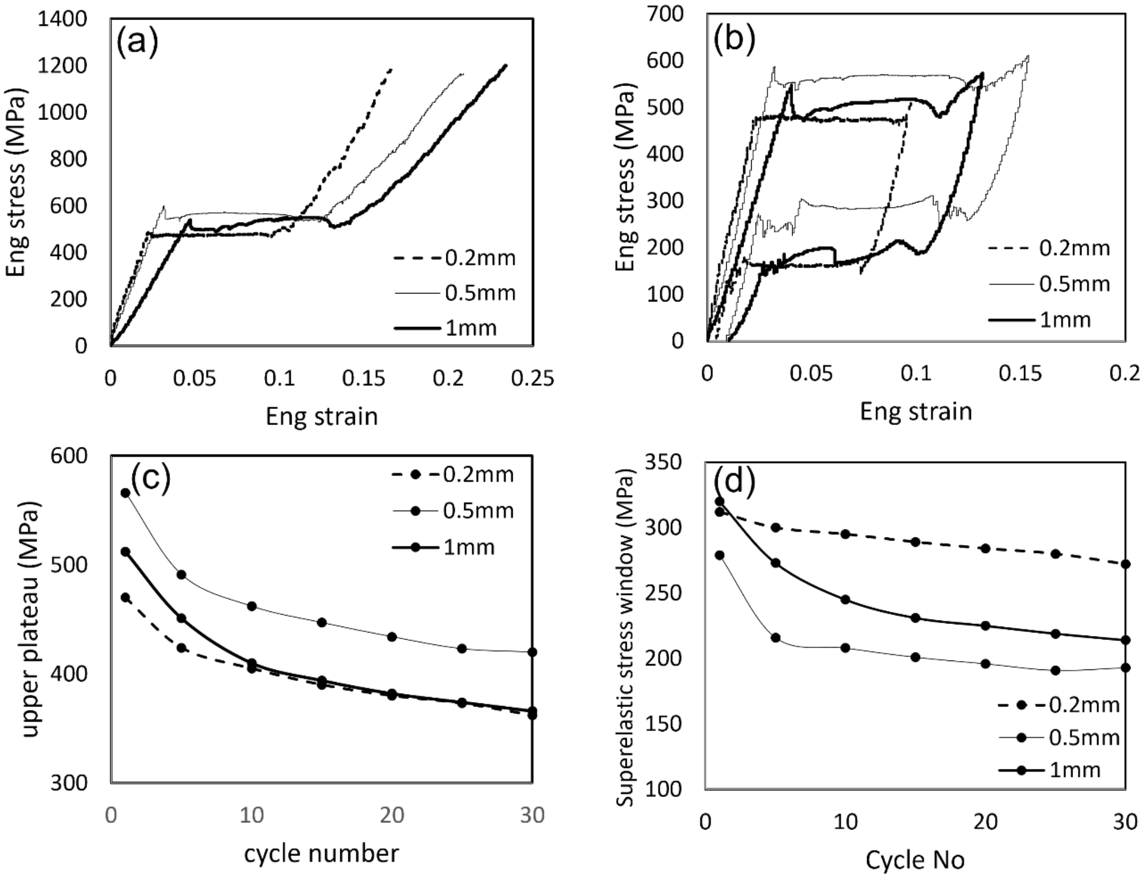

Figure 2-6- (a) tensile test until failure (b) first cycle of the wires, (c) the upper plateau of the wires for the first 30 cycles, (d) the difference between the upper and lower plateaus for the first 30 cycles.

Table 2-5 shows the failure stress of the tensile tests, along with average upper and lower plateau stresses of the first cycles. The results indicate that the upper and lower plateaus, as well as the difference between them, rapidly declined in the first 10 cycles and then stabilized. The 0.2mm wire exhibited the most stable superelastic stress window (the difference between the upper and lower plateaus).

Table 2-5- the average of failure stress, upper and lower plateau of the wires

wire size (mm)	failure stress (MPa)	upper plateau stress (Mpa)	lower plateau stress (MPa)
0.2	1416.50 ± 11.50	471.67 ± 3.40	127.38 ± 0.91
0.5	1233.33 ± 24.73	569.33 ± 2.49	263.95 ± 5.42
1	1396.00 ± 66.87	523.67 ± 0.47	175.89 ± 3.35

The data of Figure 2-6 and Table 2-5 were collected under a cycling frequency of 0.001Hz. After these data were collected, the rest of the tests were carried out with a cycling frequency of 0.1Hz. Figure 2-7 shows the first cycle of the three wires with the frequency of 0.1Hz. After increasing the strain rate, the required stress to initiate the phase transformation slightly increased in all wires. Also note that an upward trend was found in the 1st cycle plateaus of all three wires.

The DIC tests were performed to determine the accurate strain field of the wires. Figure 2-8 shows the load-displacement curve and DIC pattern of the first cycle, for the three wires. The wires were initially in an austenitic state with zero strain, indicated by the blue color on the DIC scale axis. Point 1 in Figure 2-8 (a), (c) and (e) marks the onset of plateau stress in all wires, but no macroscopic martensite band formed at this point. The DIC system detects the austenite or martensite bands based on their measured strain. At point 2, a high strain region formed near the grips in all the wires and grew throughout the wires. The high strain region was represented in red by the DIC software and represented the martensite band. The highest achieved local strain in all wires were between 8-9%. In 0.5mm and 1mm wires, another band forms at the lower grip and the two bands coalesced.

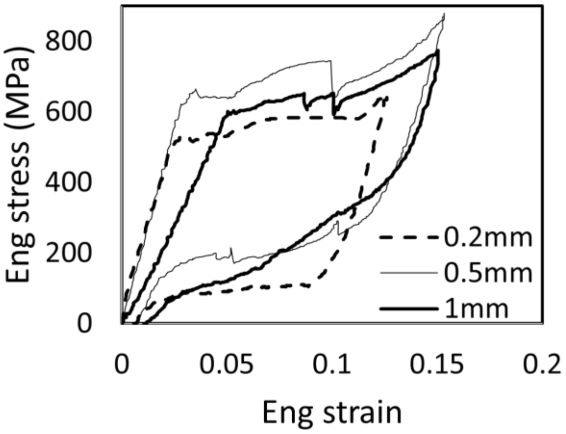

Figure 2-7- first cycles of the wires with frequency of 0.1Hz.

The stress-strain curves shown in Figure 2-9 (a), (b) and (c) have been created from time compliance of the Mark-10 fatigue test and DIC data. Figures (a), (b) and (c) are associated with the 0.2, 0.5 and 1mm wires, respectively. Figure 2-9 (d), (e), (f) and (g) compare the 1st, 10th, 20th and 50th cycles of the wires, respectively. Assessment of the Figure 2-9 (d)-(g) confirms that the 0.2mm wire exhibits a more ideal flat plateau, compared to the 0.5 and 1mm wires. Figure 2-9 (h) shows the change in hysteresis loop area of the wires in 50 cycles. As illustrated in Figure 2-9 (h), the hysteresis area of the 0.2mm wire dropped by 15% during the first 10 cycles, compared to the 50% and 54% drop in the 0.5mm and 1mm wires, respectively. The change in residual strain of the wires is exhibited in Figure 2-9 (i). At the end of the 10th cycle, the accumulated residual strain of the 0.2mm wire was about 0.56%, compared to 1.34% of the 0.5mm wire and 1.19% of the 1mm wire. Since the initial image acquisition stopped at the end of the 10th cycle, only the residual strain of the first 10 cycles were used in this figure.

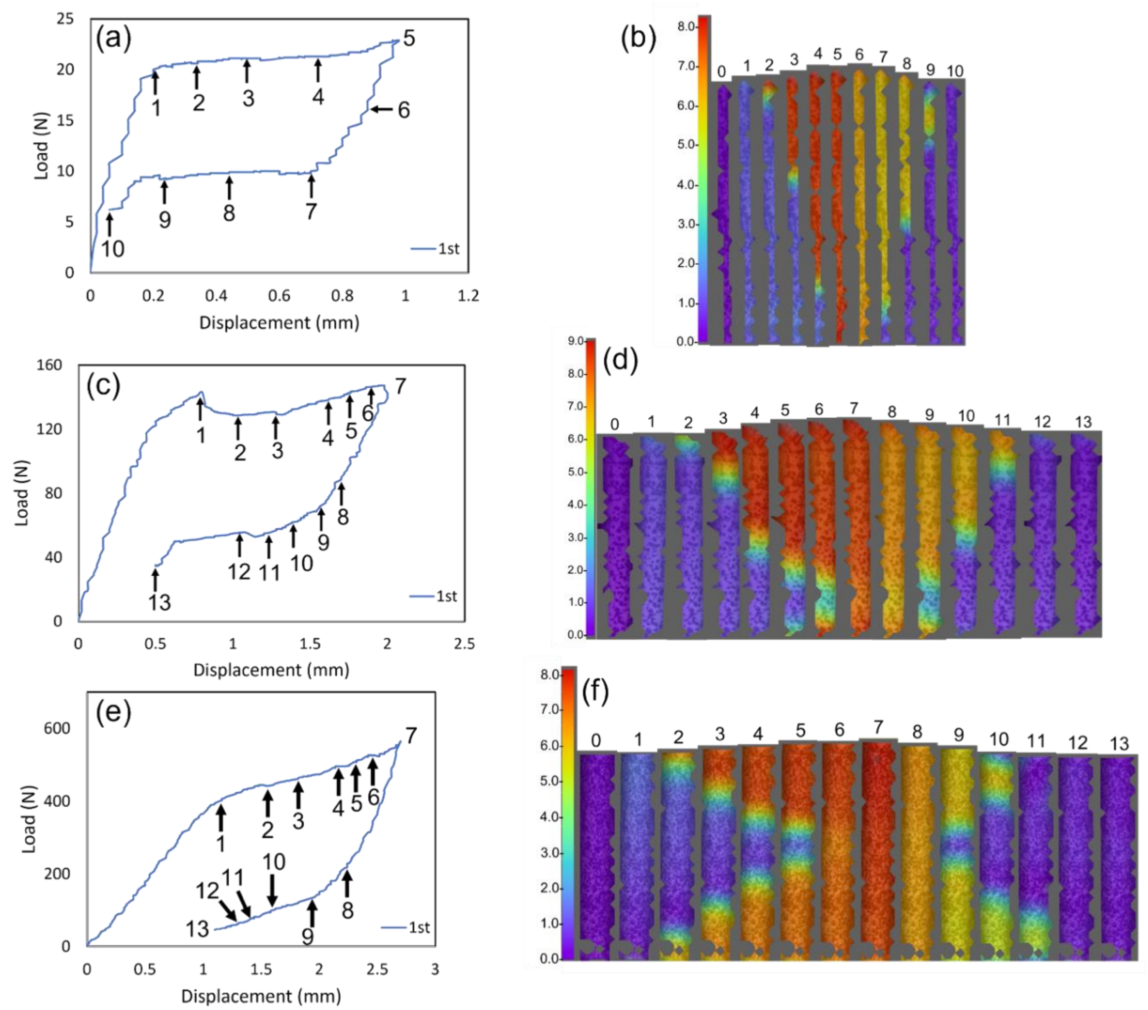

Figure 2-8- (a) the load-displacement curve of the first cycle of 0.2mm wire (b) 0.2mm wire DIC pattern, (c) the load-displacement curve of the first cycle of 0.5mm wire (d) 0.5mm wire DIC pattern, (e) the load-displacement curve of the first cycle of 1mm wire (f) 1mm wire DIC pattern.

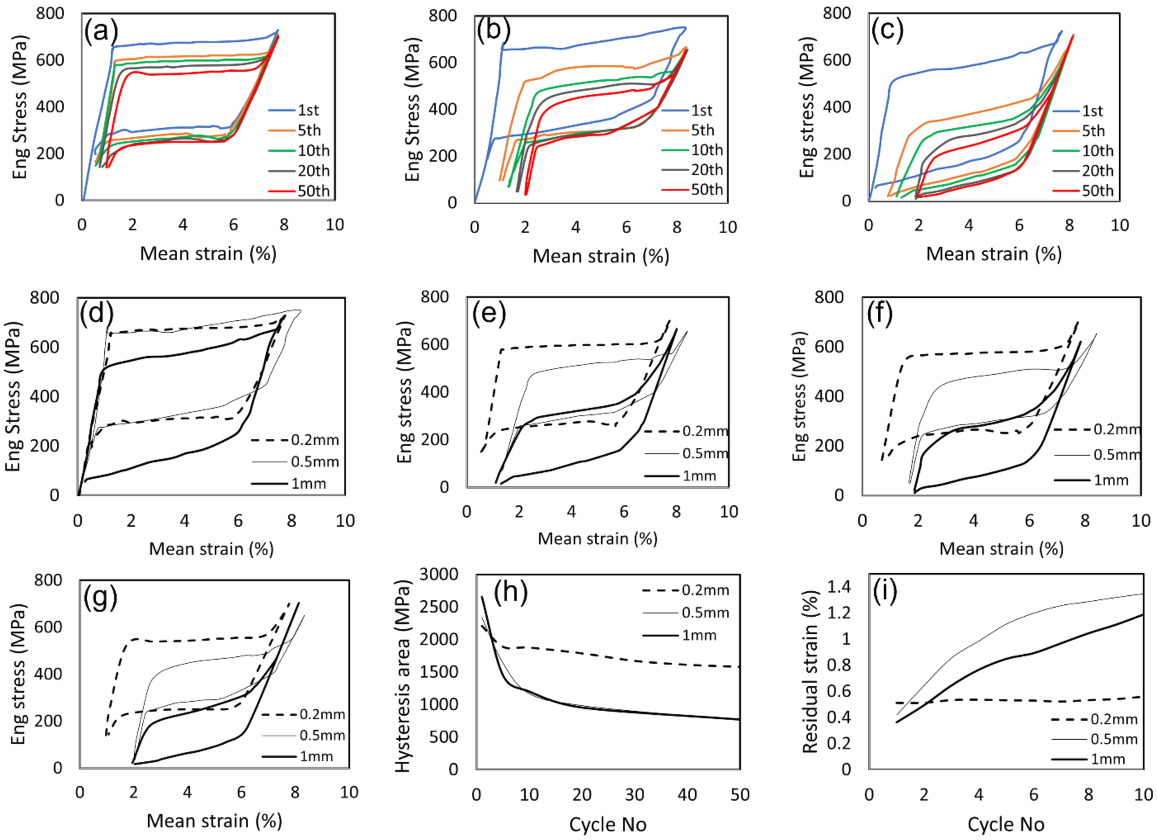

Figure 2-9- (a) engineering stress-mean strain of (a) 0.2mm, (b) 0.5mm, (c) 1mm, comparison of the (d) first cycles, (e) 10th cycles, (f) 20th cycles, (g) 50th cycle, (h) hysteresis areas, (i) residual strains.

The stress-strain curves of Figure 2-9 (a), (b) and (c) were used to determine the Young's modulus of the austenite and martensite phases of the three wires, shown in Table 2-6. As indicated in the table, the martensite phase had a lower elastic modulus compared to the austenite phase.

Figure 2-10 (a), (b) and (c) show surface of the as-received 0.2, 0.5 and 1mm wires, respectively; and Figure 2-10 (d), (e) and (f) display the electropolished surface of each wire. It can be seen from the figures that the surface quality of the wires significantly improved after the surface treatment.

Table 2-6- austenite and martensite elastic modulus of the wires

Wire size (mm)	Austenite elastic modulus (Gpa)	Martensite elastic modulus (Gpa)
0.200	54.60±1.18	25.95±1.49
0.500	66.42±7.26	26.40±0.55
1.000	56.33±3.57	26.69±1.04

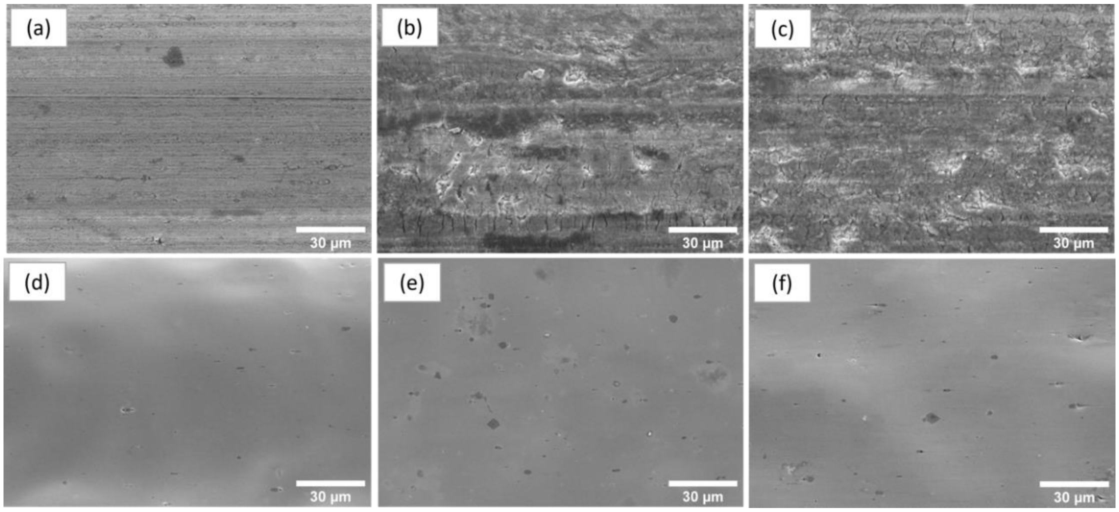

Figure 2-10- SEM images showing the surface of the wires, as-received (a) 0.2mm, (b) 0.5mm, (c) 1mm, after surface treatment (d) 0.2mm, (e) 0.5mm and (f) 1mm.

Figure 2-11 (a) shows the surface of a 1-mm wire acquired by confocal laser microscopy. Figure 2-11 (b) displays the cross-sectional profile of the wire and Figure 2-11 (c) exhibits the same profile after flattening. The average of profile absolute values ($\mathrm{R_a}$) were used to quantify and compare the surface roughness of the wires. Table 2-7 shows the surface roughness of the as-received and electropolished wires. The results of confocal laser microscopy also confirmed the surface quality improvement after the surface treatment process.

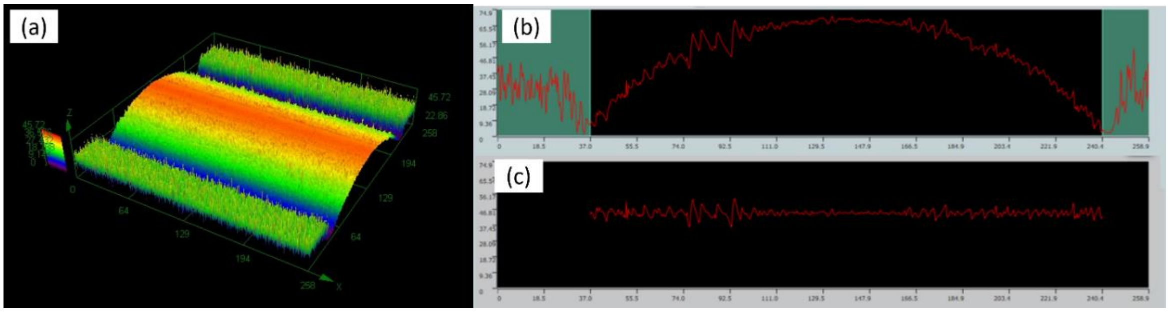

Figure 2-11- confocal laser microscopy result (a) surface of a 1mm wire, (b) a random profile, (c) the same profile after flattening filter.

Table 2-7-average surface roughness

Wire size (mm)	0.200	0.500	1.000
Ra (µm), as-received	0.644	0.817	0.794
Ra (µm), electropolished	0.414	0.540	0.353

Figure 2-12 compares the effect of surface treatment procedure on the fatigue mechanism of the 0.2mm wire. Figure 2-12 (a) shows the fracture surface of a non-electropolished 0.2mm wire. Figure 2-12 (b) and (c) display enlargement of some regions of the fracture surface, presenting the beach marks and river marks at the surface. As illustrated in Figure 2-12 (f), the crack initiated at the surface of the wire for this sample. Figure 2-12 (d) displays the fracture surface of an electropolished 0.2mm wire. Figure 2-12 (e), (f) and (g) emphasize more detail of the fractured surface. Similar to the non-electropolished sample, this sample also exhibited two regions, one fatigue with beach marks and one of the final fracture. A non-metallic inclusion was found at the crack initiation site of the electropolished wire (Figure 2-12 (e)). The arrows show the crack growth direction.

Figure 2-13 exhibits the longitudinal surface of the 0.2mm wire, perpendicular to the fracture surface seen in Figure 2-12 (d). The surface “A” at Figure 2-13 (a) represents the fracture surface after fatigue failure. The arrows in Figure 2-13 (a) indicate the damage caused by the grip. Figure 2-13 (b) shows a surface crack that formed at a corner of an inclusion.

The evolution of transformation temperatures and enthalpies after fatigue is displayed in Figure 2-14 (a), (b) and (c), for the 0.2, 0.5 and 1mm wires, respectively. The DSC peaks of the fatigued wires, as shown in Figure 2-14, initially shifted to the right. However, in the 0.5 and 1mm wires (Figures (b) and (c)), the peaks gradually split up as the cycle number increases, and the two peaks gradually moved away from each other.

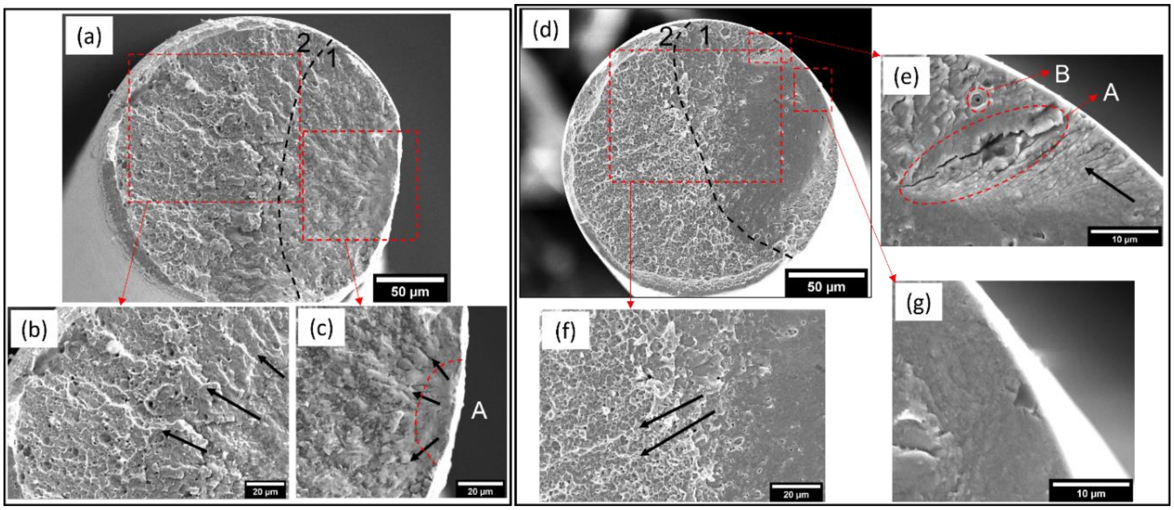

Figure 2-12- (a) the fracture surface of 0.2mm wire, not electropolished, (b) crack growth direction (c) crack initiation site (d) fracture surface of 0.2mm wire, electropolished, (e) secondary crack, (f) direction of crack growth, (g) crack initiation site.

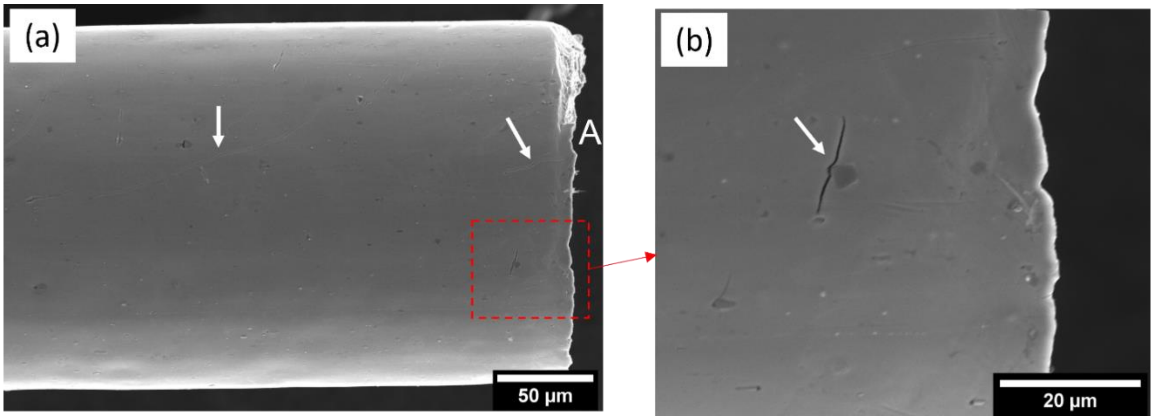

Figure 2-13- (a) longitudinal fracture surface of the electropolished 0.2mm wire (b) a crack that initiated at the corner of a surface inclusion.

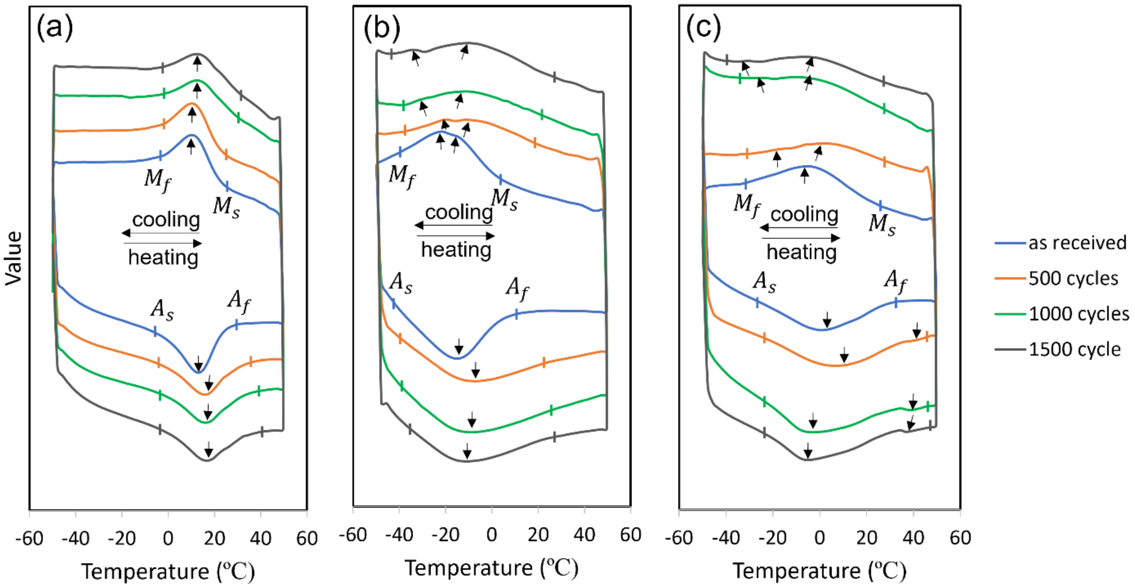

Figure 2-14- evolution of critical transformation temperatures after fatigue (a) 0.2mm, (b) 0.5mm, (c) 1mm.

2.4 Discussion

2.4.1 Functional Fatigue

To exhibit the maximum superelasticity effect at room temperature, superelastic nitinol should have an $\mathrm{A_f}$ temperature that is slightly below room temperature (124). The DSC results of the as-received wires (Figure 2-4) and their tensile behavior (Figure 2-6 (a)) showed that all three wires were superelastic at room temperature. Although the wires were intended to be the same based on their material specification provided by the manufacturer, we found variations in their material properties. The DSC result (Figure 2-4) showed that the 0.2mm wire presented an $\mathrm{A_f}$ temperature closer to the room temperature, with a relatively higher transformation enthalpy. The transformation temperature of nitinol can be influenced by various factors. Kokkinos et al. demonstrated that subjecting Ni-rich nitinol alloys to thermal aging treatment leads to the creation of

$\mathrm{Ni_4Ti_3}$ precipitates and intermediate R-phase, which causes a change in the composition and results in a change in the transformation temperatures (125,126). A more detailed discussion of the effect of the intermediate R-phase can be found in Appendix 2-B. Depending on annealing temperature, time and cooling rate, the transformation temperatures may dramatically change (126–130). Jahanbazi et al showed that both cold work and heat treatment have an impact on transformation temperatures (127). They found that a higher cooling rate results in a lower $\mathrm{A_f}$ temperature, while a greater extent of cold work leads to an increase in the $\mathrm{A_f}$ temperature (127). Carl et al reported that even small changes in the composition can have a significant impact on transformation temperatures (128). The manufacturer did not provide information regarding the wire processing, but according to the material specifications, all wires were in an annealed condition. There was no noticeable sign of the intermediate R-phase in the stress-strain curve of any of the wires. However, the slight presence of R-phase in the 0.5mm wire will be discussed in Chapter 4.

Many researchers have shown that as the application temperature reaches $\mathrm{A_f}$, the material exhibits an ideal superelastic behavior with no residual strain upon unloading (37–40). Therefore, it is expected that the 0.2mm and 0.5mm wires exhibit the most and the least stable superelastic response, respectively, which is in agreement with Figure 2-9. As shown in Table 2-3, the 0.5mm wire showed a significantly lower transformation enthalpy. The strong decrease in the enthalpy of the transformation in the 0.5mm wire is caused by stabilization of the austenite phase (131,132). The enthalpy of transformation in nitinol is closely related to its transformation temperature (132). As mentioned earlier, the 0.5mm wire has the highest difference between its $\mathrm{A_f}$ temperature and the application temperature (room temperature). Stabilization of the austenite at the elevated temperatures (above its $\mathrm{A_f}$ temperature) makes it harder for the martensite phase to be stress-induced (131,132).

The area of the hysteresis loop represents the capability of the material to dissipate energy and recover the applied deformation (89). Increasing the number of cycles and consequential accumulation of defects results in gradual reduction of energy dissipation per cycle (area of the hysteresis loop) and an increase in the residual strain. It also can be seen in Figure 2-9 (i) that the residual strain growth rate in 0.2mm wire is significantly lower than the other two wires. The functional fatigue could be described in terms of the ability of the material to absorb energy (i.e., the area of the hysteresis loop) or the evolution of residual strain (68,87). From these observations, it can be concluded that the 0.2mm wire shows a better functional behavior than the 0.5 and 1mm wire.

Since the $\mathrm{A_f}$ temperature of the 0.5mm wire was relatively far from the application temperature, it does not exhibit an ideal superelastic behavior. So, the measured strain of the 0.5mm wire contains some plasticity as well. The $\mathrm{A_f}$ temperature of the 1mm wire is close to the application temperature. So, it can be expected that the contribution of plasticity in the residual strain of the 1mm wire is insignificant compared to the 0.5mm wire.

To avoid the effect of the transformation latent heat, the data of Figure 2-6 was collected under the frequency of 0.001Hz. When the test is performed in very low frequency conditions, it is expected that the wires recover the deformation at the end of the first cycle, with the least amount of residual strain. Figure 2-6 (b) showed that the 0.5mm and 1mm wires had some residual strain. However, after holding the sample at room temperature, a 100% strain recovery was detected after one cycle. This observation can be justified by the shape memory effect and high sensitivity of the superelastic nitinol to the temperature change. Due to the latent heat of transformation, the specimen experiences a non-isothermal condition. Therefore, the residual strain is governed by two main sources: (i) the isothermal superelastic strain, which recovers upon unloading, and (ii) the strain which is caused by the accumulated heat and recovers as the wire cools down (133). While the internal heat production from the transformation latent heat is proportional to the specimen volume, the heat exchange with the surroundings is proportional to its surface area. The competition between these two factors defines the evolution of strain (134). It also has been known that the larger surface area to volume ratio ($\frac{A}{V} = \frac{2\pi rh}{\pi r^2 h} = \frac{2}{r}$) causes the object to cool down faster (135). Therefore, the 1mm wire has a lower cooling rate and holds more heat than the smaller wires. This factor contributes to the higher residual strain of the 1mm wire, as well.

As shown in Figure 2-14, the DSC peaks of fatigued wires, initially shifted to the right. However, as the cycle number increased, the peaks of 0.5mm and 1mm wires gradually split and moved further apart. This phenomenon indicates the development of an intermediate R-phase. Santos et al (136) reported that R-phase transforms to martensite under applied load. However, it does not recover its deformation upon unloading. R-phase tends to show more shape memory effect, that the deformation recovery occurs after heating the sample above its A_f temperature (136). Formation of the intermediate phase may also contribute to the higher residual strain of the 0.5 and 1mm wires. However, as illustrated in Figure 2-14, the intermediate R-phase appears as the cycle number increases and it may not have a large contribution during the first 10 cycles. Appendix 2-B includes more information about the effect of R-phase on the mechanical behavior of the superelastic nitinol wires.

Table 2-6 shows the elastic modulus of the wires, where the strain measurements were taken from DIC results, which indicated that the 0.2mm wire had a lower elastic modulus compared to the other wires. Lach et al (137) found that there are two main factors that affect the stress-strain behavior (i.e. the transformation stress plateau and elastic modulus) of the nitinol: (i) the presence of microstructural phases such as martensite and R-phase in the initial microstructure; (ii) their stress state (either twinned with low residual stresses, or detwinned with high residual stresses). So, the stress-strain behavior strongly vary with the heat treatment history, micromechanical state of the material and its initial microstructure (137). While the thermo-mechanical history of the wires was not provided by the manufacturer, a microstructural analysis may explain the difference between the stress-strain behavior of the wires. As presented in Table 2-4, the 0.2mm wire had the highest defect density, introduced through the production process. Therefore, it may experience a higher micro-stress fluctuation within the initial austenite matrix. As displayed in Figure 2-5 (a) and (b), the 0.2mm wire contained a series of micro-flaws elongated in the longitudinal direction of the wire. These microstructural flaws around the non-metallic inclusions were likely introduced through the wire drawing process (113). These micro-flaws are also seen around some of the larger inclusions of 0.5mm wire as well. The larger density of inclusions and microstructural flaws in the 0.2mm affects the micro-stress state of the matrix surrounding them and leads to partial transformation of the nearby grains. With the same explanation, the 0.5mm wire had the lowest density of microstructural defects and the highest upper plateau stress.

As exhibited in Figure 2-7, the strain rate affected the shape of the hysteresis area and the plateau stresses. Many studies have shown that an increase in the strain rate results in transformation hardening, which is also a direct outcome of accumulation of the transformation latent heat (38,132–134,138). As a result of transformation hardening, the phase transformation becomes more difficult and higher local stress is needed to proceed (90). As illustrated in Figure 2-7, under frequency of 0.1Hz, the plateau of the 0.2mm wire remained mostly flat, compared to those of the 0.5 and 1mm wires, which corresponds to the lower strain rate sensitivity of the 0.2mm wire. Other than the strain rate, the transformation hardening in nitinol is a function of the internal state variables, which include the localized microstructure of the interface, grain size, and microstructural defects (133). The better heat conduction between the 0.2mm wire and its surrounding also resulted in a lower strain rate sensitivity in this wire and a more stable plateau compared to the larger ones, as shown in Figure 2-7.

Degeneration of superelasticity can also be described as a decrease in plateau stresses and the superelastic window (the difference between the upper and lower plateaus). As the microstructural damage gradually increases, the critical stress for the stress-induced transformation decreases and the hysteresis loop becomes narrower

(68,89,93). Figure 2-6 (c) showed that the upper plateau of 0.2mm, 0.5mm, and 1mm wires decreased by 13%, 18%, and 19% respectively, within the first 10 cycles. Figure 2-6 (c) indicates that the hysteresis loop narrowed by 5%, 25%, and 23% for the 0.2mm, 0.5mm, and 1mm wires, respectively. These observations also suggest that the 0.2mm wire has a more stable superelastic functionality compared to the others.

Figure 2-8 (b), (d) and (f) display the DIC map and strain progression for the 0.2mm, 0.5mm, and 1mm wires, respectively. The first martensite band in all wires did not initiate at the onset of superelastic plateau. In all wires, the first martensite band nucleated near the grips at point 2, as a result of grip pressure. This aligns with the observation by Daly et al (139) that the martensitic phase transformation begins at the grain level before macro-bands become visible. The macroscopic martensitic band expanded throughout the wire. Upon unloading, an austenite band formed and grew into the martensite, and as shown in Figure 2-8 (d), (e) and (f). At the end of the lower plateau, the wires returned to their initial austenitic state. The formation and annihilation of martensitic/austenitic bands will be examined in more detail in Chapter 4.

As Table 2-6 shows, the elastic modulus of martensite is lower than that of austenite. While the initial calculations based on statistical thermodynamics claimed that the elastic modulus of martensite is higher than austenite, the experimental results represent the opposite (140). The phase transformation in a polycrystalline superelastic nitinol never exceeds to a fully transformed martensitic state at the end of the plateau (91). The martensitic transformation continues to proceed beyond the transformation plateau in the linear elastic deformation range of martensite, which results in the lower values of martensite elastic modulus (140,141).

2.4.2 Structural Fatigue

In superelastic nitinol, functional fatigue is characterized by the gradual degradation of superelastic response of the material, due to repeated cyclic loading. Whereas structural fatigue involves crack initiation, propagation, and failure in traditional sense (58,83,87–89,95,142).

Fatigue crack initiation determines the starting point of crack growth and thus the overall fatigue life of the material (143). A proper understanding of fatigue crack initiation is important for predicting the fatigue life of a component. It has been known that surface roughness is one of the detrimental factors affecting fatigue strength (144–146). Therefore, it is important to study the effect of surface roughness on the fatigue life of the wires.

According to Roark's formula (equation 2-1), the stress concentration factor ($\mathrm{K_t}$) is a nonlinear function of the specimen notch and its geometry (147,148).

$$K_t = C_1 - C_2\left(\frac{2a}{W}\right) + C_3\left(\frac{2a}{W}\right)^2 - C_3(\frac{2a}{W})^3 \tag{2-1}$$

In this equation, "a" and "W" represent the notch length and specimen width respectively (147). In this study, "a" represents the surface defect length and "W" represents the wire diameter. Based on the Roark's formula, for the wires with similar surface quality (similar “a” value), the smaller wires are more sensitive to the surface roughness.

Figure 2-10 and result of Table 2-7 showed a considerable improvement in the surface quality of the wires after electropolishing. Figure 2-12 highlighted the significance of the surface quality on fatigue fracture surface. Fractured surfaces shown in Figure 2-12 were analyzed to characterize crack initiation and propagation features. Fatigue life mainly includes crack nucleation and growth of a fatigue crack (149). The fracture surface can be divided into two distinct regions, an area of crack initiation and fatigue crack growth (zone 1 in Figure 2-12 (a) and (d)), followed by a region of ductile tensile fracture caused by overload (zone 2 in Figure 2-12 (a) and (d)) (150,151). Beach marks and river marks are typical features of a fatigue fracture surface and reveal information about the crack growth rate and stress state during fracture (95,120,150,151). Beach marks indicate stable, slow crack growth, while river marks indicate fast, unstable rupture where the material cannot withstand the load (150,151). The non-electropolished wire had a small beach mark region (see area A in Figure 2-12 (c)), while the electropolished wire showed a larger area of crack propagation (almost all area of zone 1 in Figure 2-12 (d)). The arrows in Figure 2-12 (c) indicate the crack propagation direction. The beach marks and fatigue striations can be traced back to determine the fatigue crack origins (150,151). As expected, the non-electropolished wire showed the surface as the crack origin. It has been reported that in the heavily drawn wires, the fatigue performance of the wires is controlled by the surface defects, which mainly lead to short fatigue lives (53). Figure 2-12 (g) displays that the crack in the electropolished wire initiated from a surface inclusion.

Numerous observations have shown that fatigue crack initiation occurs at an inclusion that is located at or near the surface (78,99,152). This is due to a mechanical interaction between the surface and sub-surface inclusions, which is very detrimental to the fatigue life of the material (102). The arrow in Figure 2-12 (e) shows fatigue striations. Region A displays a secondary fatigue crack near the surface, parallel to the striations, indicating the complex tip geometry of the fatigue crack (120). Region B is probably a void caused by a non-metallic inclusion that was detached during fatigue. The stable crack propagation area of the electropolished sample (zone 1) was estimated to be 45% of the wire's total area. The river marks are clearly observed in zone 2 in Figure 2-12 (a) and (d) indicating the final catastrophic overload forces (150,151). Figure 2-12 (b) and (f) exhibit the magnified morphology of the unstable rupture regions. The arrows show the river marks and direction of crack growth. This region is characterized by elongated dimple patterns and micro-void coalescence which are common features of ductile fracture (89,150,151).

Experimental observations showed that in the electropolished 0.2mm wires, the failure happened at a surface/sub-surface inclusion near the grips, due to the mechanical interaction between the grip pressure and inclusion stress field. In Figure 2-13 (a), there are visible lines on the wire surface that are related to the damage caused by the grip (see Appendix 2-A for grip information). Figure 2-13 (b) illustrates an inclusion at the surface with a sharp corner, where a crack initiated. Around the fracture surface, similar cracks are commonly found on the circumferential surface of all wires. However, considering the stress concentration factor and the Roark’s equation (equation 2-1), these cracks are more detrimental to the smaller wires (147).

2.5 Conclusion

Superelastic nitinol wires of three different sizes were subjected to microstructural characterization and low cycle fatigue tests. The microstructural characterization results revealed that the smaller wires exhibited a higher quantity of internal cracks and defects introduced through the wire drawing process.

Surprisingly, despite the higher density of defects, the small wire exhibited better functional fatigue, which can be attributed to the cooling rate effect. However, the presence of internal cracks in small wires leads to a smaller upper stress plateau compared to larger wires.

The smaller wire also displayed higher sensitivity to surface defects, which diminished the crack nucleation stage of this wire, resulting in a decrease in its structural fatigue life (see Appendix 2-A).

2.6 Future Work

The amount of energy dissipated during the functional fatigue process can vary depending on the size of the nitinol wires. Analyzing the temperature changes over time can provide a better understanding of how wire size affects functional fatigue behavior. Therefore, the next step to compare the functional and structural fatigue of superelastic nitinol wires with different sizes can be accomplished through an infrared thermography study.

Infrared thermography is an effective technique for studying the differences in fatigue performance of wires with different sizes. This method detects temperature changes on the surface of the wire during cyclic loading, which can provide insights into energy dissipation and heat generation. Moreover, infrared thermography can also identify surface defects and cracks in the wire, providing information on crack initiation and propagation stages of the fatigue process. Overall, infrared thermography is a valuable tool for investigating the effect of wire size on fatigue performance, supplementing DIC measurements presented in this work.

The chemical composition is another important factor that significantly affects superelasticity and transformation temperatures. Conducting an Inductively Coupled Plasma-Optical Emission Spectroscopy (ICP-OES) test would be an effective way to determine the exact composition of the material and provide a better understanding of the differences between the transformation temperatures.

2.7 Research Limitations

One limitation of this study was the fatigue testing methodology. We encountered issues with the grip serrations, which led to non-uniform stress being applied to the 1mm wires and difficulty holding the smaller wires. To overcome these issues, we tested various types of grips. However, we found that bollard grips, which are commonly used for wires, were not suitable for superelastic materials due to the superelasticity that occurs around the bollard and affects stress measurements. Therefore, alternative grip designs are needed.

It should be noted that changes in grip design and the contact surface between the grip and the sample may have a significant impact on stress measurement. This highlights the need to address grip-related issues to ensure accurate and consistent results.

Our observations revealed that the composition and characteristics of nitinol wires can vary, which can affect their fatigue performance. The wires that were purchased at different times showed variations in their material properties. This highlights the urgent need to establish standardized procedures to ensure the production of more reliable nitinol wires.

Appendix 2-A

Strain Amplitude- Cycle Number Plot

The cyclic fatigue life of a material is often evaluated as the number of cycles to failure, $\mathrm{N_f}$. Experimental tests were performed at a constant frequency of 0.1 Hz under a displacement-controlled condition. As a result of functional fatigue, the lower plateau of the 0.2mm wire wires dropped below zero MPa after a few hundreds of cycles. To avoid compressive stresses, the lower strain was fixed at 30% of the plateau for all wires and the upper strain was variable. The strain amplitude was calculated as $\frac{\Delta\varepsilon}{2} = \frac{\varepsilon_{\mathrm{up}} - \varepsilon_{\mathrm{lo}}}{2}$. To avoid premature failure, the wires were electropolished using the parameters mentioned in Table 2-2.

Figure 2-15 (a) shows the self-tightening wedge grip (Mark10- G1061-2). Our initial data revealed that the serrations on the wedge grips create dents on the wires and lead to premature failure. So, a pair of wire bollard grips (Mark10-2.00G1103) was used for this experiment as shown in Figure 2-15 (b). The bollard grips are designed so that the wire can be wrapped around the bollards and clamped at one end. In this design, the wire section wrapped around bollards may undergo phase transformation as well, resulting in some shear component and spring back effects in the measured stress. To avoid these cases, the wire was not wrapped around the bollards and only the clamp part was used to tighten the wires.

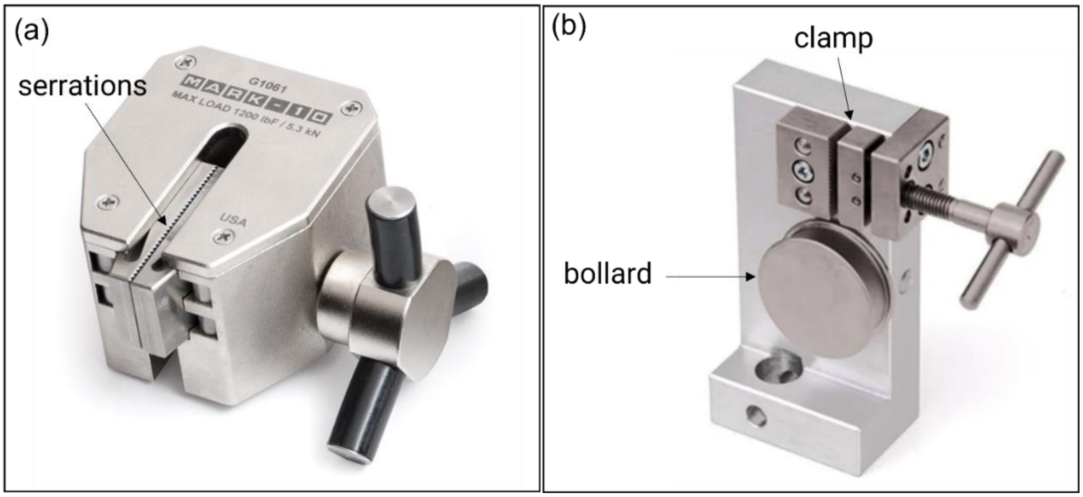

Figure 2-15- (a) wedge grip (b) bollard grip.

The strain amplitude ($\frac{\Delta\varepsilon}{2}$) versus number of cycles to failure ($\mathrm{N_f}$) plot for the 0.2mm and 0.5mm wires is illustrated in Figure 2-16. The number of cycles to failure increased as the applied cyclic strain amplitude decreased. Fractography of all the 0.2mm wires showed a surface or sub-surface inclusion at the crack initiation site. So, the failure of the 0.2mm wires involved crack initiation and propagation.

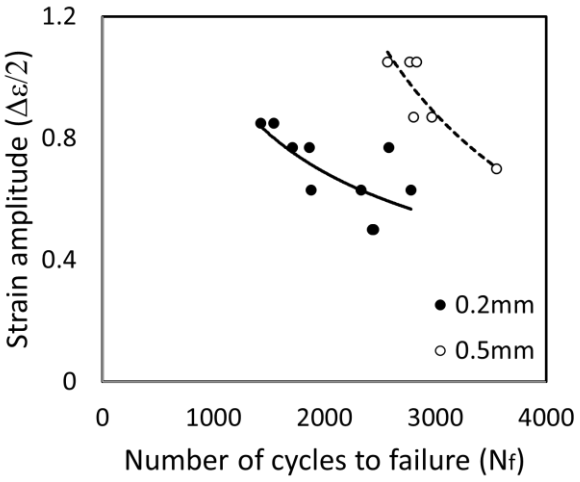

Figure 2-16-Total strain amplitude (Δε /2) versus number of cycles to failure (N_f) plot for the 0.2mm and 0.5mm wire.

However, Figure 2-17 shows that the 0.5mm and 1mm wires failed due to a surface defect. Further failure analysis revealed that the friction between grip and the wires damaged the surface (Figure 2-17 (c) and (f)), causing a premature failure. Comparing them with Figure 2-13, it is easy to see that the clamps caused less damage to the 0.2mm wire compared to the 0.5mm and 1mm wires. This could be due to the higher applied load to the larger wires. Therefore, fatigue life of the 0.5 and 1mm wire lacks crack initiation phase. Despite this, Figure 2-16 showed that the 0.5mm wires had a longer fatigue life compared to the 0.2mm wire, indicating that the crack propagation time in 0.5mm is greater than the total time of crack nucleation and propagation in the 0.2mm wire. As seen in Figure 2-17, the fracture surfaces of the 0.5mm and 1mm wires had a similar morphology to that of the 0.2mm wire. The stable crack propagation area (zone 1) in the 0.2mm electropolished wire was 45%, while it was estimated 27% and 21% for the 0.5mm and 1mm wire, respectively. Various factors may affect the stable crack growth prior to failure, such as microstructure, strength, toughness, and residual stress state. The presence of inclusions, impurities, or defects can also influence crack propagation and limit stable crack growth. Additionally, the loading conditions, such as stress intensity, also play a role in limiting stable crack growth (95,150,153). Area A in Figure 2-17 (b) and (e) show the crack initiation region. Arrow B in Figure 2-17 (b) and (e) exhibit fatigue ratcheting marks parallel to the direction of crack propagation, indicating multiple crack initiation sites (150).

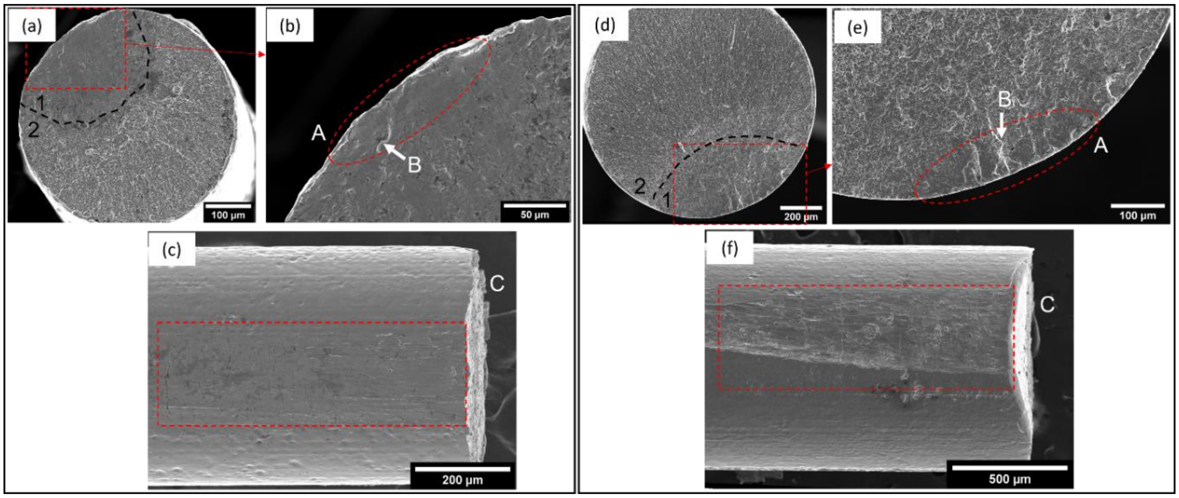

Figure 2-17- (a) fracture surface of the 0.5mm wire after fatigue (b) crack initiation site in 0.5mm wire (c) effect of grips on the o.5mm wire surface (d) fracture surface of 1mm wire (e) the crack initiation site of the 1mm wire (f) effect of grip on the 1mm wire.

Appendix 2-B

R-Phase

The nitinol wires were purchased multiple times from the same vendor. The results showed that the wires were not all the same at each purchase. This is another indication of inconsistency in superelastic nitinol design in the lack of exact standard.

Figure 2-18 displays the stress-strain behavior of the 0.2mm wire in two purchases. Although the material specifications were the same for both samples, they showed significantly different response to the applied load. One of the samples displayed a 2-step plateau which is characteristic of the presence of the intermediate “R-phase” in the initial microstructure (136,154,155).

It has been reported that other than austenite and martensite, nitinol may also present an intermediate phase with rhombohedral lattice structure, known as R-phase (136,156,157). While in the ternary systems such as Ni-Ti-Fe, Ni-Ti-Al, or Ni-Ti-Co, R-phase occur spontaneously (158), in the binary system of Ni-Ti, the R-phase may appear after the aging heat treatment of the Ni-rich alloys (136,155,157,159–162). As the Ti_3Ni_4 precipitates form during the aging treatment, the R-phase nucleates around the precipitates (160,161).

In the 2-step plateau shown in Figure 2-18, the first step of loading is associated with the $\mathrm{R} \rightarrow \mathrm{M}$, and the second step is related to the $\mathrm{A} \rightarrow \mathrm{M}$ phase transformation (136,154). It can be seen from the figure that the R-phase had a lower plateau stress level, lower Young’s modulus and less elongation compared to the austenite phase of nitinol, which is consistent with the previous studies of R-phase (136,154,155). After unloading, the mixed sample showed a large amount of residual strain, compared to the sample that was initially in the fully austenitic state. This is also consistent with the finding of Santos et al (136). Their observation showed that R-phase tends to demonstrate a shape memory effect and recovers its original state after applying heat (136).

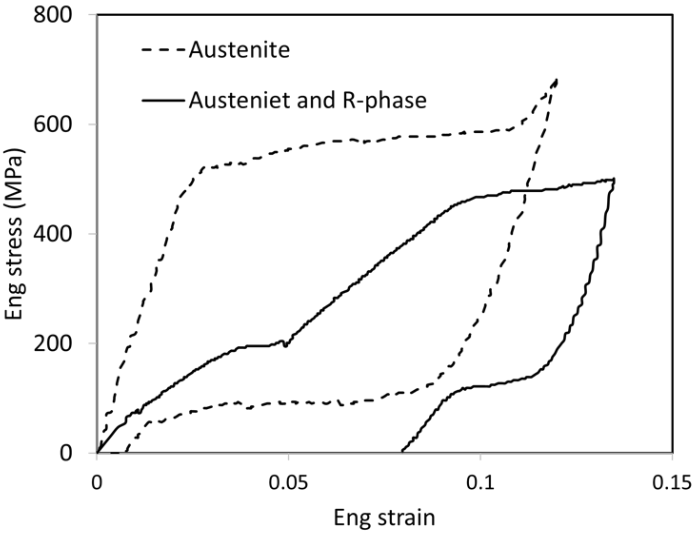

Figure 2-18- Comparison of the stress-strain behavior of the superelastic nitinol with initial austenitic state and a mixed state of austenite and R-phase.

The diffraction data were collected using a SuperNova diffractometer (Oxford Diffraction) equipped with an Atlas CCD detector. Four phi scans were performed at a scan rate of 1 deg/sec, covering both positive and negative two-theta angles. The sample was positioned parallel to the face of the detector at an omega angle of 57 deg, with a distance of 75 mm and an effective chi angle of 90 deg. Cu K-alpha radiation with a wavelength of 1.54184 Å was used.

Figure 2-19 (a) and (b) compares the DSC and XRD results of the mixed-phase wire with the fully austenitic sample. The DSC result of the sample that contained R-phase showed a 2-step transformation during cooling (Figure 2-19 (a)), but only one step was detected during the heating. This is also consistent with the finding of Santos et al (136) and Kahlil-Allafi et al (163).

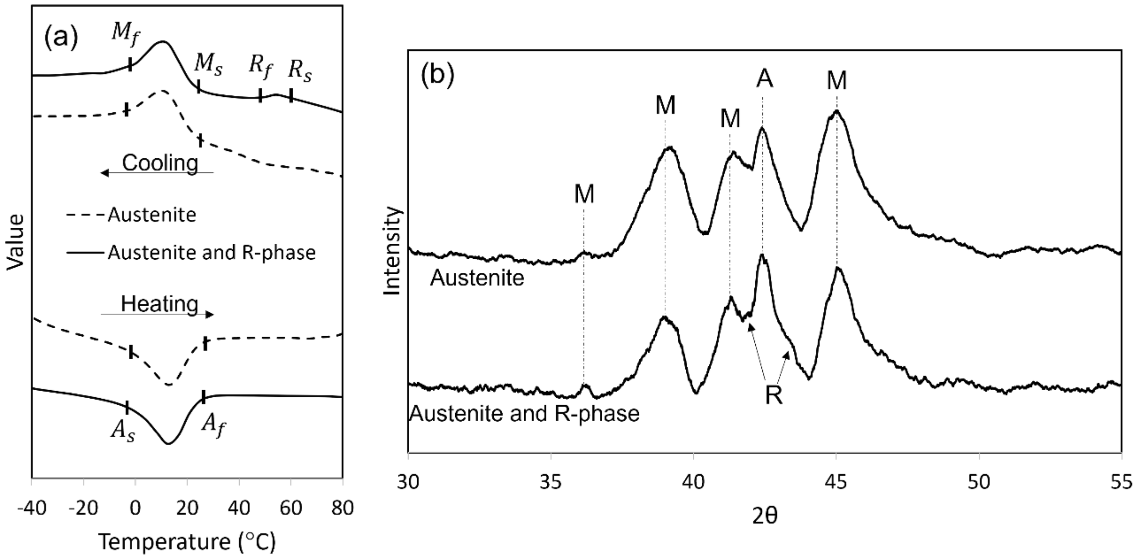

Figure 2-19- effect of the presence of R-phase on the wire, (a) DSC and (b) XRD comparison.

The XRD results of both austenitic and mixed-phase wires (Figure 2-19 (b)) displayed the presence of some martensite in the initial state of the material, denoting that the wires were under stress during the sample preparation or installation in the XRD sample holder. The austenite phase displays a peak near 42.5° (162,164,165), which splits into a double peak following formation of the R-phase (162,164,165). The arrows in Figure 2-19 (b) show the double peaks of R-phase. It is difficult to find the ratio of the austenite and R-phase in the XRD data, due to overlapping of the peaks of the two phases. However, the amount of residual strain after unloading (illustrated in Figure 2-18) is proportional to the quantity of R-phase in this sample (136).

3 MICROSTRUCTURAL EVOLUTION OF SUPERELASTIC NITINOL UNDER FATIGUE: INSIGHTS FROM 3-D X-RAY CHARACTERIZATION

3.1 Introduction

2-D images only contain information about the surface of a sample (166–169) and the surface microstructure does not reveal the true number density, morphology, and distribution of defects in three dimensions (167,170–172). To obtain the 3-D geometry of the inclusions, the crystallographic orientation of the material surrounding them and the lattice strain around non-metallic inclusions, a microstructural characterization via two synchrotron-based X-ray methods will be employed before and during fatigue testing. First, absorption-contrast X-ray micro-tomography (μ-CT) scans was conducted to locate the positions of the nonmetallic inclusions and the other microstructural defects. Then, far-field high energy diffraction microscopy (ff-HEDM) experiments was carried out to obtain 3-D orientations of the grains along with the elastic strain measurements.

3.1.1 Literature Review

The μ-CT system can reveal the internal microstructure of samples by capturing 2-D images from different angles (173). This system utilizes X-rays to generate cross-sectional images of physical objects (173–175). The 2-D images can be processed using reconstruction software to create a comprehensive 3-D model of the scanned object, which can be further refined and analyzed in a digital environment for research, design, and simulation purposes (173,175). Given its non-destructive and high-resolution imaging capabilities, the μ-CT system has become an essential tool in numerous fields, including materials science, engineering, biology, and medicine (173–175). Its use has enabled researchers to gain valuable insights into complex structures and has opened up new avenues for exploring the microscopic world (173–175).

Figure 3-1 shows the four steps of imaging in μ-CT technique. In step A, a series of X-ray images are taken of the object as it rotates. The object is rotating at a small angle for each image acquisition, resulting in a set of 2-D images of the object at different angles (step B). Then the images are processed through a computer algorithm to reconstruct the stack of the cross sectional images (step C). The final output of the tomography process is a 3D image of the object that can be visualized and analyzed (step D) (173–175).

However, the μ-CT technique is unable to detect crystallographic orientations of the grain structure. Such orientations are often closely linked to material properties. Therefore, while tomography techniques are valuable tools, they may not provide a complete picture of a material's characteristics (176,177).

HEDM is an advanced technique capable of characterizing the microstructure of large polycrystalline aggregates at the grain length scale with sensitivity to crystallographic orientation (177). This non-destructive method provides high-resolution information about the internal structure of materials, enabling researchers to study the fundamental mechanisms that govern the behavior of materials under various conditions (176–178). The far-field HEDM technique can be utilized to study properties of individual grains within a polycrystalline material and measure the 3-D position, volume, orientation, and elastic strain of the individual grains (179–181). On the other hand, the near-field HEDM technique can be used to map the spatial distribution of grain morphologies (177,179).

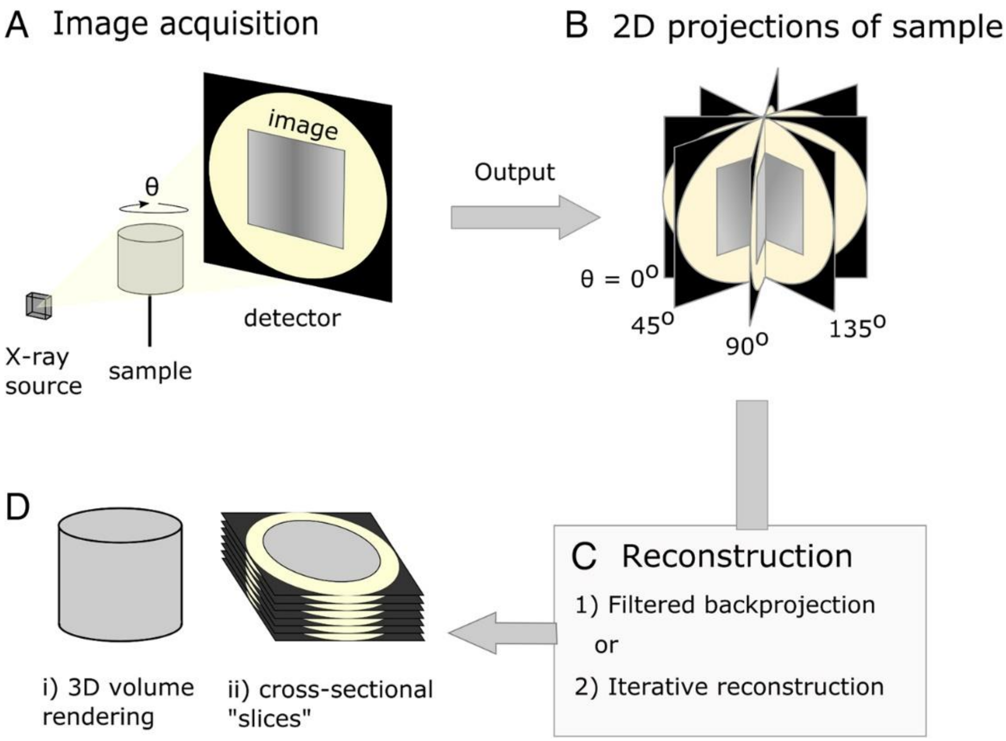

Figure 3-1- Schematic of X-micro-computed tomography steps, (A) image acquisition as the sample rotates, (B) 2-D projections of the sample are rendered, (C) reconstruction (D) 3-D model of the object (175).

Figure 3-2 shows the schematic of ff-HEDM and nf-HEDM. The far-field detector is positioned approximately 1 meter away from the sample, and it is utilized for collecting ff-HEDM data. The near-field detector, on the other hand, is located 5-15 mm from the sample (179). As the sample rotates 360º in ω, data is collected from multiple diffraction patterns, which are then used to reconstruct the 3-D orientation of the grains (179).

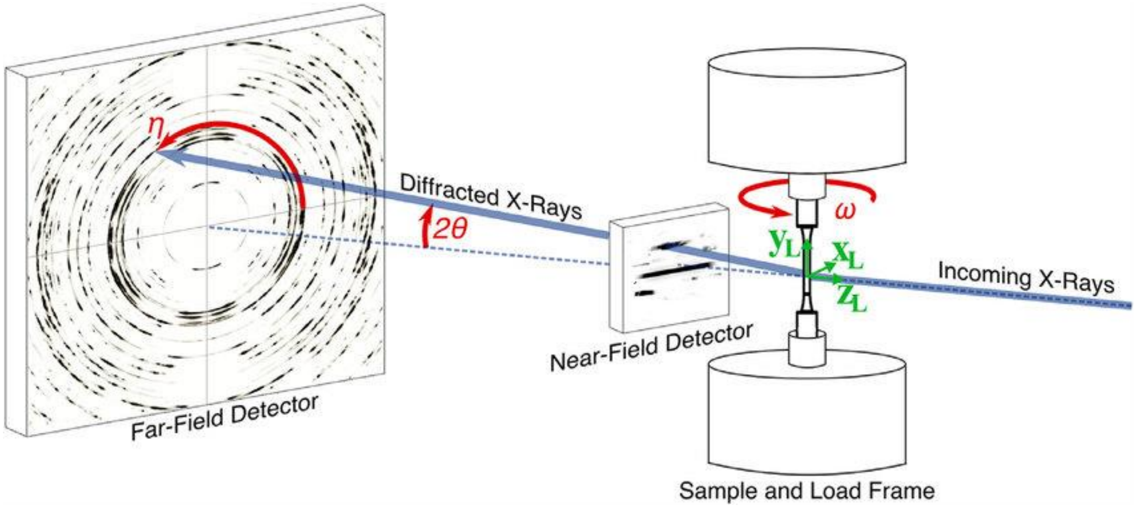

Figure 3-2- Schematic of experimental setup in ff-HEDM and nf-HEDM (179).

The HEDM technique has been used to study the grain-scale evolution of numerous materials, including steel (182,183), Ni superalloy (184), copper (185) and titanium (186) under applied loads. In the case of superelastic nitinol, there have been relatively few studies that focused on the phase transformation at the grain-scale. Paranjape et al (72) studied intragranular heterogeneity in the phase transformation of superelastic nitinol under an applied load. They utilized ff-HEDM technique and showed that heterogeneity in the phase transformation of the grains arises from their microstructural constraints, such as grain orientation and neighboring interactions (72). They reported that the higher number of the neighboring grains may bring more constraint to the grain transformation, resulting in a higher amount of heterogeneity in the grains (72). Other than grain boundaries and texture, the microstructural features such as inclusions, precipitates and the intermediate R-phase are also considered as microstructural constraints that impact granular heterogeneity in superelastic nitinol specimens grains (72,81).

In another study, Paranjape et al combined ff-HEDM and modeling techniques to analyze the effect of micron-sized inclusions on martensitic transformation of a lab-grown single crystal nitinol with multiple subgrains (81). They showed that the stress state near the inclusions affects the activation of martensite variants, leading to increased heterogeneity in the vicinity of the inclusions (81). Although this work by Paranjape et al shed light on the effect of inclusions on the activation of martensite variants in a nitinol single crystal, the impact of stress state on the inclusions in a polycrystalline material has yet to be studied. In this research, the ff-HEDM technique was combined with μ-CT to investigate the effect of the inclusions in a polycrystalline material, as they are commonly used in practical applications.

The ff-HEDM technique is effective in characterizing the microstructure of the materials that have a relatively large grain size (72,177). A strong crystallographic texture or a higher number of the grains can increase the likelihood of spot overlap (177,187). Intensity of the spots is proportional to their relative grain volume (177,188) and the detectable grain size distribution is limited by the dynamic range of the area detector (177). Therefore, if the grain size is small in a polycrystalline specimen, the grains may not be detected by ff-HEDM and can potentially disappear from the resulting microstructure characterization (72,177).

Figure 3-3 displays the schematic of martensitic transformation at the grain size level in a polycrystalline material. It has been shown that in a polycrystalline material, a complete transformation implies that around 60-70% of the volume has undergone the transformation process (91). During the phase transformation, unfavorably oriented grains may never go through phase transformation and the favorably oriented grains may only exhibit partial transformation (72,91). The HEDM technique is capable of detecting and differentiating between grains and subgrains based on their crystallographic orientation (187). The schematic of grain transformation under load is depicted in Figure 3-3 (b). When under load, the partially transformed grains are divided into martensite and austenite subgrains. Even the fully transformed grains are refined into martensite domains with different orientation, which are separated by interdomain interfaces (schematically shown in an enlarged grain in Figure 3-3 (b)) (189). After unloading, a high density of dislocations remain in the austenite grains (90,190,191), which interact and entangle with each other, leading to the formation of sub-boundaries and low angle grain boundaries within the austenite grains (192,193), as schematically displayed in Figure 3-3 (c). Furthermore, after each cycle, some retained martensite can remain in the material (91).

Thus, due to the complex nature of the superelastic transformation, a superelastic nitinol material typically maintains a mixed grain-sub grain texture after a severe cold deformation (194). Therefore, for the ff-HEDM experiment, a minimum initial grain size distribution of 30-40µm is preferred.

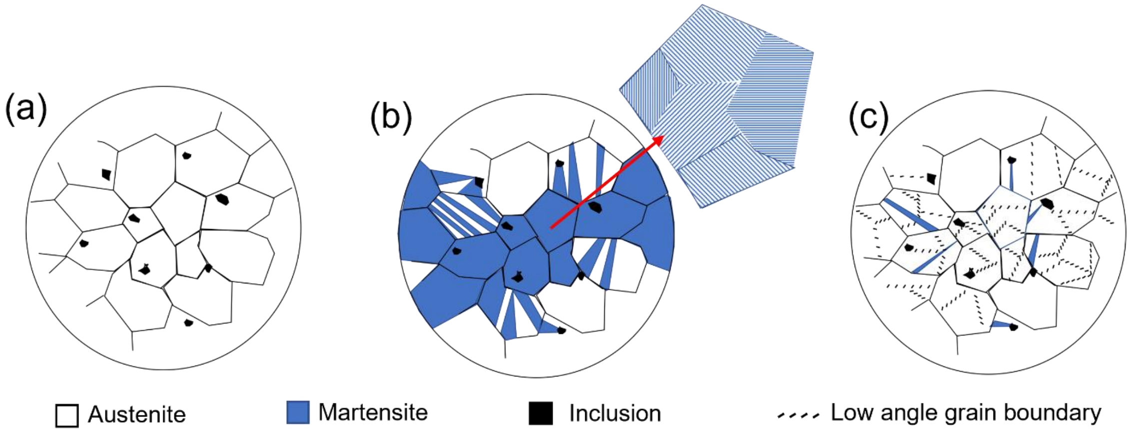

Figure 3-3- Schematic of martensitic transformation and grain refinement in superelastic nitinol, (a) pre-cycling, (b) under load, a transformed grain is enlarged to show the martensite variants with different orientation within one grain, (c) the subgrains inside the austenite grains after unloading, adapted from G. Eggeler et al (88).

In this chapter, the 3-D X-ray techniques will be utilized to study the effect of cycling on the microstructure of superelastic nitinol.

3.1.2 Objective and Goal

The inevitable manufacturing defects introduced by the production process leads to a decrease in the fatigue performance and creates a large variation in the fatigue life (195). It has been shown that the crack nucleation sites are usually connected to the surface and internal defects such as notches, inclusions, and voids (144). The fatigue data indicates that larger defects are associated with a shorter fatigue life (196)**.** However, post-mortem fractography shows that the initiating defect is not always the largest defect (197). It also has been acknowledged that the proximity of the inclusions to the surface plays a role in the fatigue life. The optical or electron microscopes only deliver 2-D images that contain limited information about the surface of a sample (166,170,197–199). The 3-D characterization techniques are needed to achieve a full dataset of the density, location, geometry, and possible connectivity of the defects (123,200,201). I hypothesize that the size, density, and location of the microstructural imperfections significantly affect the phase transformation and fatigue behavior of a superelastic nitinol specimen. To verify this hypothesis, 3-D synchrotron X-ray methods such as ff-HEDM and μ-CT were utilized. The combination of these two techniques allowed for the observation of the microstructural evolution of superelastic nitinol around inclusions and internal voids at the grain-scale level (202).

3.2 Experimental Procedure

The original goal of the research was to examine the effects of cyclic loading on nitinol wires. However, in order to meet the requirements of the Advanced Photon Source (APS), a particular sample design was needed, which can be seen in Figure 3-4 (a). For this purpose, a cold-rolled superelastic nitinol sheet with a thickness range of 3.99mm-4.11mm and an A_f temperature range of 10±5ºC was purchased from Edgetech Industries. To prepare the samples for the study, electrical discharge machining (EDM) was employed parallel to the rolling direction of the sheet. EDM is a precise machining method that uses a series of electric sparks to erode the material and create a desired shape with tight tolerances (203). Figure 3-4 (b) shows the sample after EDM process.

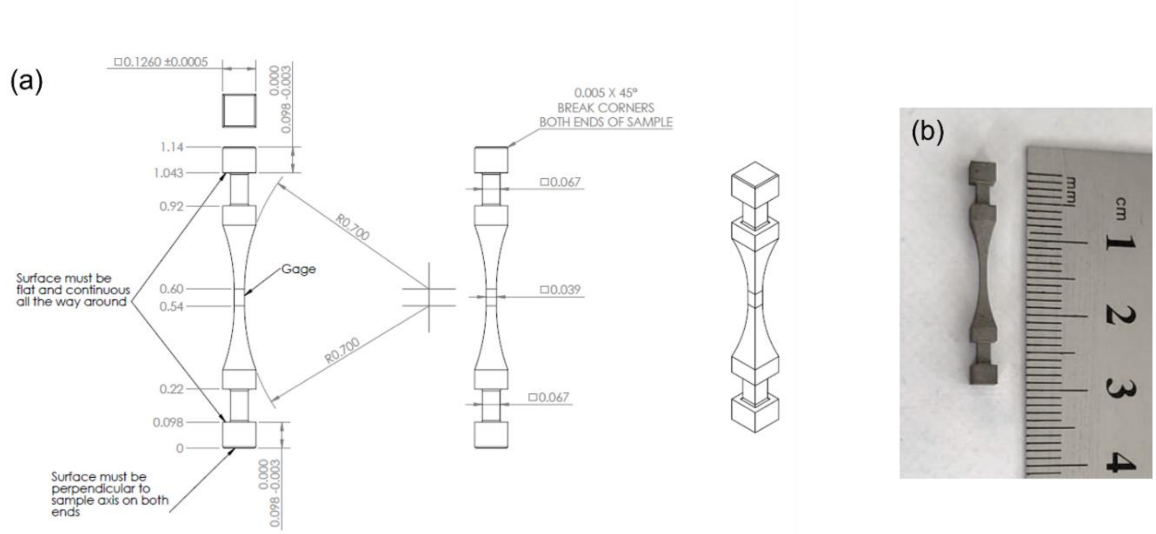

Figure 3-4- (a) sample geometry, (b) the sample after EDM.

The as-received specimen had a nanoscale grain size distribution. Therefore, a heat treatment procedure was implemented to grow the grains. The vacuum-encapsulated specimens were placed in a resistance furnace and heated at a rate of 10ºC/min and maintained at 850ºC for 2 hours. Afterwards, they were water quenched. The backscattered electron (BSE) SEM images were used to observe the grain boundaries after the heat treatment.

To improve the surface quality of the samples after EDM, the electropolishing procedure was applied using the setup described in Chapter 2, Section 2.2. The samples were electropolished under 0.5A current until a desired surface quality was achieved. SEM images were used to examine the surface quality of the samples after surface treatment. The tensile behavior of the annealed and non-annealed samples were collected using the Mark10-ESM750 (displacement resolution 0.001 inch or 0.0254mm) tensile test stand and MR01-750 (load resolution 0.5 lbf or 2.2241 N) load cell. The experimental procedure outlined in Section 2.2 was followed to create the speckle pattern and the DIC data acquisition. Stress-strain curves were generated for both annealed and non-annealed samples. Stress was calculated by dividing the load (taken from the Mark-10 instrument) by the surface area of the gauge section, and the strain was determined by averaging the strain distribution over the DIC map.

The ff-HEDM experiments involved mounting the sample in a compact load frame and illuminating it with monochromatic X-rays with a wavelength of 0.172978nm and an energy of 71.676 keV. A single layer scan of the 1mm tall region at the gauge center was conducted using a 1mm tall beam. The images were recorded at a 0.1° step size on a GE5.EDF detector positioned 924mm away from the specimen.

The annealed sample was subjected to an in-situ tension experiment under stress-controlled conditions, ranging between 0-400MPa. The crosshead speed was set to 0.001mm/s. During the first cycle, ff-HEDM data was collected at loading stresses of 100, 200, 300, and 400 MPa. Upon unloading, ff-HEDM data was collected as the stress reached 300, 200, 100, and 0 MPa. Subsequently, the data was collected at the maximum load of 400MPa and unloaded states of the cycle 2, 3, 4, 10, 100, 500, 1000, 1100, 1200, 1300, 1400, 1500 and 1600. At Cycle 1600, the maximum applied load was increased to 450 MPa, which led to the sudden failure of the specimen.

The ff-HEDM data of the non-annealed sample was collected under the same loading conditions for 400 cycles. The data was collected at the maximum and minimum loads during the first 10 cycles, and subsequently collected every 100 cycles at the 100th, 200th, 300th, and 400th cycle.

The Microstructural Imaging using Diffraction Analysis Software (MIDAS), developed by APS was used to analyze the ff-HEDM data of the annealed sample. MIDAS was used to obtain information about the grain size, centroid, orientation, and grain strain tensor (177). A 3-D polycrystal (Voronoi tessellation) image with the dimensions of 0.2mm×0.2mm×0.2mm was developed using the open-source Neper[3] software. Due to the large number of grains in the non-annealed sample, the package was not able to distinguish and process the diffraction spots of the grains, as the technique had a limitation in this regard (72,177). The diffraction images of both samples were processed using HEXRDGUI[4]. To avoid the potential impact of internal residual strain that formed after EDM, the lattice parameter of the austenite phase was determined by analyzing the diffraction pattern of the annealed sample. Similarly, during the initial loading of the non-annealed sample, the martensite lattice parameters were determined using HEXRDGUI.

The μ-CT technique was utilized to monitor the microstructural evolution of the specimen while the sample was under cyclic loads. The PG1 high-resolution tomography detector, with a spatial resolution of approximately 3μm was used. The sample was rotated over a 360º angular range and images were captured in 0.1º steps. The initial tomography data acquisition was performed on the pre-cycling annealed sample. Subsequent scans were taken only at the maximum load for the 1st, 10th, 100th, 500th, 1500th, and 1600th cycles, where cracks were open and easier to detect. The tomography data were reconstructed using a MATLAB code for image reconstruction developed by

---

[3] https://neper.info/

[4] https://github.com/HEXRD/hexrdgui

APS and GRIDREC algorithm. The open-source software TOMVIZ[5] was used to visualize and analyze the 3-D tomographic images. The SEM images were utilized to conduct a fractography analysis on the failed annealed sample.

3.3 Results

Figure 3-5 shows the grain structure in 1mm wire after the grain growth heat treatment. In Figure 3-5 (a), the black arrows depict the precipitates that formed after the heat treatment. After polishing, the experimental observation showed that some grains on the surface of the sample transformed into martensite due to the applied load during mechanical polishing. In Figure 3-5 (b), grains A and B in Figure 3-5 (b) remained in austenitic state and did not show martensite variants, while arrows C, D, E and F indicate the martensitic grains with different orientations. The same heat treatment procedure was applied to the APS sample.

Figure 3-6 compares the tensile behavior of the samples before and after grain growth heat treatment, collected using Mark-10 stand. Both samples displayed a similar behavior until 400N applied load. The annealed sample exhibited the characteristic of a brittle material, a linear elastic region followed by a sudden failure at 500N. While the non-annealed sample showed a small plateau near 370N, as indicated by an arrow, followed by a significant plastic deformation region.

---

[5] https://tomviz.org/

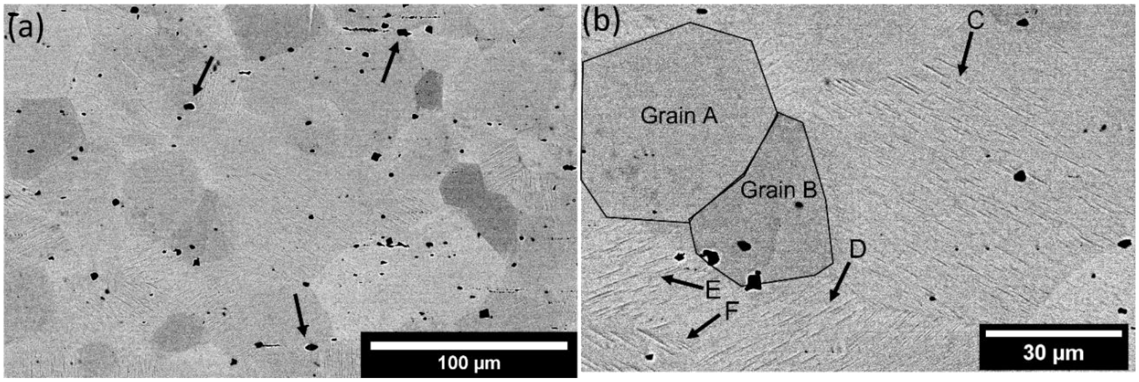

Figure 3-5- (a) The grain structure after the grain growth heath treatment in 1mm wire, (b) enlarged section of the image that highlights the austenite grains and differently oriented martensite grains.

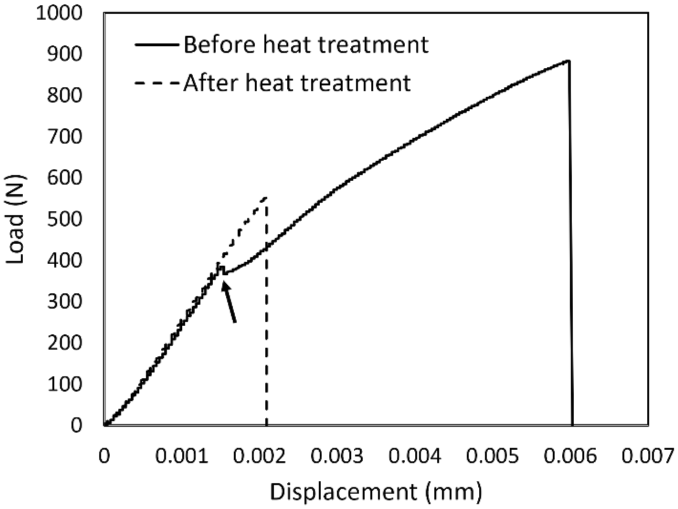

Figure 3-6-comparison of the tensile behavior of the annealed and non-annealed samples.

Figure 3-7 compares the DIC strain measurement of the gauge section of the samples, before and after annealing. The samples were cycled under stress-control between 0-400N. Comparing the DIC maps revealed that the annealed sample showed slightly less strain than the non-annealed one at 400N load. Figure 3-7 (e) displays the stress-strain behavior of the samples until failure.

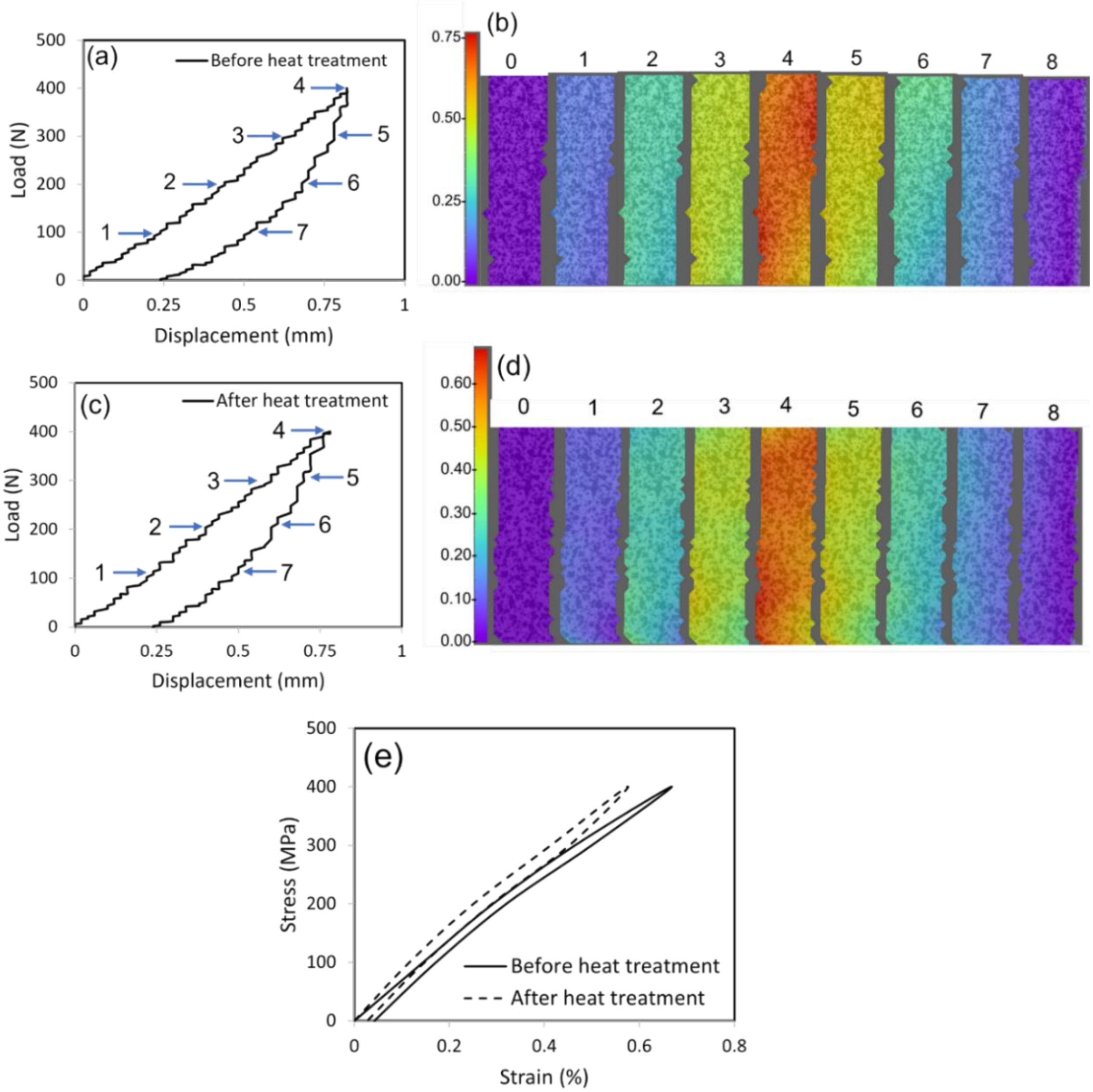

Figure 3-7- DIC images stress controlled 0-400, (a) the load-displacement curve of the non-annealed sample, (b) the DIC map of the non-annealed sample, (c) the load-displacement curve of the annealed sample, (d) the DIC map of the annealed sample, (e) the stress-strain curves of the samples.

Figure 3-8 compares the full ring diffraction pattern of the sample before and after the grain growth heat treatment. In both patterns, the diffraction spots fell on the Debye-Scherrer rings of the cubic austenite. The (110), (200) and (211) rings are illustrated in Figure 3-8 (a) and (b). However, both patterns were missing the (100), (111) and (210) rings. The non-annealed sample had a 4-fold symmetric diffraction pattern at the A(200) ring, while the annealed sample showed a random pattern of the grains. Additionally, the annealed sample exhibited a more spotty pattern and a lower number of grains compared to the non-annealed one. The lattice parameter of the annealed austenite sample was determined to be 3.014A using the diffraction pattern of the annealed sample.

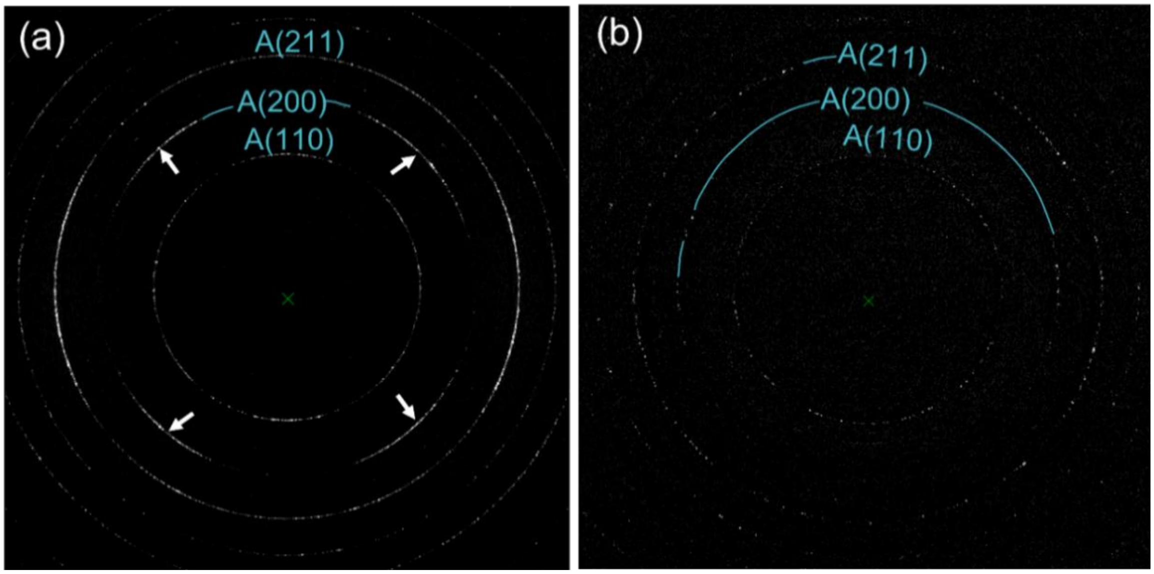

Figure 3-8- The diffraction pattern of the (a) not-annealed and (b) annealed sample, pre-fatigue.

A stress-controlled cyclic load between 0-400MPa was applied to the annealed sample. Figure 3-9 presents the change in diffraction spots of the annealed sample during the first cycle. The stress-strain curve shown in Figure 3-9 (b) is taken from Figure 3-7 (e). Three A(211) grains were selected to closely follow the change in their diffraction pattern during the loading and unloading steps of the first cycle. The results of Figure 3-9 indicated that the size and intensity of the diffraction spots changed as the material was under load. Upon loading at 100MPa load, there was no significant change in the pattern of the three grains. At 200MPa load, the size of spots decreased while the number of spots increased, and this trend continued as the load increased. It is possible that the high intensity spot observed at the 400MPa cycle is the result of overlapping several spots. There was no indication of martensitic phase transformation upon loading the annealed sample, as evidenced by the absence of a martensite ring in the diffraction pattern of the loaded material. In Figure 3-9 (h), (i) and (j), it can be observed that the number of spots gradually decreased, as the load decreased. At the end of the cycle (Figure 3-9 (k)), the three grains were recovered. However, three additional small spots were also observed near A(211) ring.

A close examination of the diffraction pattern showed that when the material is under load, the Debye-Scherrer rings shift towards a larger radius. To further investigate the shift in spot position during the cycling, grain 2 of Figure 3-9 (c) was enlarged in Figure 3-10. Figure 3-10 (b) shows shift in the position of the spots as well as increase in their number as the material is under load. After the first unload, the spot shifted back to the initial Debye-Scherrer ring position, but the number of the spots was not the same as the pre-cycling condition.

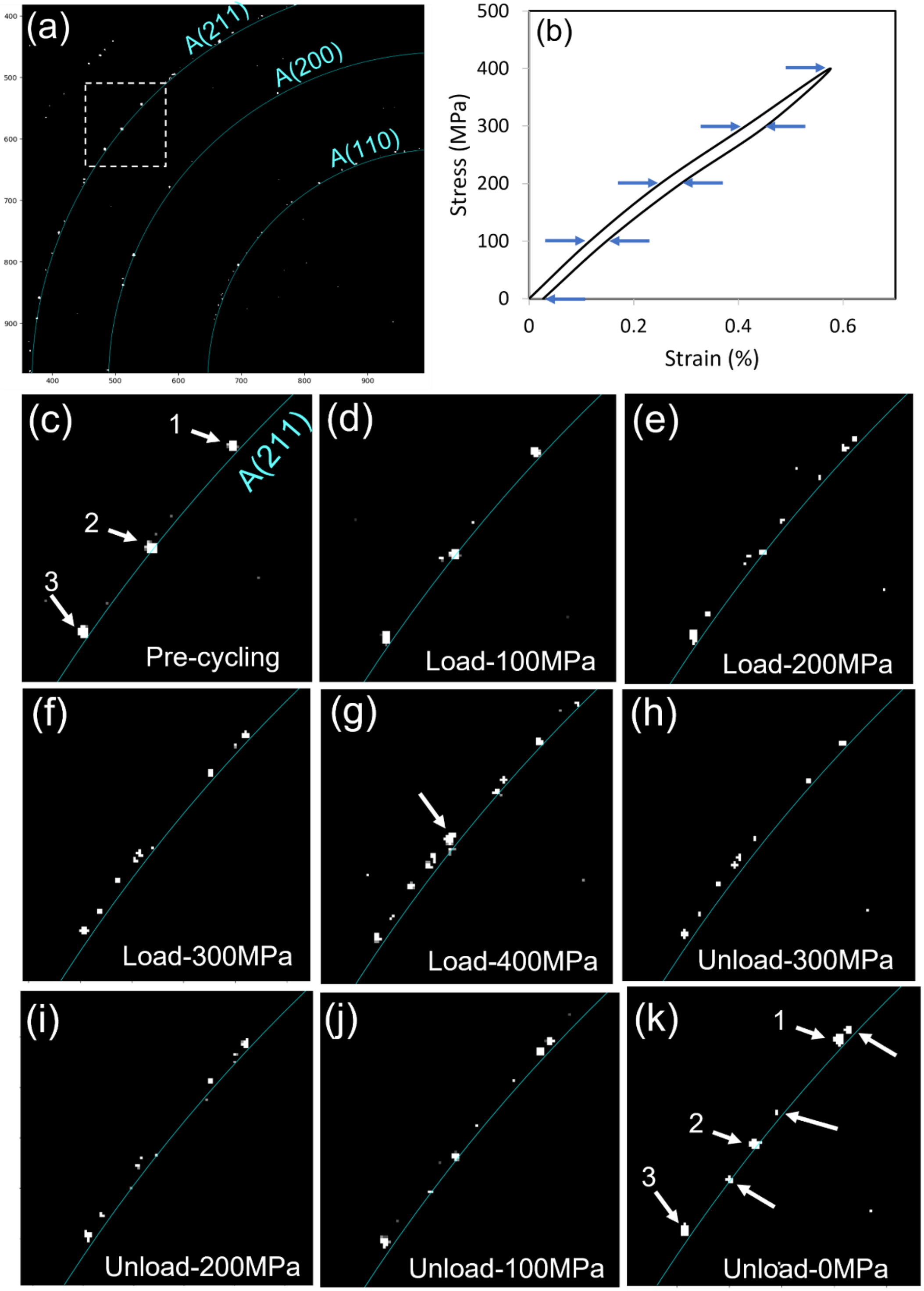

Figure 3-9-First cycle of the heat treated sample (a) the first three Debye-Scherrer rings, (b) stress-strain curve of the 1st cycle, enlargement of three grains (c) pre-cycling, (d) loading under 100MPa, (e) loading under 200MPa, (f) loading under 300MPa, (g) peak load at 400MPa, (h) unloading under 300MPa, (i) unloading under 200MPa, (j) unloading under 100MPa, (k) end of the 1st cycle.

The subsequent cycles exhibited the same trend. At the 1600th cycle, the applied stress was increased to 450Mpa, resulting in a larger shift of the Debye-Scherrer ring position and ultimately leading to sample failure. Figure 3-10 (i) showed that the spots did not shift back to their initial position after the 450 MPa stress. Furthermore, under 450MPa stress, the spots were elongated in the radial direction of the Debye-Scherrer ring.

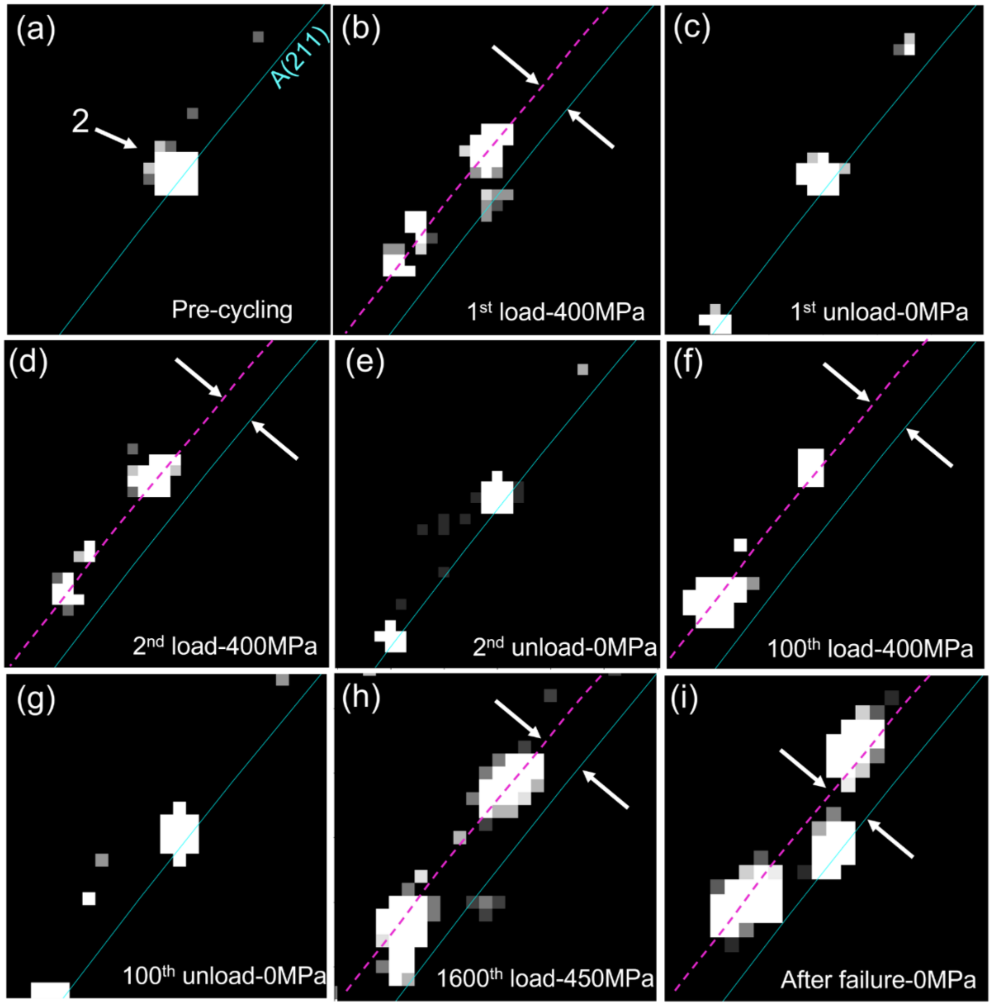

Figure 3-10- Shift in spatial position of grain 2, annealed sample (a) pre-cycling, (b) first load peak at 400MPa, (c) first unload, (d) second load at 400MPa, (e) second unload, (f) 100th load at 400MPa, (g) 100th unload, (h) 1600th load where the stress increased to 450MPa, (i) after failure at 1600th cycle.

Figure 3-11 (a) displays the HEXRD diffraction pattern of the non-annealed sample before cycling.

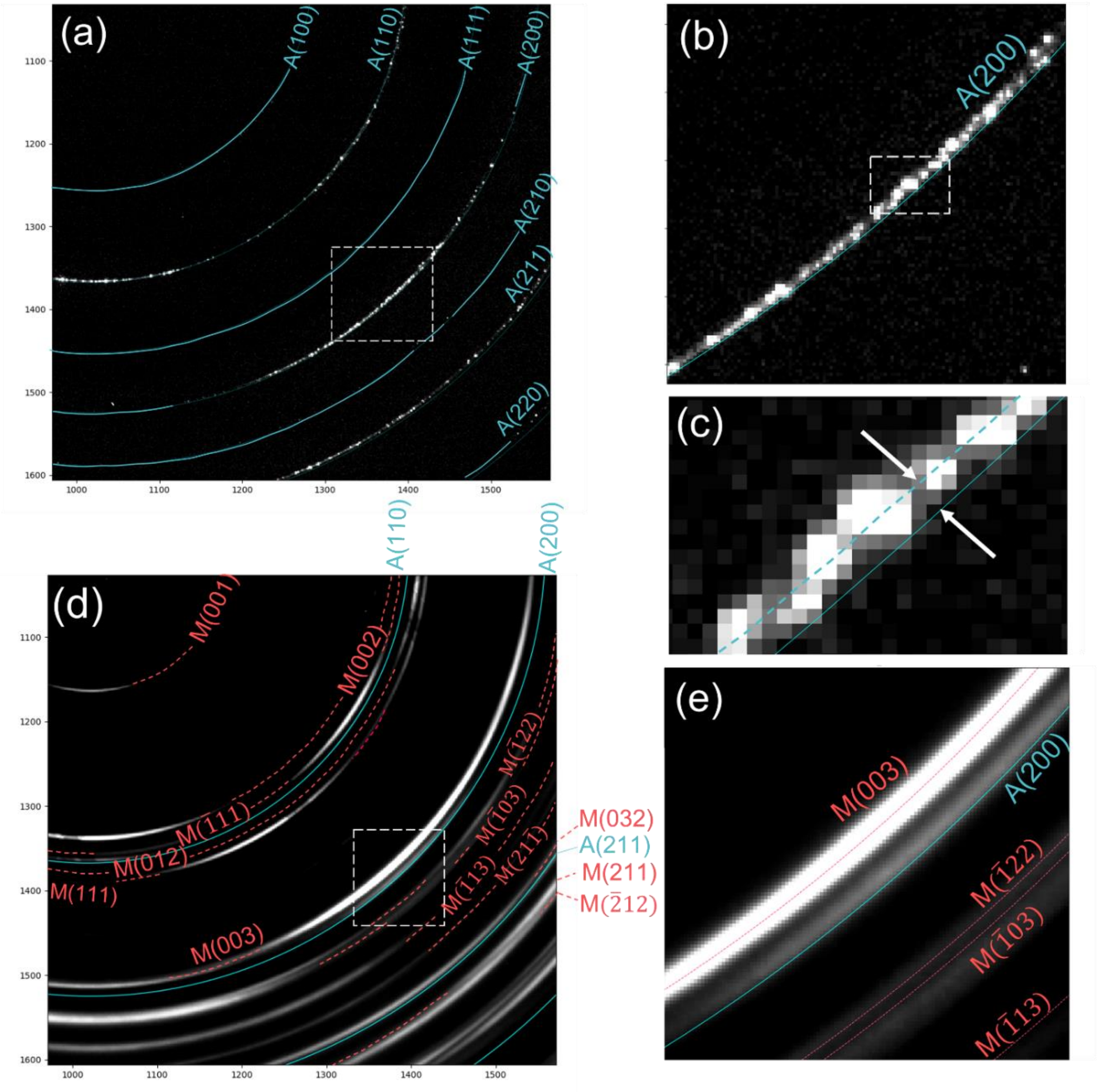

Figure 3-11- Diffraction pattern of the non-annealed sample (a) pre cycling, the specified region is enlarged at (b), (c) a (200) grain of austenite, (d) loaded sample, the specified area is magnified at (e).

As shown in this figure, the diffraction peaks of the grains fell approximately on the reference Debye-Scherrer rings of cubic austenite. The diffraction spots were located on the (110), (200), (211) and (220) rings of austenite, while the (100), (111) and (210) were empty. The specified area of Figure 3-11 (a) is enlarged in Figure 3-11 (b). Figure 3-11 (c) illustrates the magnified reflection of a set of (200) grains. The figure revealed that prior to cycling, the grains were shifted to a slightly smaller ring radius. The solid line represents the location of the Debye-Scherrer rings for a cubic austenite with a lattice parameter of 3.014A, whereas the dashed line indicates the location of the shifted diffraction spots. The diffraction pattern of the sample at the first load (under 400N tensile load) is shown in Figure 3-11 (d). This figure illustrates that as the austenite rings faded, there was a noticeable increase in the intensity of the martensite rings. Unlike the pre-fatigued sample (Figure 3-11 (a)) that had a spotty pattern, the diffraction pattern under load showed a smoother pattern (Figure 3-11 (d)). The outlined area of Figure 3-11 (d) is enlarged in Figure 3-11 (e).

Table 3-1 displays the lattice parameters of both austenite and martensite, as measured using HEXRDGUI. The martensite lattice parameters were determined during the first load of the non-annealed sample.

Table 3-1- lattice parameters of austenite and martensite phases

Phase	a	b	c	α	β	γ	crystal system
Austenite	3.014	3.014	3.014	90	90	90	cubic (B2)
Martensite	2.79	4.41	4.68	90	97.6	90	Monoclinic (B19’)

Figure 3-12 shows a full map of the diffraction pattern observed in the non-annealed sample at the first load. The diffraction pattern reveals the presence of the martensite phase with a 2, 4 and 6-fold symmetry.

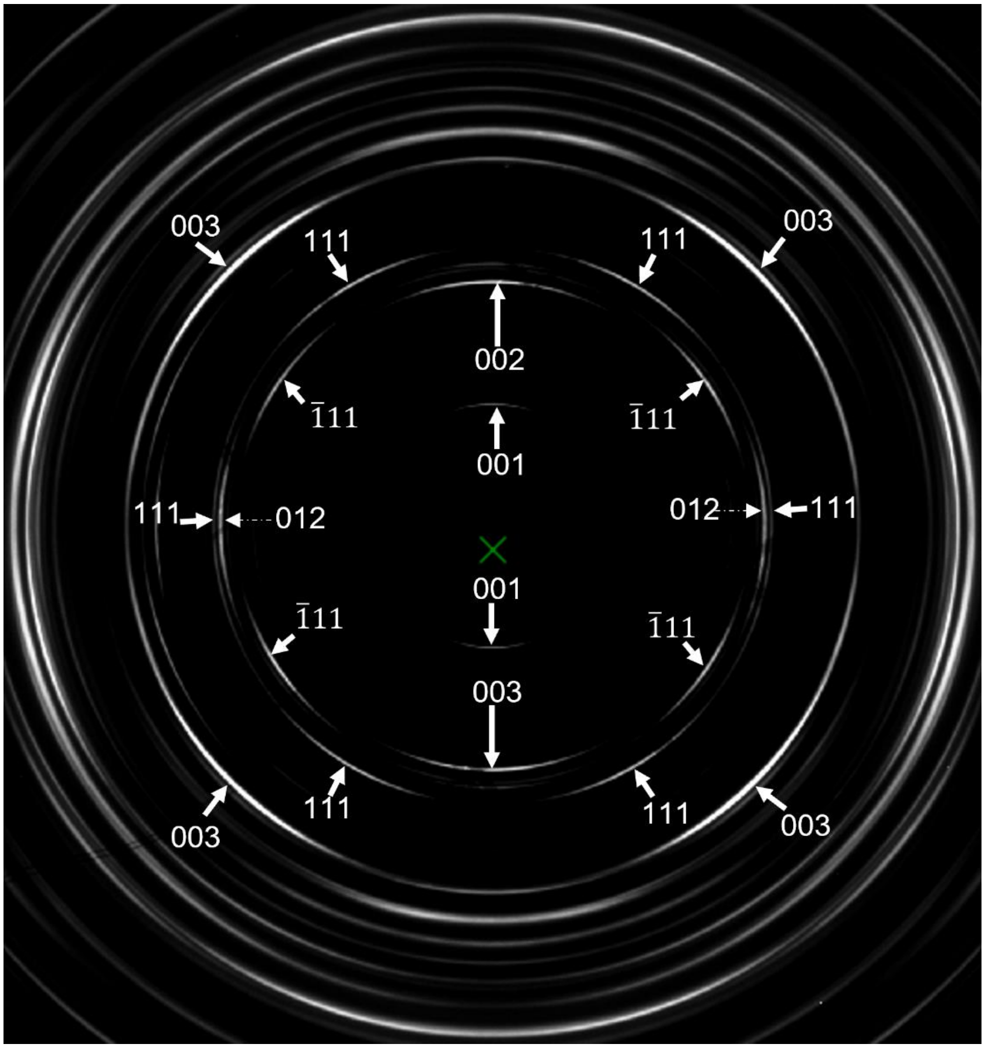

Figure 3-12- Symmetries in the diffraction pattern of monoclinic martensite phase, the first load of the non-annealed sample.

Figure 3-13 compares the diffraction patterns of the 1st, 4th, 100th and 400th cycles in loaded and unloaded states. Upon the first load, the spotty pattern changed to a more diffused pattern. The reflections of the martensite peaks can also be seen in Figure 3-13 (e). As shown in Figure 3-13 (b), the diffraction ring in the unloaded state of the 4th cycle displays a more dispersed pattern compared to the pre-fatigued one, with a noticeable ring broadening effect. Additionally, Figure 3-13 (b) displays the reflection of M(003) peak. At the loaded state of the 4th cycle (Figure 3-13 (f)), the austenite and martensite coexist. As the cycle number increased, the peak of A(200) in the unloaded state weakened, and the M(003) peak became more intense. At the unloaded state of the 400th cycle, the A(200) peaks showed a very low intensity and it fully disappeared upon loading. A broadening of the martensite peaks was also observed in the loaded and unloaded states of the 400th cycle.

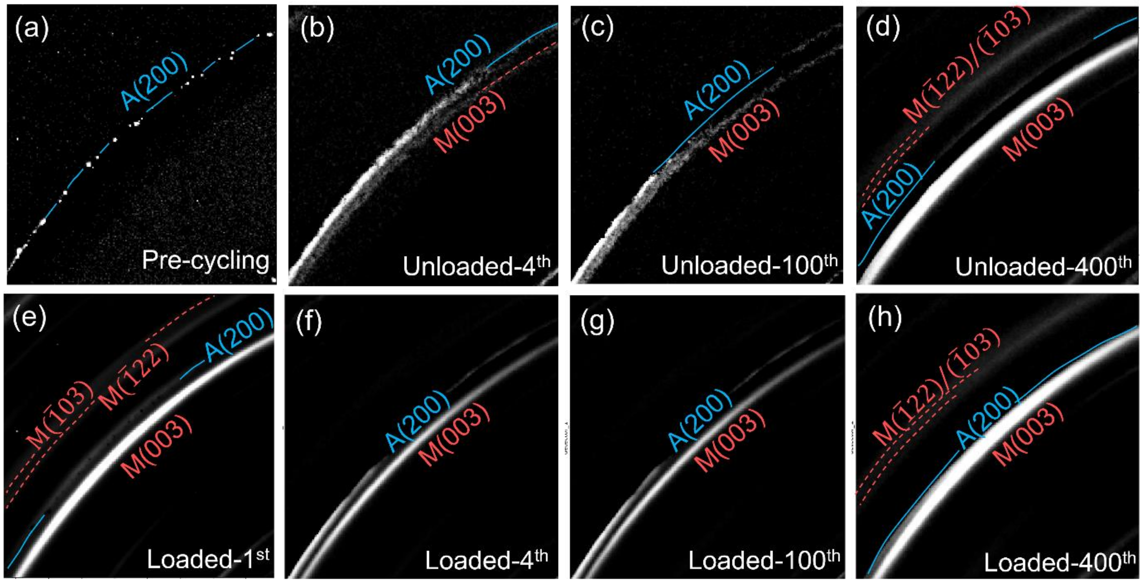

Figure 3-13- The diffraction pattern of the not-annealed sample (a) pre fatigue, unloaded state of the (b) 4th, (c) 100th, (d) 400th cycle, the loaded state of (e) 1st, (f) 4th, (g) 100th and (h) 400th cycles.

Figure 3-14 displays the Voronoi tessellation image of the annealed sample before cycling. MIDAS detected 91 grains in the cube shown in Figure 3-14. Since the sample was in annealed condition, it does not include any subgrains. Based on the MIDAS results, the grain size for this sample was in the range of 77-186µm.

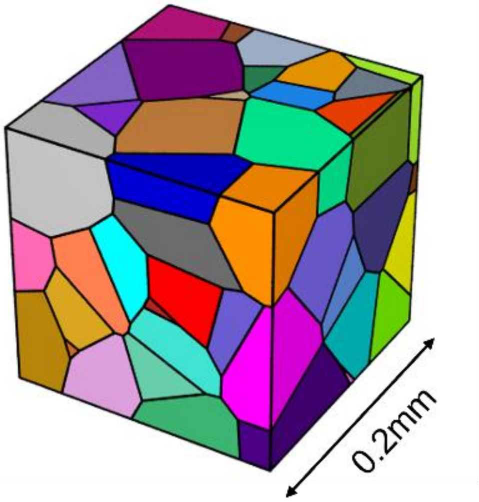

Figure 3-14- A Voronoi tessellation of the annealed polycrystalline sample prior to cycling, different colors represent different grains.

Figure 3-15 (a) and (b) display the SEM micrograph and the reconstructed tomography image of the non-annealed sample after the surface treatment, respectively. While the non-annealed sample exhibited a uniform and smooth surface, the surface treatment procedure in the annealed sample resulted in a pitted surface as shown in Figure 3-15 (c) and (d).

As shown in Figure 3-16, the internal damage and defects formed within the initial cycles and gradually increased by increasing the cycle number. The sudden increase in the applied stress at the 1600th cycle resulted in formation of several cracks that mainly initiated at the surface of the specimen. The results revealed that propagation and coalescence of cracks “A” and “B” led to the final failure. Crack “C” was the only internal crack that was observed within the sample. Figure 3-17 (a) presents the solid form of the annealed sample at the last cycle. Figure 3-17 (b) and (c) show the top and front view of the specimen, respectively.

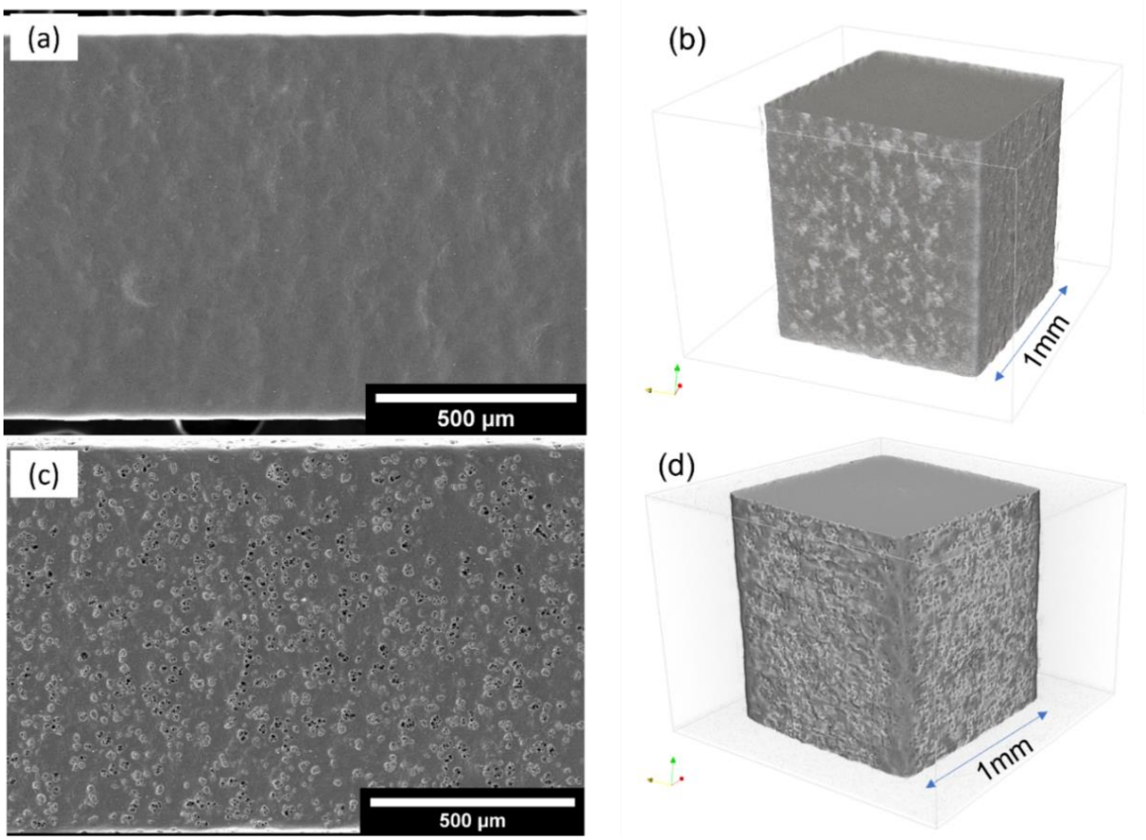

Figure 3-15- (a) SEM image of surface of the non-annealed sample (b) 3-D tomography image of the non-annealed sample (c) SEM micrograph showing surface of the sample after annealing and surafce treatment (d) 3-D tomography image of the sample.

Figure 3-18 shows the SEM image of the fracture surface of the annealed sample after failure at 1600th cycle. The location of the cracks “A”, “B” and “C” are illustrated in the figure. It can be observed that there are multiple surface crack initiation sites present on the fracture surface. The river marks can be seen as shallow grooves on the surface. The ratcheting marks, where the cracks merge together, are highlighted with white arrows.

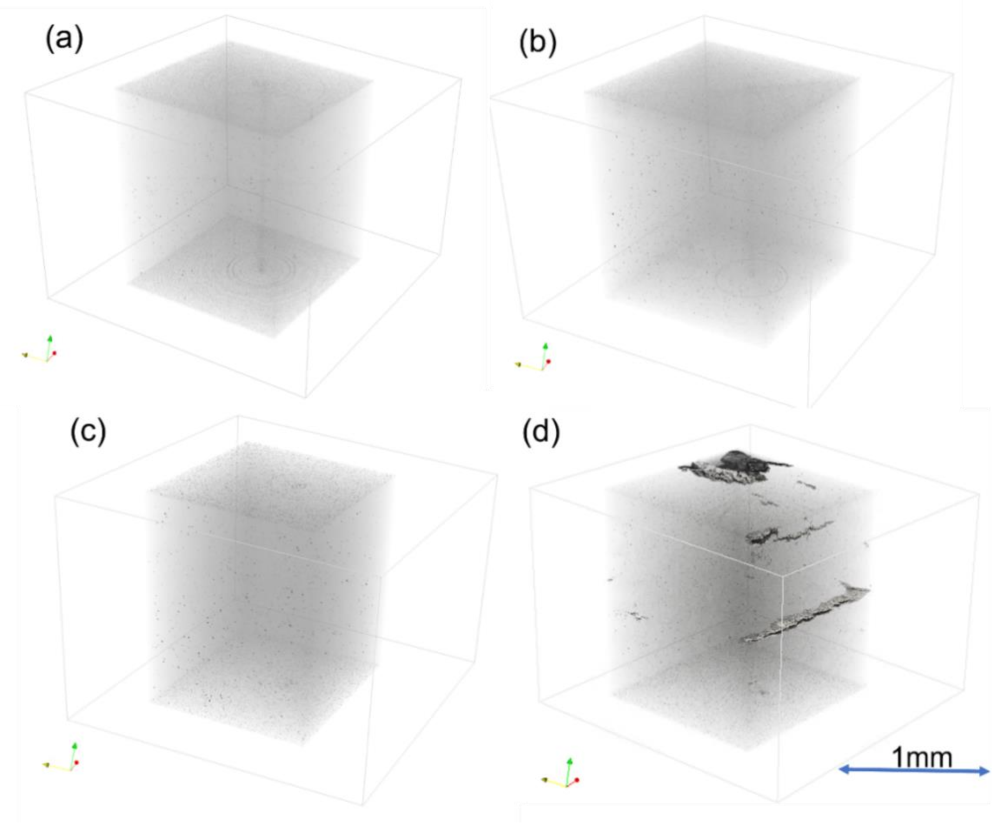

Figure 3-16-Tomography images of the internal defects of the annealed sample (a) pre cycling, (b) 10th cycle, (c) 1500th cycle, (d) 1600th cycle.

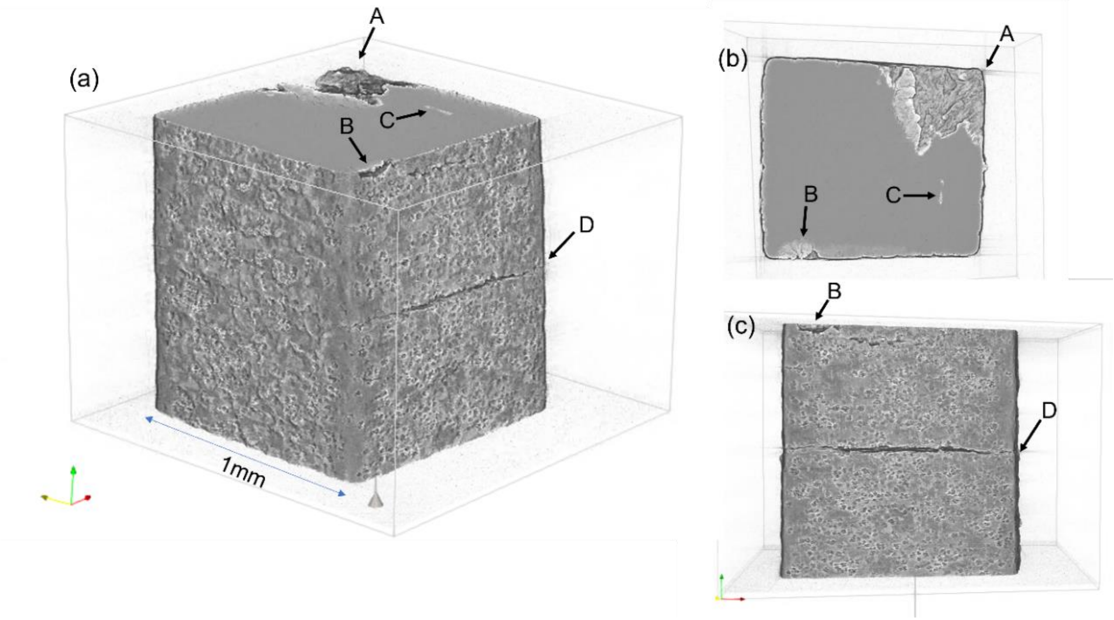

Figure 3-17- (a) the solid form of the annealed sample at the 1600th cycle, when the cracks formed, (b) top view, (c) front view.

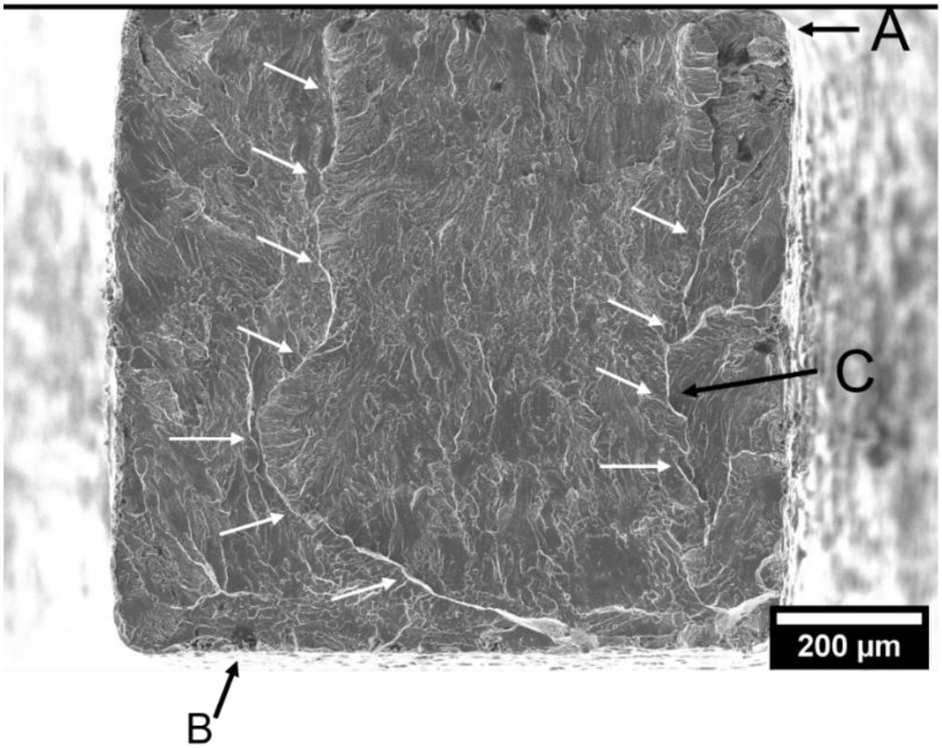

Figure 3-18- fracture surface of the annealed sample.

3.4 Discussion

3.4.1 Annealed Sample

As seen in Figure 3-6, the annealed sample exhibited the characteristics tensile behavior of a brittle material. Numerous studies have confirmed that there is an optimal grain size range for nitinol to display the desired superelastic performance (204–210). For the best superelastic behavior, the average grain size should be below 200 nm, but not significantly smaller than 100 nm (211,212). From Figure 3-5, the average grain size of the material after grain growth heat treatment can be measured around 40µm, which is significantly above the mentioned range. It has been reported that decrease in the number of the grains suppresses the phase transformation (204). The martensite nucleation rate is significantly affected by the grain boundaries (213). In larger grain sizes, the number of grain boundaries is decreased, which results in fewer sites for martensitic nucleation and suppression of the phase transformation (204) (213). Therefore, it is expected that after grain growth heat treatment, the superelastic performance of the material drops. Figure 3-5 also shows numerous large precipitates that formed during the heat treatment. Although the stress concentration near the defects and inclusions assist the martensitic transformation (83,84,103), the non-deformable large precipitates also resist shearing by stopping or deflecting the slip bands (214,215). Large precipitates potentially acted as constraints at phase interfaces and contributed to the poor transformation response (81). Several factors can contribute to a reduction in the ductility of a material during heat treatment, assuming that the chemical composition of the samples remains unchanged. These include the effect of microstructural defects that can cause the material to transition from superelastic to brittle as well as the grain size effect, as described by the Hall-Petch equation ($\sigma = \sigma_0 + \frac{K}{\sqrt{d}}$) (216). In this equation, σ_0 is the original yield stress, d is the average grain diameter and K is constant. As displayed in Figure 3-6, the non-annealed sample showed a small plateau region under applied load, indicating a weak superelastic response at the room temperature. The superelastic response of a material can be affected by numerous factors, such as its composition and transformation temperatures (19,37,38). However, the phase transformation is highly dependent on the crystallographic orientation and the defect structure of the material as well (217–219). It has been shown that the transformation strains in single-crystal nitinol are the highest near the <111> directions, intermediate for the <110> directions, and lowest for the <100> directions (72,220,221).

The diffraction pattern of the annealed sample during the first cycle (Figure 3-9) did not reveal any signs of phase transformation, which is consistent with the result of the tensile test (Figure 3-6). However, as shown in Figure 3-9, applying load to the annealed austenite resulted in a smaller spot size and a greater number of the grains. These observations suggest grain refinement of austenite phase under applied load (192,193). When a polycrystalline nitinol component goes through martensitic phase transformation or severe deformation, each austenite grain breaks down into a complex microstructure consisting of martensite variants and sub-grains (179,189). The grain refinement at the first cycle implies formation of high density of dislocation and probably small martensite planes within the austenite grains (192,222).The grain refinement in one cycle implies that the phase transformation occurred on a smaller scale, possibly involving small martensite variants within each grain. However, it did not generate high intensity martensitic spots in the diffraction pattern, indicating that the volume of the martensite variants was too small to be detected by the HEDM detector. The ff-HEDM technique has a spatial resolution of 10 µm (177). Therefore, the size of martensite variants are likely smaller than 10 µm.

As illustrated in Figure 3-10, the diffraction pattern of the annealed sample showed that under load, the spots shifted to a larger ring radius, implying tensile strain, and upon unloading, the spots returned to their initial location. The subsequent cycles displayed the same behavior until Cycle 1600, at which the load was increased to 450N. Increasing the applied load led to an increase in the ring shift. Under 450N (or 450 MPa) applied load, multiple cracks formed at the surface of the material (Figure 3-16 (d)), which ultimately led to the failure of the specimen. As shown in Figure 3-10 (i), the Debye-Scherrer ring did not shift back to its initial location after failure, implying that the grains did not recover the deformation that was applied by the 450N load. The 450N load also caused a change in the spot shape, resulting in elongated spots in angular direction of the ring, showing a higher level of distortion in this cycle (81).

Figure 3-14 depicts Voronoi tessellation of the annealed sample before cycling, including 91 grains that were detected by the MIDAS software within a cube volume of 0.2mm×0.2mm×0.2mm. The ff-HEDM technique is not sensitive to the grain shapes in a polycrystalline material (177), so shape of the grains is not estimated. The technique is capable of measuring the grain radius and the grain centroid with spatial resolution of

10µm (177). After 1600 cycles, MIDAS only detected 5 grains within this region of the specimen due the grain refinement effect that was observed in Figure 3-9 and Figure 3-10.

3.4.2 Non-Annealed Sample

Depending on the fabrication process (such as drawing, rolling, and extruding) and heat treatment, different crystallographic textures may form in polycrystalline nitinol samples (217,223). Typically, the drawing and rolling processes used to create nitinol wires, sheets, tubes and bars result in a dominant texture along the drawing direction (217,220,224). The diffraction pattern in Figure 3-8 (a) displays a discontinuous and 4-fold symmetry in the non-annealed sample before fatigue, indicating a preferentially aligned texture in specific directions (225,226), resulting from the sheet rolling process. The texture disappeared after the heat treatment, as shown in Figure 3-8 (b), and was replaced by a random distribution of grains resulting from recrystallization and grain growth processes (227,228). The large spotty pattern of the annealed sample in Figure 3-8 (b) indicates a relatively large grain size with random orientation in this sample before the fatigue test (229).

According to the extinction rule for the B2 lattice structure with (hkl) planes, a plane will appear in the diffraction pattern if the sum of its Miller indices (h+k+l) equals 2n, where n is an integer (230). As a result, in the diffraction patterns displayed in Figure 3-8, peaks corresponding to the (110), (200), and (211) planes are observed, while peaks for the (100), (111), and (210) planes are absent.

The diffraction pattern of the non-annealed sample is shown in Figure 3-11. It can be seen in Figure 3-11 (c) that the rings are slightly shifted toward a smaller Debye-Scherrer ring radius, implying a residual compressive strain in the material after EDM (231). Upon loading, this sample displayed the diffraction pattern of the monoclinic martensite phase, as shown in Figure 3-11 (d). The smeared appearance of the peaks denotes that the material is under deformation (193). The high intensity of the martensite peaks in this diffraction pattern suggests a noticeable phase transformation during the first cycle. The extent of peak broadening is related to the density, nature, and distribution of defects within the material (193,218,232). As exhibited in Figure 3-12, Debye-Scherrer rings of a deformed monoclinic lattice exhibit symmetric intensity variations and discontinuities due to the presence of residual strain within the crystal lattice (189). The reflections are particularly strongly spread in specific directions. The monoclinic lattice structure is characterized by a 2-fold symmetry (233). However, the 4- and 6-fold symmetries were also observed in the diffraction pattern of the martensite phase, as shown in Figure 3-12, resulting from the twinning and detwinning of the monoclinic lattice (178,218,234,235). It has been shown that deformation twinning occurs in oriented martensite if the applied stress exceeds the yield point of superelastic nitinol (236–238). However, there is an intrinsic coupling between stress-induced martensitic transformation and deformation twinning in the martensite phase (237). Presumably, the deformation twinning forms within the stress-induced martensite bands, where the localized stress exceeds the yield stress (218,236). The deformation twinning in martensite phase involves dislocation slip (218,236–238) and the transformation induced plasticity proceeds via deformation twinning in martensite in superelastic nitinol (237). It has been shown that the deformation twins do not transform back to the parent phase and remain in the microstructure after unloading (236,238–240).

Figure 3-13 shows effect of cycling on diffraction pattern of the non-annealed sample. The spotty pattern of Figure 3-13 (a) confirms that the grains of the pre-cycling specimen were free of dislocation defects and internal strain (189). At the first load, the diffraction reflections exhibit a more diffuse pattern, indicating either plasticity or grain refinement (192,193). The formation of low-angle grain boundaries and sub-grains impacts the diffraction pattern immediately after the initial cycles. This is due to the changes in the crystallographic orientation of the material, leading to a different scattering behavior (189,192). The grain refinement is also an indication of inhomogeneous martensitic transformation within the grains. Based on the study of Paranjape et al (72), it is expected that in the non-annealed sample, the higher number of grains and greater number of neighbors lead to a higher degree of heterogeneity, resulting in faster grain refinement, compared to the annealed sample.

The broadening of the diffraction reflections suggests that there may be small distortions and rotations occurring within the lattice (179). This occurrence is closely associated with the applied strain (179,232). The unloaded state of the 4th cycle (Figure 3-13 (b)) shows a new low intensity reflection appeared that was not present before cycling, corresponding to M(003) reflection of retained martensite phase. After the initial load, the austenite rings did not return to their original spotty pattern, suggesting permanent grain refinement, the formation of new grain boundaries, and changes in the grain structure after only one loading cycle. When comparing the loaded state of the 1st and 4th cycles (Figure 3-13 (e) and (f)), it was observed that the 1st cycle exhibited a more intense martensite ring and a higher degree of transformation compared to the 4th cycle. At the 4th load, the austenite ring did not entirely disappear, implying an incomplete phase transformation. The retained austenite at the loaded state suggests that some austenite was unable to transform to martensite, which is due to the dislocation and defect formation in the microstructure that promotes slip and inhibits transformation in some grains (241). Figure 3-13 (c) and (d) showed that the intensity of the austenite peak at the unloaded state decreased as the cycle number increased, suggesting a reduction in the amount of austenite in the sample. At the unloaded state of Cycle 400 (Figure 3-13 (e)), the faint austenite peaks and pronounced martensite peaks indicated a high amount of residual martensite after 400 cycles, implying functional fatigue of the material (217). The broadened ring pattern of the martensite after 400 cycles suggests that the microstructure became gradually refined down more and more (189). This is consistent with the process of fatigue and plastic deformation, which can lead to dislocation accumulation and grain refinement in the material over time.

Due to the overlapping of diffraction spots from a large number of grains, the ff-HEDM technique cannot characterize the microstructure of non-annealed sample with a small grain size (72,177).

3.4.3 Micro-Computed Tomography

As shown in Figure 3-15 (c) and (d), after surface treatment of the annealed sample, pits of various sizes and shapes were identified on the surface. This suggests the likely presence of multiple compounds on the surface of the specimen with different corrosion rates, possibly due to variations in crystalline orientation or localized chemical compositions after the heat treatment (242,243). The surface features did not exist at the surface of the non-annealed sample, denoting that the heat treatment procedure likely changed the chemical composition of the material. Formation of the large Ni_3Ti, Ni_3Ti_2 or Ni_4Ti_3 precipitates (as shown in Figure 3-5) may change the concentration gradient in the austenite matrix (244,245). This process may drain Ni at the surrounding matrix of the precipitates, resulting in an uneven distribution of Ni throughout the sample (245–247). It can also lead to an increase in the temperature of the martensitic transformation (247). This factor may also explain the brittle behavior of the annealed sample, shown in Figure 3-6.

The tomography images of Figure 3-16 demonstrate the gradual accumulation of microstructural damage over time. Following the sudden increase in the applied stress, the specimen failed at the stress level of 450MPa, significantly below the failure stress of the material under tensile load, shown in Figure 3-6. This observation can be explained by the fact that as damage accumulates, the material becomes weaker and less capable of withstanding the applied stress, leading to a lower tensile failure stress. Figure 3-16 (d) displayed that the cracks mainly initiated at the surface of the specimen, due to the stress concentration at the surface defects of the annealed sample (144–146). Except for crack “C”, all cracks that formed at the 1600th cycle were initiated at the surface, as exhibited in Figure 3-17. Crack “A” showed rapid propagation and joined other developing cracks, resulting in the failure of the specimen. Figure 3-18 shows the SEM image of the fracture surface. Observation of the river marks (indicating fast and unstable rupture), and absence of beach marks (sign of stable crack growth) is consistent with the sudden failure observed after load increment (150,151). The ratchet marks that are shown with white arrows implying the intersection of multiple cracks that have initiated in multiple locations and propagated through the materials (150).

3.5 Summary and Conclusion

Due to the limitation of ff-HEDM technique, a grain growth heat treatment was employed, resulting in a grain size increase within the range of 77-186μm. While the annealed sample showed a brittle tensile behavior after the heat treatment, the diffraction results suggested the likelihood of martensitic transformation occurring at the grain size scale, leading to grain refinement during the cycling. No martensite peak was detected after loading the annealed sample. However, the shift in the position of the diffraction peaks indicate the presence of strain or defects in its crystalline structure.

The loading of the non-annealed specimen was accompanied by the appearance of the martensite reflections, significant peak broadening, and grain refinement, all corresponding to the functional fatigue of the material. Grain refinement can indicate inhomogeneous phase transformation within the grains and formation of the low angle grain boundaries.

While the inability to perform 3-D measurement on the wires used in the study may limit the scope of the findings, it is still possible to draw general conclusions about the behavior of superelastic nitinol based on the results obtained. Regardless of the sample geometry, the superelastic properties of nitinol are highly dependent on its microstructure, which is influenced by its composition and thermal history. In this study, the grain growth heat treatment resulted in the formation of precipitates, which likely altered the composition of the material and affected its superelastic temperature range.

In Chapter 2, the functional fatigue was linked to the cooling rate effect and the latent heat of transformation. In Chapter 3, the functional fatigue was correlated to the grain refinement. The previous studies have shown that the residual strain (an indication of functional fatigue) rises with increasing the strain rate and the testing temperature (134,248). Therefore, it can be concluded that the poor heat conduction (lower cooling rate) between the sample and the environment may result in higher grain refinement during cycling.

3.6 Future Work

The next step to answer the research questions is to merge the results of ff-HEDM and tomography; and analyze the local strain and phase transformation near the internal defects of the specimen. The 3-D Voronoi tessellation image was only generated for the annealed sample, which did not exhibit any superelastic behavior in its diffraction patterns. However, the grain refinement confirmed that the transformation happened at the small scales. To address the research question of this chapter, it is necessary to monitor the process of grain refinement occurring in the grains surrounding the inclusions.

To address the challenges posed by grain refinement during fatigue in superelastic nitinol, combining ff-HEDM with other characterization techniques such as TEM or EBSD may be a useful approach. While ff-HEDM can struggle to detect grains as they become finer and more uniformly distributed, TEM and EBSD offer high-resolution imaging and orientation mapping capabilities that can help to track the evolution of the microstructure over time.

The heat treatment performed during this research led to the loss of superelastic behavior in the material, as well as the formation of large precipitates that led to the brittleness of the material. Therefore, it is recommended that future studies aim to address this issue by improving the furnace conditions and optimizing the heat treatment parameters.

3.7 Research Limitations

The initial objective of the research was to investigate the impact of cyclic loading on nitinol wires. However, due to the requirements of the test setup at APS, a specific sample geometry was needed, as depicted in Figure 3-4. This imposed the use of nitinol sheets instead of wires, as they were better suited for the required sample geometry.

Preparing the sample for ff-HEDM may be challenging, particularly in the case of superelastic nitinol, which can be difficult to machine or polish without introducing artifacts or damaging the material. The ff-HEDM technique requires relatively large grain sizes, but superelastic behavior weakens as the grain size increases above 200-300nm.

As the material is subjected to repeated loading and unloading cycles, the grains progressively decrease in size due to deformation-induced transformation. During fatigue cycling of the nitinol specimen, this grain refinement can create difficulties in detecting grains using ff-HEDM. The technique may struggle to accurately measure the size, strain, and orientation of the grains over time as their diffraction spot overlaps.

4 INVESTIGATION OF THE MACROSCOPIC MARTENSITE BAND FORMATION AND THE LOCALIZED DEFORMATION

4.1 Introduction

As previously observed in Chapter 2, the wires with different sizes showed a different functional fatigue performance under load. The geometry and microstructure of the wire play a key role in this difference (139). Since the microstructural defects and martensitic band formation in superelastic nitinol are interrelated, this chapter is dedicated to investigating the relationship between the microstructural features, geometry (wire size) and macroscopic behavior of the superelastic nitinol wires.

In this chapter, a 3-D digital image correlation (DIC) system was used to examine the formation of martensitic bands and the accumulation of non-homogeneous defects at a macroscopic level in all three wires.

4.1.1 Literature Review

The DIC system is a non-invasive tool that provides an accurate method for measuring full-field deformation and strain of the materials in real-time during load-unload cycles (115,116).

Figure 4-1 shows schematic of martensite band formation and annihilation during one load-unload cycle. Figure 4-1 (a) illustrates the initial austenitic microstructure of a superelastic nitinol material with its inherent inclusions. The presence of small inclusions alters the stress distribution within the material and assist the martensitic transformation (83) (90) (190). As shown in Figure 4-1 (b), the martensite variants appear at the corner of the inclusions (83) (139) in well-oriented grains (72) (91) (249). As the formation of a martensite variant begins in a well-oriented grain, the local stress state of the grain changes and triggers transformation in neighboring grains as well (91). Therefore, as shown in Figure 4-1 (c), the transformation that initiated in a favorably oriented grain, spreads to the less favorably oriented ones (91). This process continues until the macroscopic martensite bands form. As seen in Figure 4-1 (d), a great number of dislocations form at the austenite-martensite (A/M) interface to compensate for the unmatched deformation resulting from the difference in crystal structure and lattice mismatch between the two phases (90) (190) (191). Upon unloading, the A/M interface moves in the opposite direction as martensite transforms back to austenite. After the reverse transformation is completed, the dislocations formed in the martensite will be carried over into the austenite lattice (90) (191) (250), which indicates the interplay between the martensitic transformation and plastic deformation (90) (91) (191) (250). The transformation induced plasticity is in the form of dislocation pile up at the A/M interface (250) and results in residual strain accumulation (91) (250). The internal stress field induced by the dislocations may pin some of the martensite variants in place (90) (91) (191) (250). Therefore, with each load-unload cycle, a small amount of residual strain remains in the material, due to the formation of dislocations and the stabilization of locked-in martensite variants by these dislocations (91).

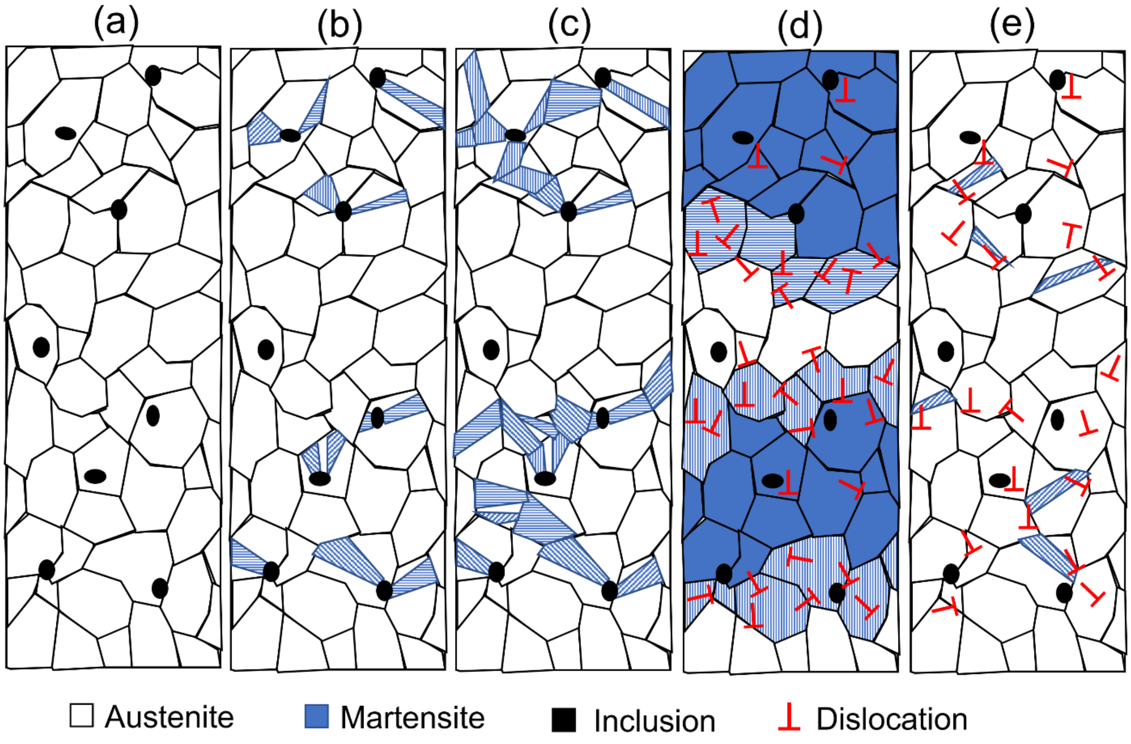

Figure 4-1- schematic of martensitic band formation in a polycrystalline material during a loading and unloading cycle.

In this chapter, a 3-D DIC system will be utilized to visualize the formation and behavior of martensite bands and gain a better understanding of the effect of wire size on material's behavior.

4.1.2 Objective and Goal

Theoretically, the deformation associated with the martensitic transformation in superelastic nitinol is fully recoverable after a complete loading cycle (196). However, it has been reported that cycling will lead to superelastic functional degradation and formation of residual martensite (239). Upon loading, the martensitic bands form and grow following the interface movement (190) (191) (251). The growth and annihilation of the deformation bands are accompanied by the formation of lattice defects to accommodate the austenite/martensite lattice misfit (167) (239). The presence of a high number of internal voids in the smaller sized wires will affect the crystallographic and micro-mechanical state around the voids and inclusions. This may result in localized martensitic transformation around the inclusion. Based on the Roark's equation (equation 2-1), stress concentration factor (K_t) around the internal sharp cracks and defects of the smaller wires is higher than the larger ones. It has been shown that the strain localization in nitinol is a competition between microstructural features and geometrical design (139). As shown in Chapter 2, the wire size impacts the accumulation and release of the latent heat of transformation, which affects the functional and structural fatigue of the wires. Therefore, when assessing the fatigue performance of the nitinol components, both microstructural and macroscopic features must be taken into consideration. I hypothesize that the microstructural and geometrical features of the specimen may affect the volume of martensitic transformation and the residual martensite. At macroscopic level, there may be some constraints that limit the M/A interface movement. In this chapter, the change in the local deformation and residual strain in a macro-scale level were analyzed, to better understand formation of the residual martensite. A 3-D DIC system was used to assess the phase transformation after a certain cyclic life, which is beneficial to analyze the functional fatigue and the residual martensite of the superelastic nitinol wires.

4.2 Experimental Procedure

The experimental procedure of DIC data acquisition was described in detail in Section 2.2. Initially, it was decided to create a neck zone on the wires and focus the DIC cameras on the neck area. However, the neck zone created a more localized effect on the superelastic behavior of the wires. The detail of DIC measurement on the sample with zone section is discussed in Appendix 4-A. Therefore, the DIC results of this chapter were collected using the as-received wires.

The DIC results indicated that the small wires were sliding in the wedge grips. Therefore, during the DIC data acquisition, the 0.2mm and 0.5mm wires were gripped using the clamp section of the bollard grips (Mark10-2.00G1103). For the 1mm wire, a pair of wedge grips (Mark10- G1061-2) were used. In this chapter, the wires used for the DIC measurement were approximately 25mm in length (distance between the grips), and the DIC cameras were focused on a random region of the wire, far from the grips, to avoid the localized effect of the grip pressure. Therefore, the strain measured by the DIC system in this chapter represents the local strain in the specific region of the wire where it was focused, and not the global strain.

X-ray diffraction (XRD) was used in this study to investigate the localized phase transformations in the wires. Initially, an XRD pattern was taken of the as-received wires at a random spot. The diffraction data were obtained using a SuperNova diffractometer, equipped with an Atlas CCD detector. The sample was positioned parallel to the face of the detector with a distance of 75 mm, and an effective angle of 90°. Scans were conducted at a scan rate of 1 deg/sec, encompassing both positive and negative 2θ angles. Cu K-alpha radiation with a wavelength of 1.54184 Å was used as the source of X-ray radiation.

The samples were fatigued for 1000 cycles under displacement-controlled condition. The upper and lower strain for each sample were set at the end-point of the wire's upper plateau and below its lower plateau, respectively. After fatigue, XRD was used to analyze the areas that showed different macroscopic transformation behavior during cycling.

4.3 Results

4.3.1 DIC Measurement of the As-Received 1mm Wire

Figure 4-2 (a) shows the first cycle of a 1mm as-received wire, fatigued under displacement-controlled condition with the frequency of 0.1Hz. The upper and lower displacements were set at the end-point of the 1mm wire upper plateau and below its lower plateau, respectively. The Figure 4-2 (b) displays the detailed progressions of the actual strain field distribution along length of the wire at points 0-9. Frame 0 shows the initial state of the as received wire. Figure 4-2 (b) indicates that the first martensite band of this region nucleated at the point 1. A drop in load was observed as the martensite band initiated in this region. The martensite band grew in both directions as the applied load increased. However, at the maximum point of the cycle (point 4), an area at the bottom of the wire did not reveal the macroscopic transformation and the A/M interface stopped there. Six areas of the 1mm wire were selected as exhibited in Figure 4-2 (b). Figure 4-2 (c) shows the mean strain versus time of these areas. Point “p” in Figure 4-2 (c) indicates where the superelastic plateau started (near 1.4% strain) and point 1 displayed nucleation of the 1st martensite band. As illustrated in Figure 4-2 (d), before point “p” a linear mean strain was observed in all areas with a small difference in their values. Figure 4-2 (e) shows small strain fluctuations in the local strain of all selected areas as the plateau starts. In Figure 4-2 (e), it can be seen that there was a sudden decrease at approximately 4.75 seconds in area “B”, followed by a rise in its strain levels. At the maximum point (point 4), areas “A”, “B”, “C” and “D” exhibited roughly 7.5% strain, while area “E” near the A/M interface showed slightly lower strain. The strain at area “F” did not exceed 2%.

Upon unloading, near point 5, martensite transforms back to austenite. At point 6, another austenite band at the top of the wire grew into the martensite. The austenite bands coalesced, and the last trace of macroscopic martensite band disappeared at point 8. However, as Figure 4-2 (f) shows, after point 8, the local strain slightly fluctuates until point e, after which a linear strain is observed.

Figure 4-3 illustrates a comparison of the local behavior of the selected areas shown in Figure 4-2 (b). The “Eng stress” was calculated as the applied load over the initial cross section area of the wire ($\sigma = \frac{F}{A}$). The “Mean strain” was calculated as the average of all point within the selected areas. Area “F” did not show a hysteresis plateau, with the strain remaining below 2%. However, the other areas displayed a stress plateau with approximately 7% of strain.

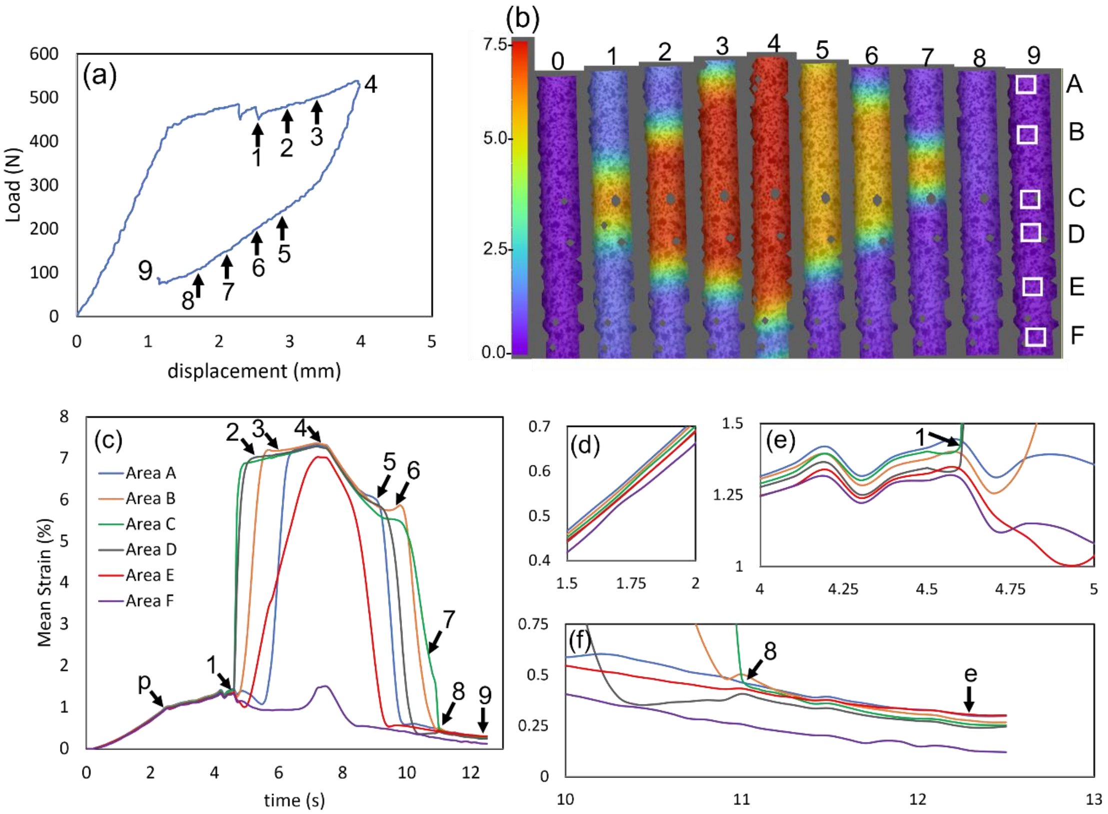

Figure 4-2- (a) The 1st cycle of the 1mm wire (b) progression of the strain distribution along the length of wire at the points 0-9 (c) mean strain versus time of the selected areas of the 1st cycle (d) enlargement of the linear section and (e) enlargement of the non-linear section (f) enlargement of end of the cycle.

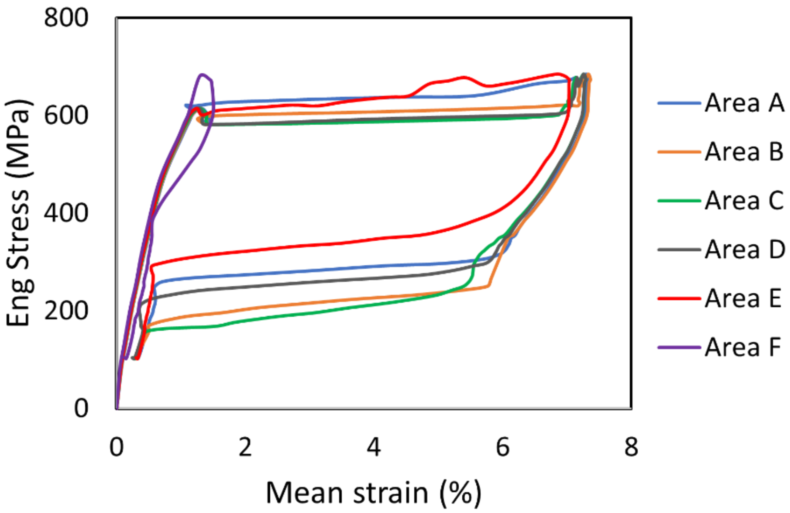

Figure 4-3- The stress-strain curves of the selected areas of cycle 1.

Figure 4-4 shows the load-displacement curve and strain distribution of the 2nd cycle. The plateau strain (point “p”) started near 1.3%. However, no martensite band initiates in this region of the wire during the 2nd cycle. Two martensite bands formed outside the focus area and expanded into the region from top and bottom of the wire. At the maximum point of the cycle (frame 3), both A/M interfaces stopped near the middle of the region, which is close to the location where the 1st band of the first cycle nucleated. Upon unloading, the martensite transformed back to austenite and the original state of the wire was recovered at the end of the cycle.

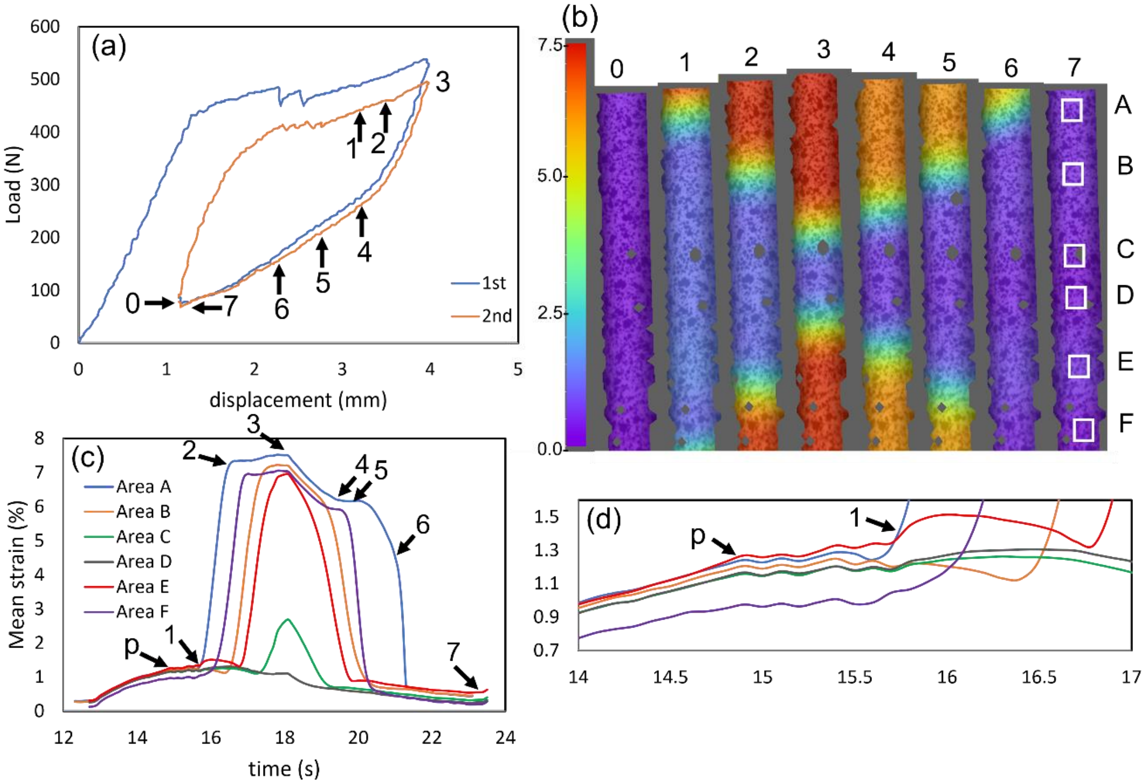

Figure 4-4- (a) The 2nd cycle of the 1mm wire (b) progression of the strain distribution along the length of wire at the points 0-7 (c) mean strain versus time of the selected areas of the 2nd cycle (d) enlarged section of 0.7-1.5% strain.

Figure 4-5 displays the load-displacement curve and strain distribution of the 3rd cycle. As shown in frame 1, a martensite band nucleated near area “E”. At frame 2, another martensite band grew into the region of interest. In frame 3, there is a region between area “B” and “C” where both A/M interfaces stopped. The comparison of the maximum points of the 2nd and 3rd cycle exhibits that the untransformed area slightly shifted up after the 3rd cycle and the A/M band stopped near area “D”. Figure 4-5 (c) displays the mean strain versus time of the selected areas. Figure 4-5 (d) shows enlargement of a section of 0.5-2% of strain.

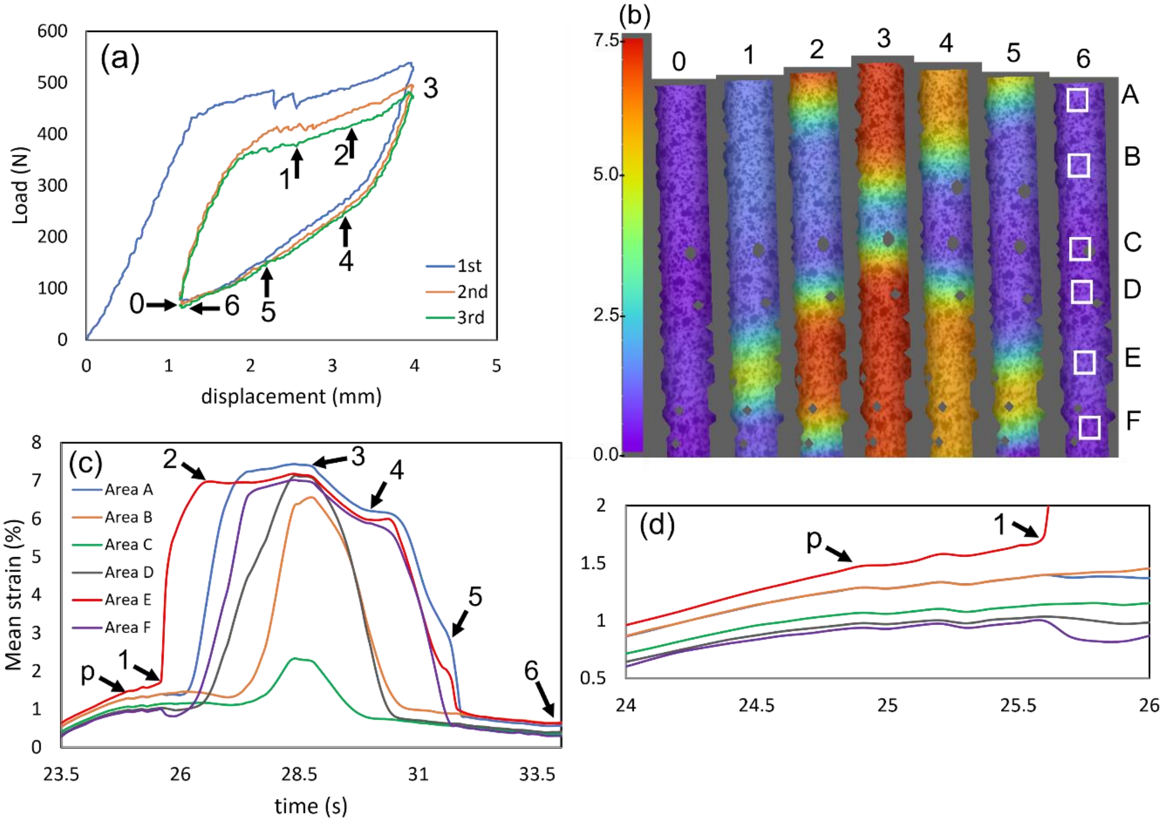

Figure 4-5- (a) The 3rd cycle of the 1mm wire (b) progression of the strain distribution along the length of wire at the points 0-6 (c) mean strain versus time of the selected areas of the 3rd cycle (d) enlargement of 0.5-2% strain.

The macroscopic band formation and annihilation of the 4th cycle is similar to the 3rd one. However, as Figure 4-6 shows, the 5th cycle has a different band structure. Two martensite bands nucleate within the region of interest at the 5th loading cycle. Both bands stopped as they reached the non-transforming region (the area that did not transform in the previous cycles). Upon unloading, both bands disappeared, and the austenite phase was recovered. Figure 4-6 (c) depicts the mean strain versus time of the selected areas. Figure 4-6 (d) shows enlargement of 0.5-2.5% of strain.

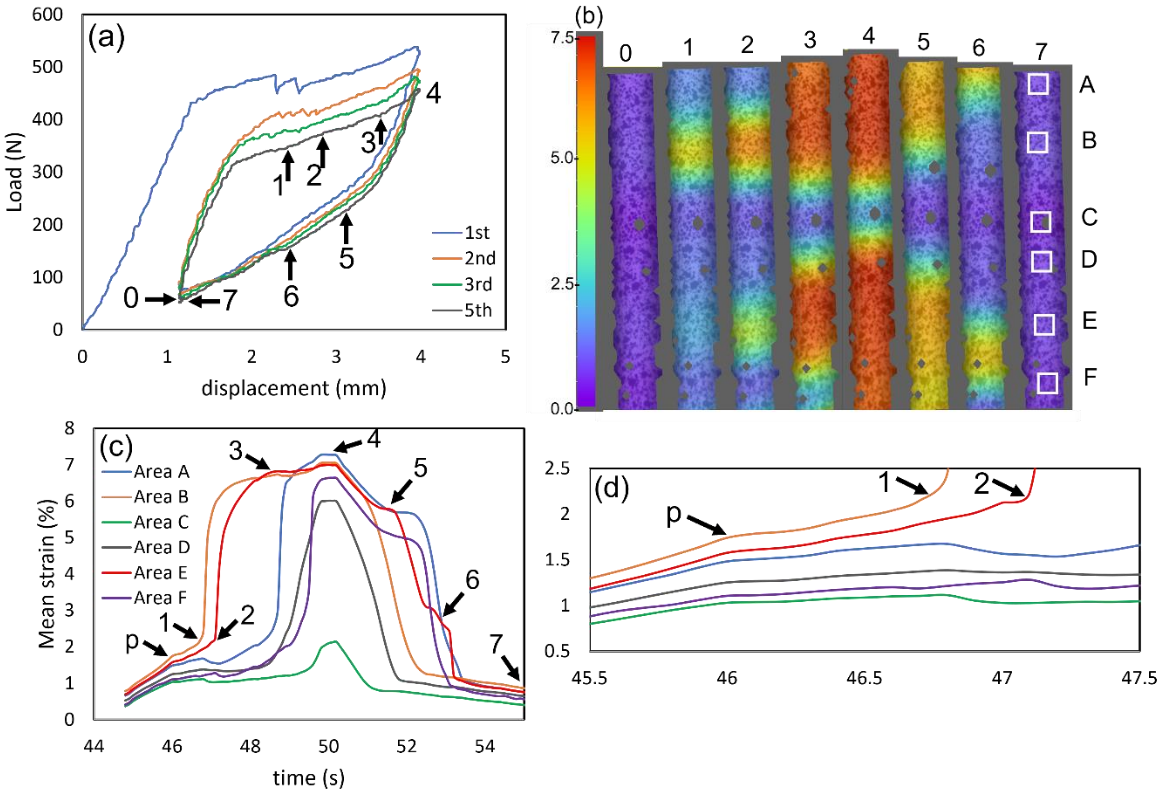

Figure 4-6- (a) The 5th cycle of the 1mm wire (b) progression of the strain distribution along the length of wire at the points 0-7 (c) mean strain versus time of the selected areas of the 5th cycle (d) enlargement of 0.5-2.5% strain.

The cycles 6-9 showed a macroscopic band structure similar to the 5th cycle. Figure 4-7 illustrates the nucleation of two martensite bands near "B" and "E". Frame 3 indicates that a martensite band expanded into the bottom side of the wire and the bands merged at area "F". As displayed in frame 8, an austenite band formed at area "F", where the two martensite bands merged during the loading cycle. As depicted in frame 9, the austenite bands merged at area "E". Figure 4-7 (c) shows the mean strain versus time of the selected areas. Figure 4-7 (d) shows enlargement of 0.5-3.5% of strain.

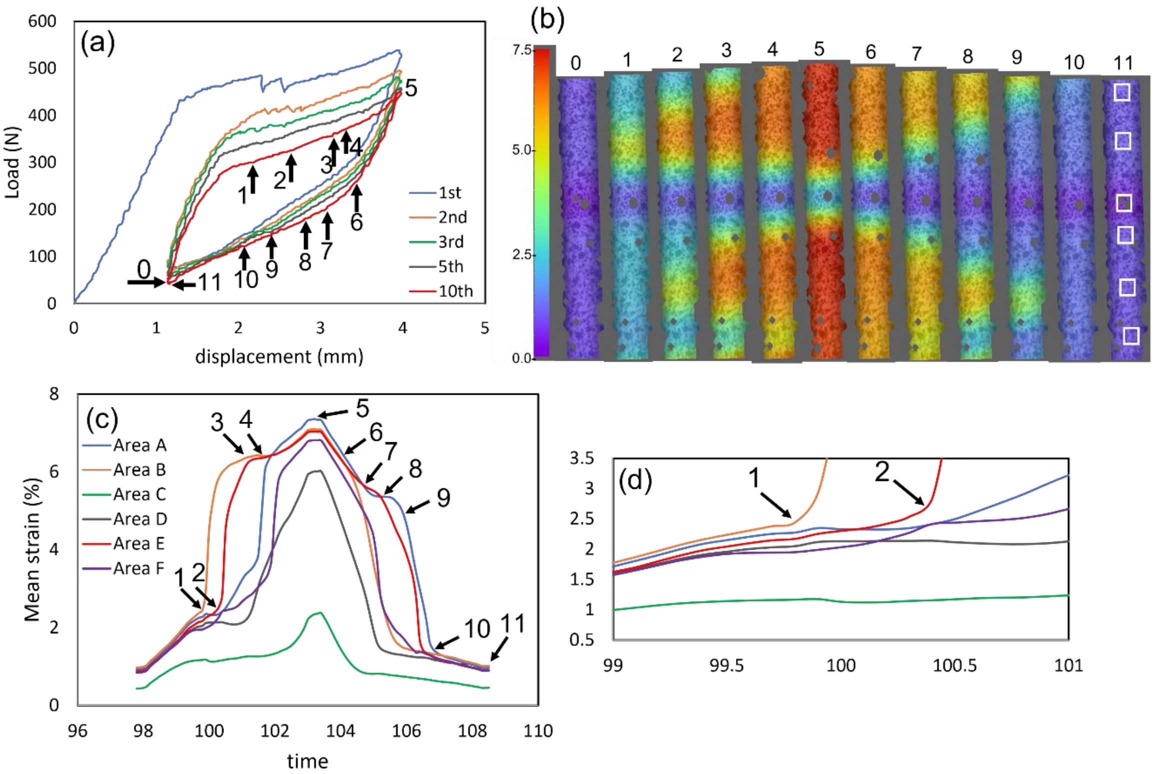

Figure 4-7-(a) The 10th cycle of the 1mm wire (b) progression of the strain distribution along the length of wire at the points 0-11 (c) mean strain versus time of the selected areas of the 10th cycle (d) enlargement of 0.5-3.5% strain.

DIC data acquisition stopped after the 10th cycle. Figure 4-8 (a) shows the last frame of cycles 1-10. Figure 4-8 (b) exhibits the evolution of residual strain of the selected areas at the end of each cycle. At the end of the 1st cycle, area “E” (where the A/M interface stopped) and area “F” (the non-transforming region) had the highest and lowest residual strain, respectively. In the 2nd cycle, the non-transforming region was near area “C”, and the residual strain of the area “F” started to increase. The highest residual strain at the end of the 2nd cycle was near areas “B” and “E”, where the A/M bands stopped. A rising trend was seen in all areas as cycle number increased. After initial cycles, the accumulation of residual strain in all areas was stabilized. At the end of the 10th cycle, area “C” showed the least accumulation of residual strain, while the residual strain in the other areas approached 0.9%.

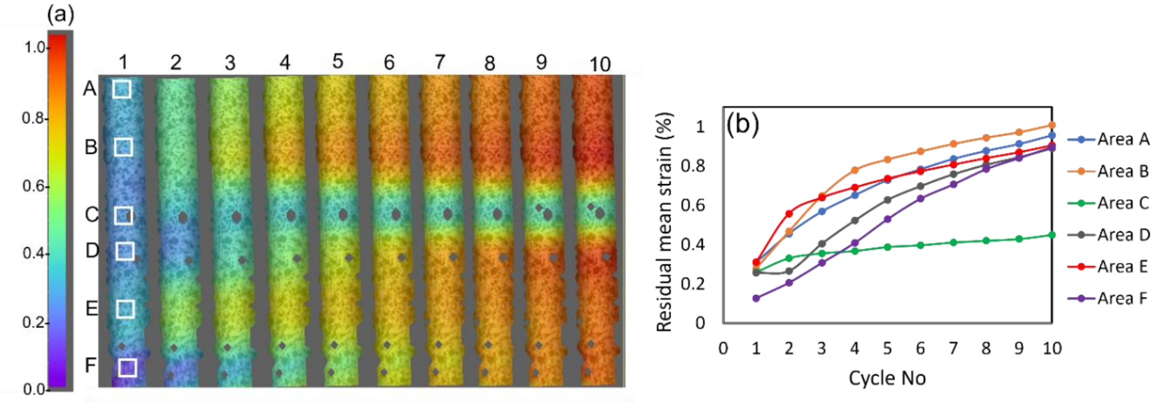

Figure 4-8- (a) The last frames of the cycles 1-10 and 6 selected areas, 1mm wire (b) the residual mean strain of each area at the end of the cycles 1-10.

The DIC image acquisition was started over again at the 30th cycle. Figure 4-9 shows the progression of the strain distribution in Cycle 30. Frame 1 shows that at Cycle

30, 4 martensite bands nucleated at relatively close times. The bands expanded and gradually coalesced at point 3 and saturated at the maximum point (point 4). The A/M interface stopped near area “C” and the strain at area “C” did not exceed 2%. Upon unloading, the austenite band expanded, and the initial state of the wire was recovered. Figure 4-9 (c) shows the mean strain versus time of the selected areas. Points “p” and 1 displays the onset of plateau and the martensite bands nucleation, respectively. Figure 4-9 (d) illustrates enlargement of 0.5-3% strain. Tracing the mean strain vs time curve of area “C” shows that its elastic section gradually dropped below other regions as well.

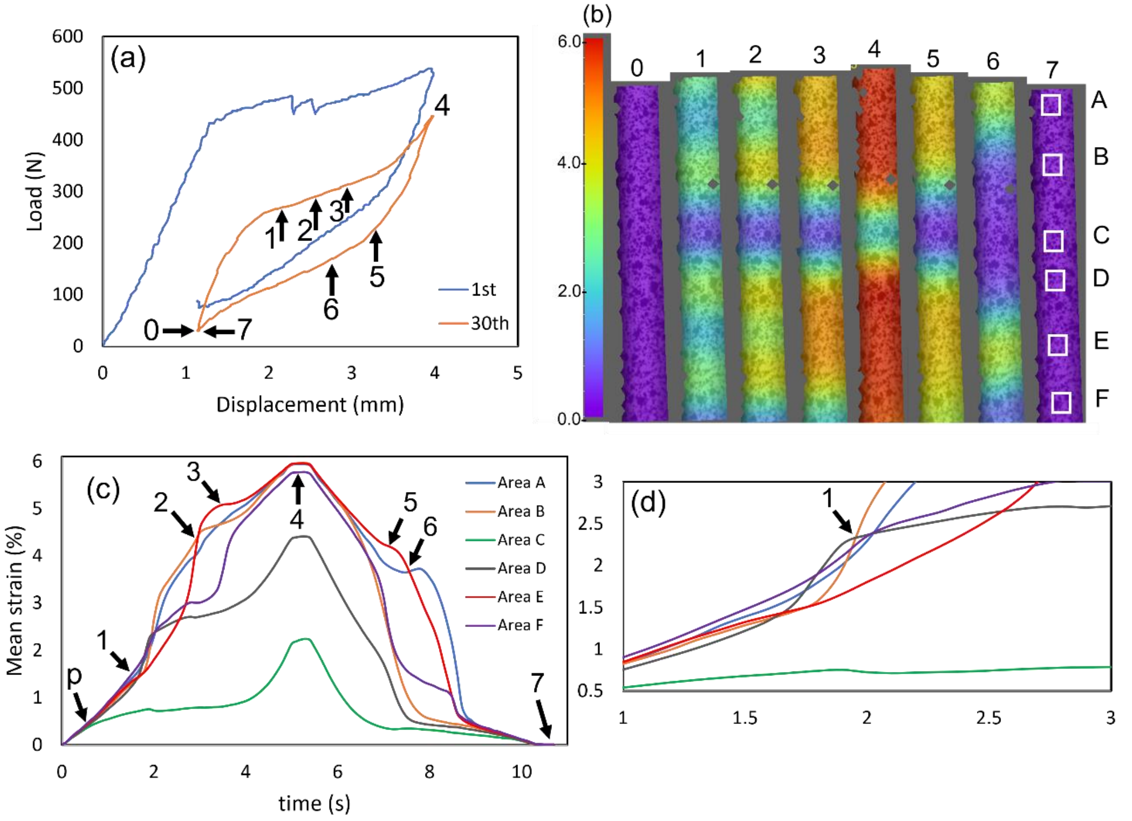

Figure 4-9- (a) The 30th cycle of the 1mm wire (b) progression of the strain distribution along the length of wire at the points 0-7 (c) mean strain versus time of the selected areas of the 30th cycle (d) enlargement of 0.5-3% strain.

The DIC data of the cycles 100, 500 and 1000 showed the same macroscopic band structure as the 30th cycle, where 4 martensite bands nucleated upon loading and a region in around area “C” remained untransformed.

Figure 4-10 shows the residual strain of the cycles 30, 100 and 500. Each frame displays the residual strain of one cycle. The residual strain map of the 30th and 100th cycles revealed a pattern similar to Figure 4-8, where the strain near area “C” was significantly less than the other regions. However, the Figure 4-10 (c) shows that the residual strain of Cycle 500 did not follow the martensite band formation and annihilation pattern anymore.

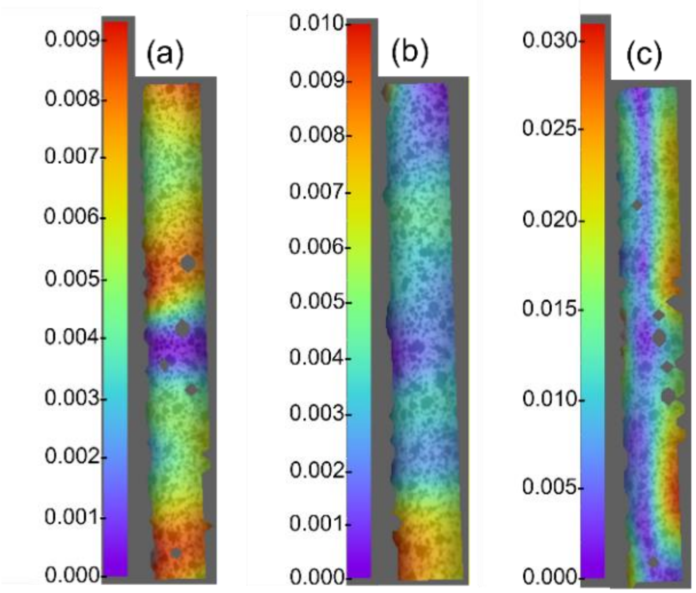

Figure 4-10- residual strain of the cycles, 1mm wire (%) (a) 30, (b) 100 and (c) 500.

4.3.2 DIC Measurement of the As-Received 0.5mm Wire

Figure 4-11 (a) shows the first cycle of a 0.5mm as-received wire, fatigued under displacement-controlled condition with the frequency of 0.1Hz. The upper and lower strains were set at the endpoint of the 0.5mm wire upper plateau and below its lower plateau, respectively. Figure 4-11 (b) displays the actual strain field distribution along length of the wire at the points 0-9. To study the localized residual strain of the wire, 5 areas of the sample were selected. Figure 4-11 (c) shows the mean strain versus time of the areas for the 1st cycle. Points "p" and 1 depict the onset of superelastic plateau and the moment that a martensite band grew into the region of interest, respectively. No martensite band nucleated at the region of interest during the first loading cycle. A band grew into the region from the upper side of the wire. As shown in Figure 4-11 (d), right before the band reaching areas "A", there was a sudden drop in its local strain. The same pattern happened when the martensite band reached area "B" at 4 seconds. At the peak of the cycle, a small area at the bottom of the region did not show macroscopic phase transformation and the A/M interface stopped near area "E". Upon unloading, the reverse transformation occurred, and martensite disappeared after point 7. However, the strain curves revealed small fluctuations until point e.

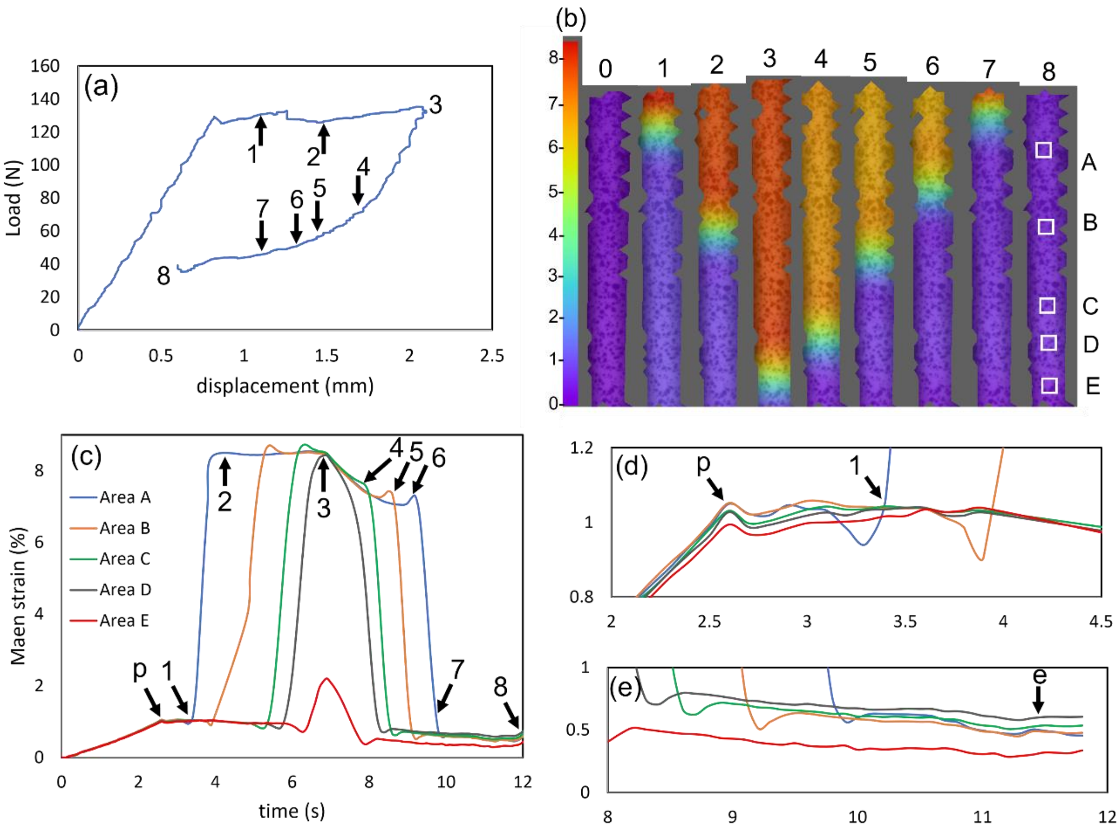

Figure 4-11- (a) The 1st cycle of the 0.5mm wire (b) progression of the strain distribution along the length of wire at the points 0-8 (c) mean strain versus time of the selected areas (d) enlargement of 0.6-1.2% strain (e) enlargement of end of the cycle.

The 2nd cycle showed the same band structure as the 1st one. Figure 4-12 depicts that the 3rd cycle has a different band pattern. A martensite band nucleated at the stress point indicated as 1. Upon growth, it coalesced to another band that grew into the region of interest. The A/M interface stopped as it reached the area "E." Upon unloading, the martensite band gradually disappeared. Figure 4-12 (c) and (d) show that within the elastic region (before point "p"), the strain in area "E" was significantly lower than the other areas. At the peak of the cycle, the strain at area "D" reached 8.7%, while the area "E" did not exceed 4%.

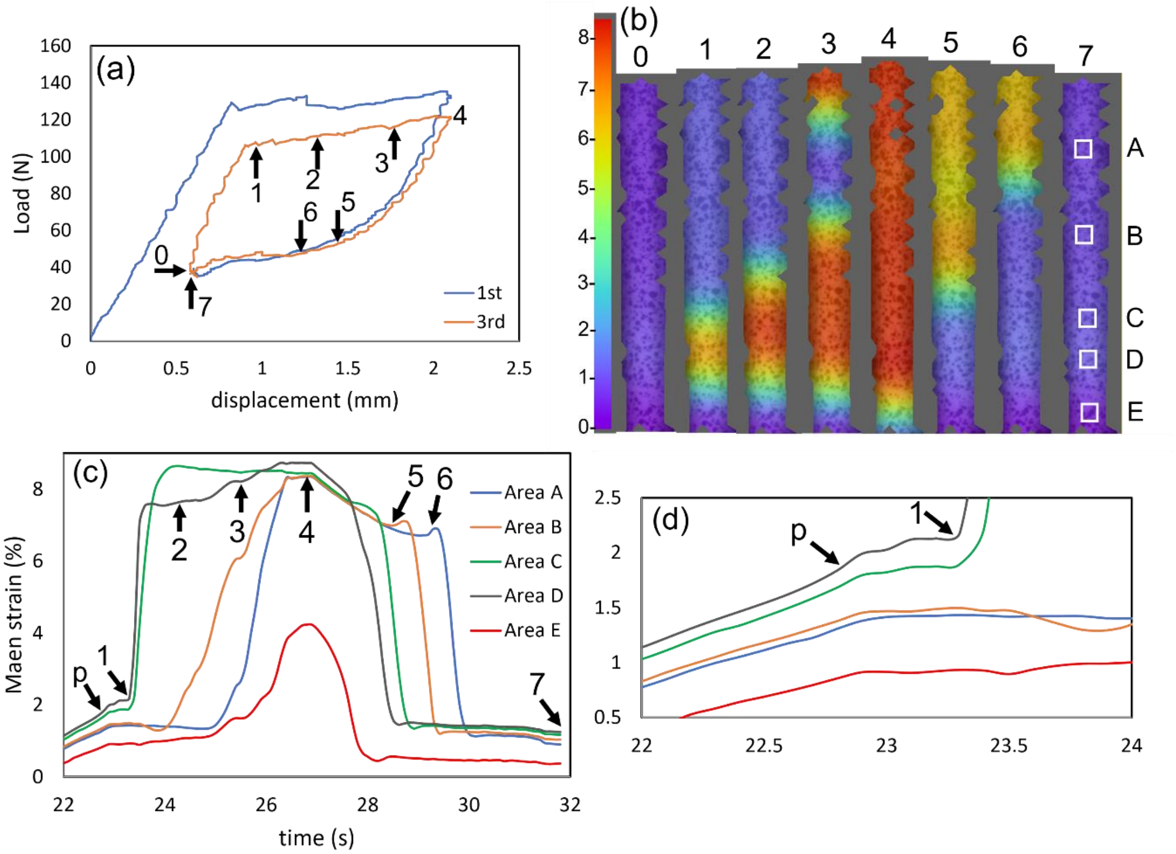

Figure 4-12- (a) The 3rd cycle of the 0.5mm wire (b) progression of the strain distribution along the length of wire at the points 0-7 (c) mean strain versus time of the selected areas (d) enlargement of 0.5-2.5 strain.

The 4th cycle revealed a similar band structure to the 3rd one. Figure 4-13 shows the progression of the strain distribution along the wire at the 5th cycle. During this cycle, the band formation pattern on loading remained unchanged. However, the band annihilation pattern at the reverse transformation (unloading) changed. At frame 6, an austenite band nucleated within the martensite region at area “A”. Figure 4-13 (c) showed that when the two austenite bands reached near area “B”, its local strain suddenly increased prior to coalescence of the austenite bands (point 7). Figure 4-13 (d) shows enlargement of 0.5-3.5% strain. As displayed in Figure 4-13 (b) the austenite bands coalesced near area “B”.

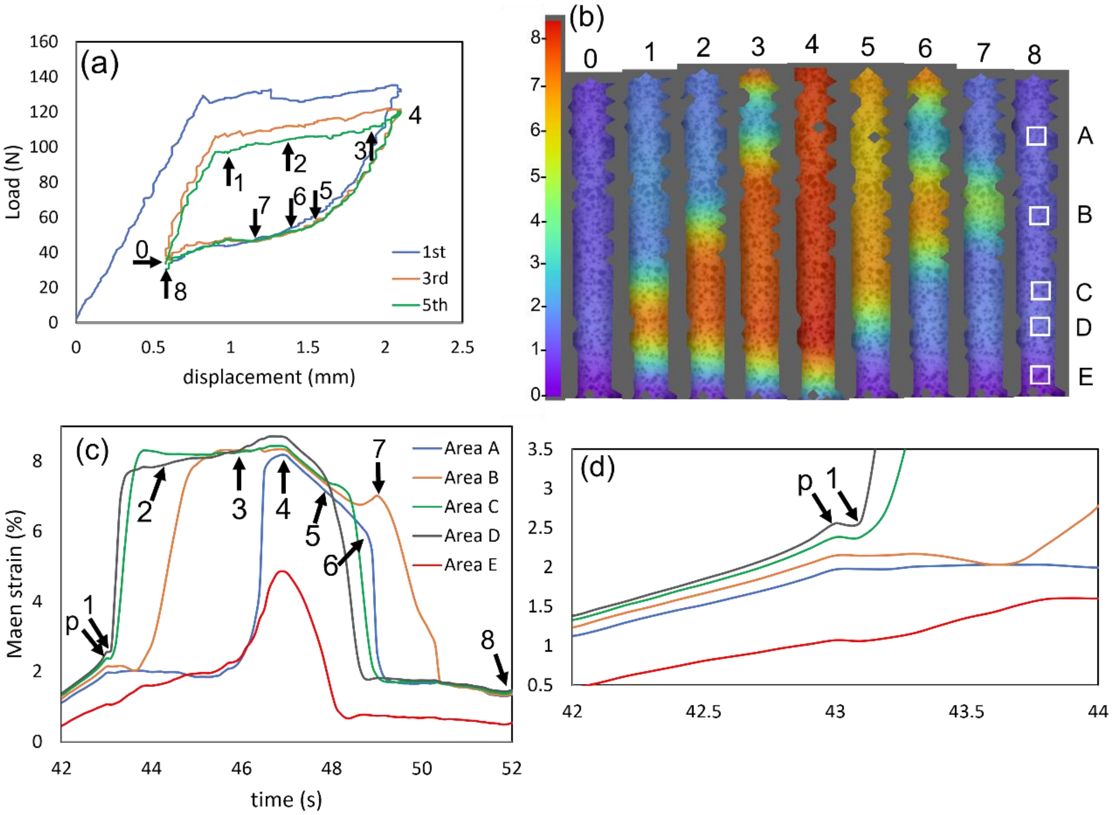

Figure 4-13- (a) The 5th cycle of the 0.5mm wire (b) progression of the strain distribution along the length of wire at the points 0-8 (c) mean strain versus time of the selected areas of the 5th cycle (d) enlargement of 0.5-3.5% strain.

The 6th and 7th cycle displayed the same martensitic band structure. Figure 4-14 shows that the band structure changed again at the 8th cycle. Frame 2 of Figure 4-14 (b) revealed two martensite bands nucleated at the region of interest at point 1 and 2, respectively. Figure 4-14 (c) shows the mean strain versus time of the selected areas for the 8th cycle. The A/M band stopped near area “E” and its strain remained at about 2%. Toward the end of the loading cycle, the strain in this area increased to 4%. Figure 4-14

(d) displays enlargement of 1-4% strain. As exhibited in Figure 4-14 (b) the band pattern on unloading was similar to the 5th cycle.

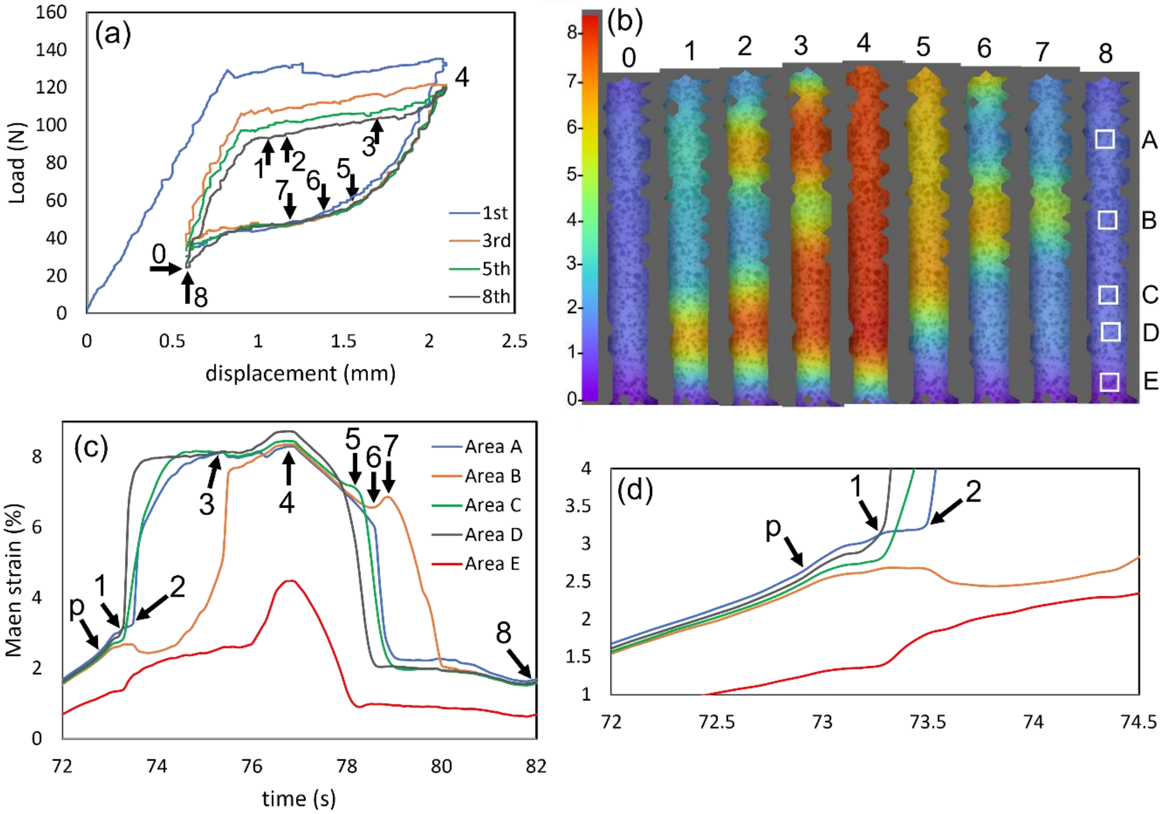

Figure 4-14- (a) The 8th cycle of the 0.5mm wire (b) progression of the strain distribution along the length of wire at the points 0-8 (c) mean strain versus time of the selected areas (d) enlargement of 1-4% strain.

The formation and annihilation of the austenite and martensite bands did not change in the subsequent cycles. Figure 4-15 (a) and (b) show the last frame of cycles 1-10 and the evolution of residual strain of the selected areas at the end of each cycle, respectively. At the end of the 1st cycle, the untransformed area “E” and the area that the A/M interface stopped (area “D”) had the lowest and highest residual strain, respectively. As the cycle number increased, all areas showed an increasing trend. Area “E” remained the area with the least strain, while the residual strain at area “A” increased at a faster rate. After 7 cycles, the accumulation of residual strain in all areas was stabilized.

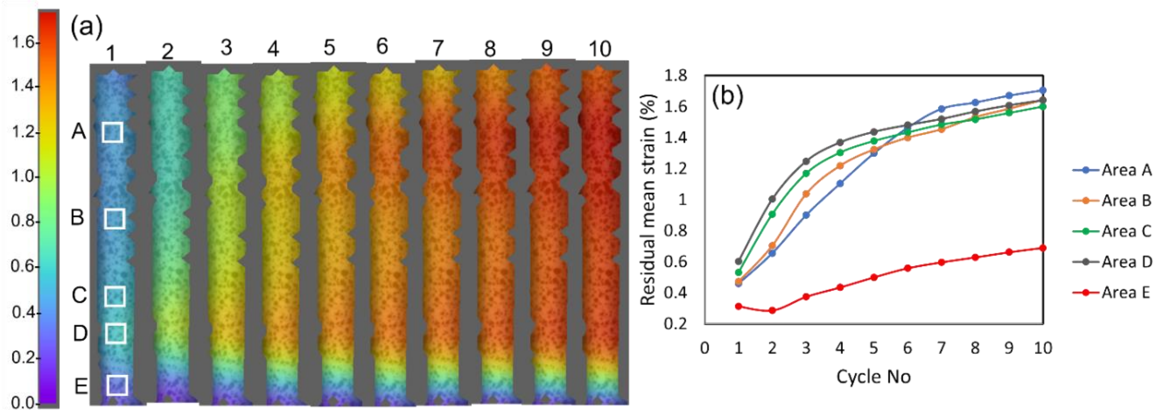

Figure 4-15- (a) The last frames of the cycles 1-10 and 5 selected areas, 0.5mm wire (b) the residual mean strain of each area at the end of the cycles 1-10.

Figure 4-16 shows the 30th cycle of the 0.5mm wire along with its DIC results. As frame 1 displayed, two martensite bands nucleated upon loading, similar to the 8th cycle. However, comparing the frame 2 of Figure 4-14 (b) and frame 1 of Figure 4-16 shows that the upper martensite band slightly shifted down. The unloading pattern did not change. Figure 4-16 (c) exhibited the change in mean strain versus time of the selected areas. Figure 4-16 (d) illustrates enlargement of 1-4% strain.

The formation and annihilation of the bands remained unchanged at cycles 100 and 500. Figure 4-17 shows the residual strain of the cycles 30, 100 and 500. The highest residual strain was observed near area "A" in the residual strain maps of the 30th and 100th cycles. Area “B” and “D” displayed high local residual strain as well. The localized strain accumulation at the end of the 100th cycle is more distinct compared to the 30th cycle.

Figure 4-17 (c) shows that at the end of the cycle 500, the residual strain did not have a band pattern anymore.

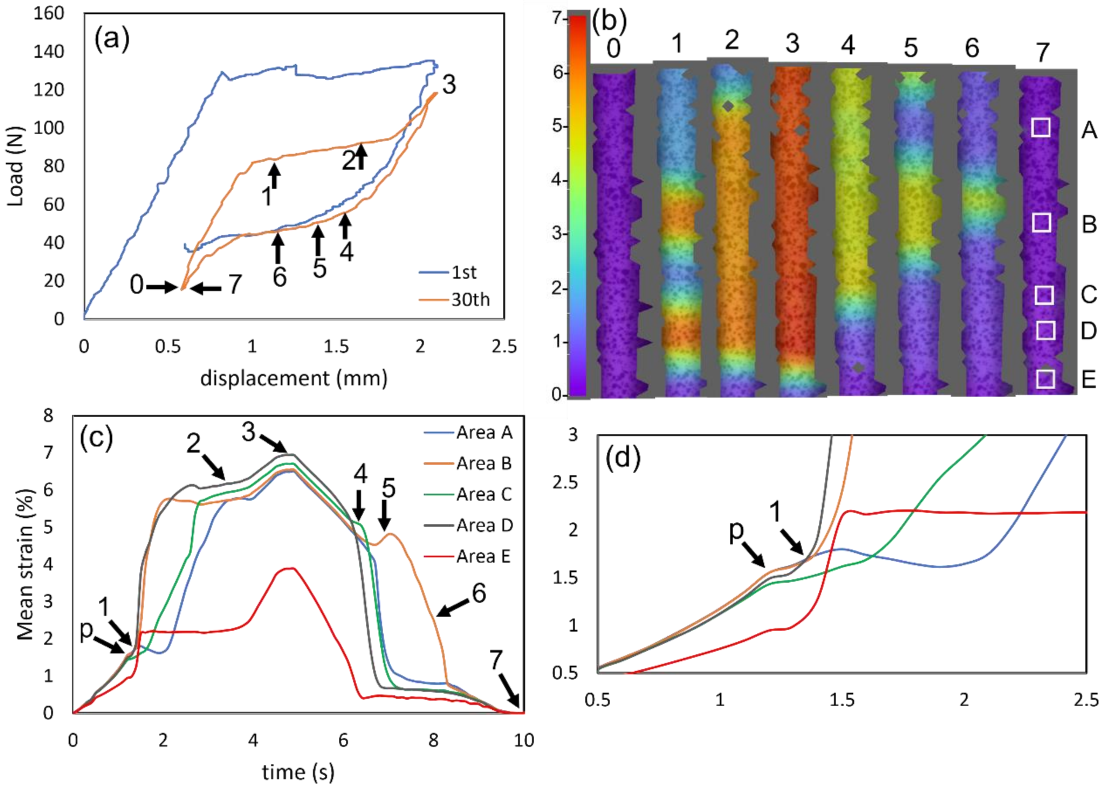

Figure 4-16- (a) The 30th cycle of the 0.5mm wire (b) progression of the strain distribution along the length of wire at the points 0-7 (c) mean strain versus time of the selected areas of the 30th cycle (d) enlargement of 0.5-3% strain.

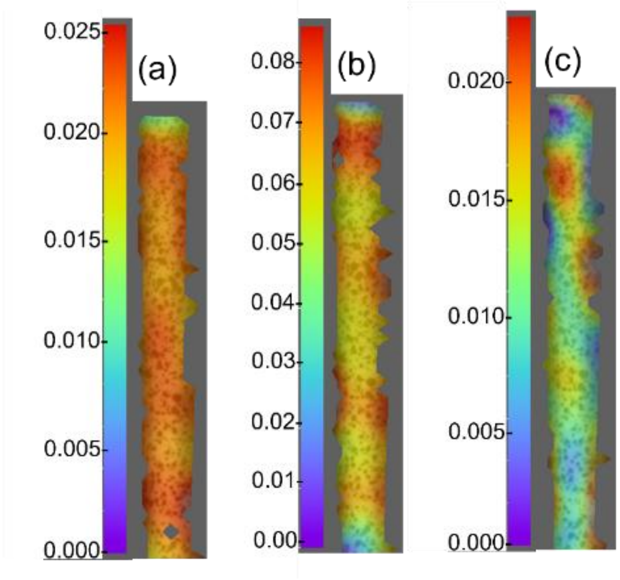

Figure 4-17-residual strain of the cycles, 0.5mm wire (%) (a) 30, (b) 100 and (c) 500, 0.5mm wire.

4.3.3 DIC Measurement of the As-Received 0.2mm Wire

Figure 4-18 shows the 1st cycle and the strain distribution of the 0.2mm wire. The upper and lower strains were set at the endpoint of the 0.2mm wire upper plateau and below its lower plateau, respectively. To examine the localized strain distribution of the wire, 4 random areas were selected, as illustrated in Figure 4-18 (b). The DIC map revealed that no martensite band nucleated at this region at the 1st cycle. As shown in Figure 4-18 (c), The plateau starts at point “p”, followed with small strain fluctuations in all selected areas. At point 2, a martensite band grew into the region. At 3 seconds, just before the A/M interface reached area "A," a drop in its local strain occurred. A similar pattern was observed in other areas as the martensite band approached them. At the peak (point 4), the area of interest was all in the martensitic state. Upon unloading, an austenite band nucleated at area “A” at point 7. Toward the end of cycle, another austenite band grew into the region of interest from the bottom side of wire (see frame 10). As the austenite bands approached each other near area "D," an increase in its local strain was observed, as depicted in Figure 4-18 (c). This was followed by the coalescence of the austenite bands and a decrease in local strain. After the martensite band disappeared, the strain of area "D" dropped to point "e". Note that after point e, all areas showed a linear behavior. At the end of the cycle (frame 11), the austenite was fully recovered.

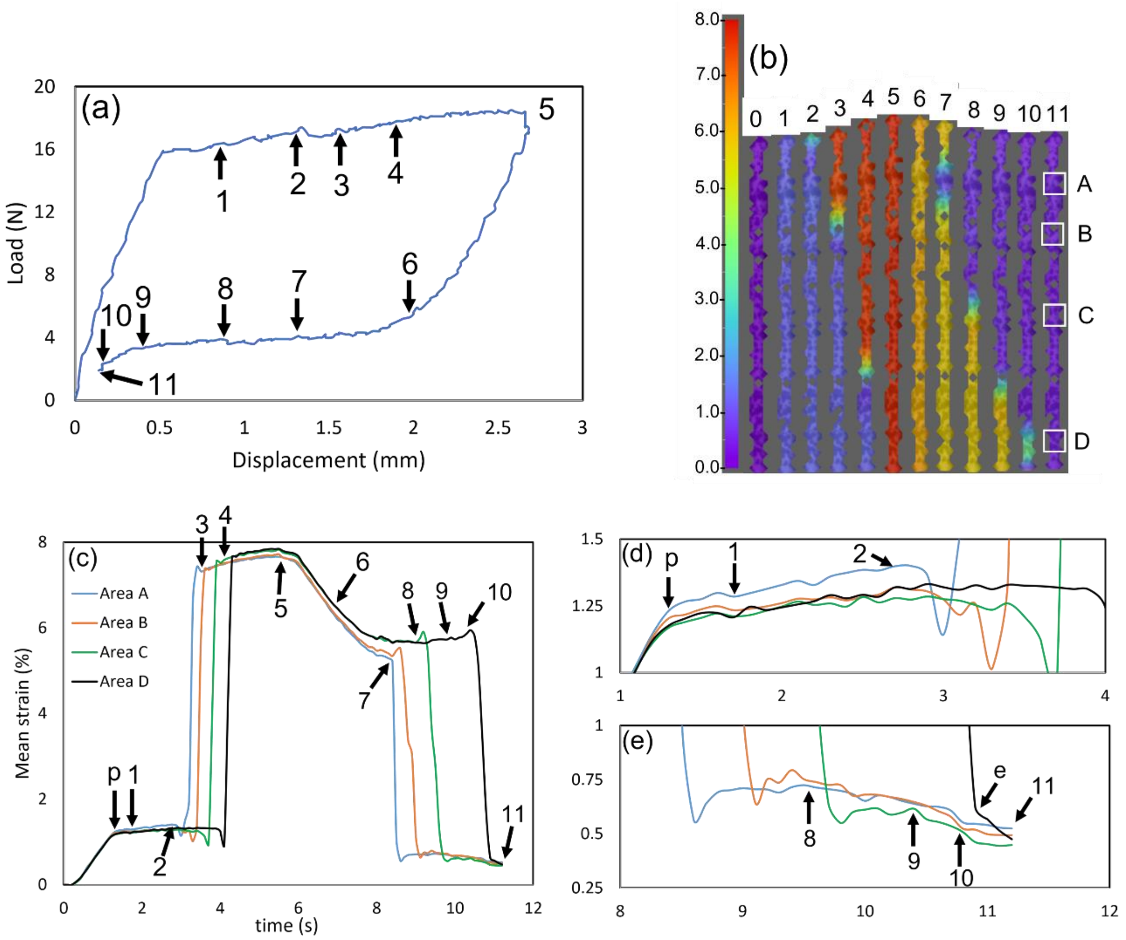

Figure 4-18- (a) The 1st cycle of the 0.2mm wire (b) progression of the strain distribution along the length of wire at the points 0-11 (c) mean strain vs time of the selected areas (d) enlargement of 1-1.5% strain, beginning of loading (e) enlargement of 0.25-1% strain, end of unloading.

Figure 4-19 shows the 2nd cycle and the strain distribution of the 0.2mm wire. Upon loading a martensite band nucleated at area “A”, the same location that the austenite band formed in the previous cycle. The martensite band grew throughout the region of interest in two directions. At the maximum point (point 4), the area of interest was fully in the martensitic state. Upon unloading, an austenite band nucleated around area “A” and grew in both directions. Figure 4-19 (c) displays mean strain versus time of the selected areas. Figure 4-19 (d) shows enlargement of 1-2% strain.

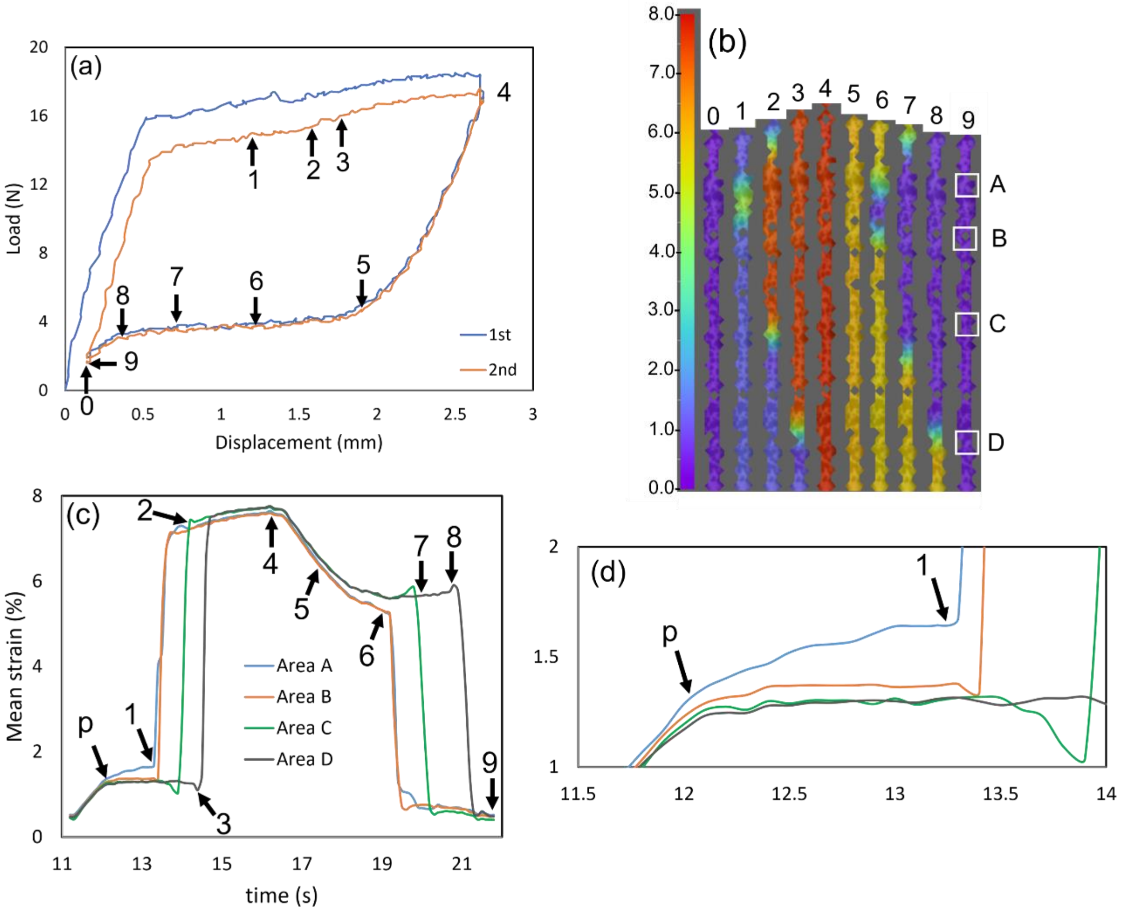

Figure 4-19- (a) The 2nd cycle of the 0.2mm wire (b) progression of the strain distribution along the length of wire at the points 0-9 (c) mean strain vs time of the selected areas (d) enlargement of 1-1.5% strain.

Figure 4-20 shows the 3rd cycle and the strain distribution of the 0.2mm wire. As exhibited in Figure 4-20, upon loading a martensite band formed at area “A”, similar to the 2nd cycle. After unloading, no austenite band nucleated in the area. Instead, two austenite bands grew into the region from upper and bottom sides of the wire. The martensite disappeared at area “D”, similar to the 1st cycle. Figure 4-20 (c) shows mean strain versus time of the selected areas. Figure 4-20 (d) displays enlargement of 0.25-1.25% strain.

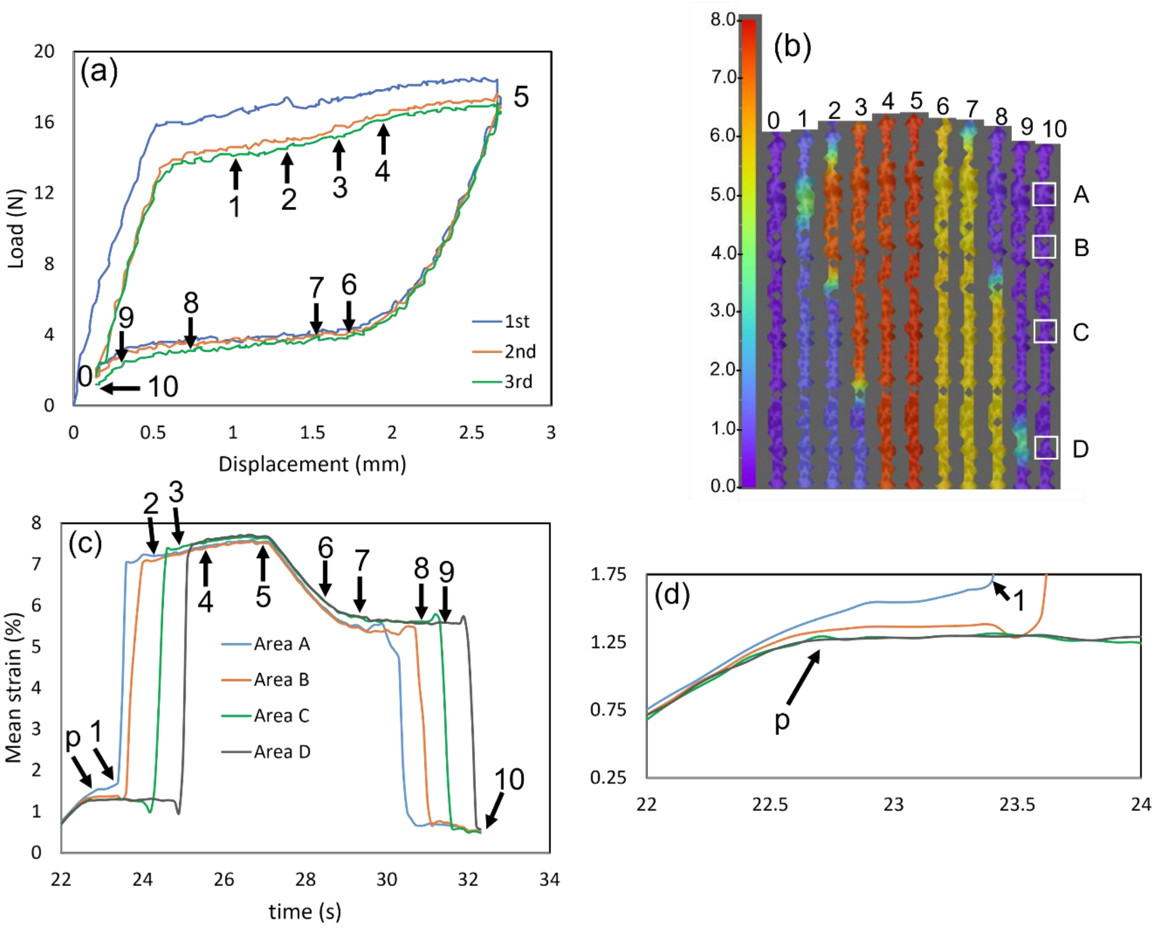

Figure 4-20- (a) The 3rd cycle of the 0.2mm wire (b) progression of the strain distribution along the length of wire at the points 0-10 (c) mean strain vs time of the selected areas (d) enlargement of 0.25-1.75% strain.

The subsequent cycles showed the same band formation and annihilation as the 3rd cycle. Figure 4-21 illustrates the last frames of the first 10 cycles of the 0.2mm wire. it can be seen from Figure 4-21 (a) that the residual strain mainly accumulated near areas “A” and “D”. Figure 4-21 (b) shows small fluctuation in residual strain of the areas in the first 5 cycles. Following the 5th cycle, stability was achieved.

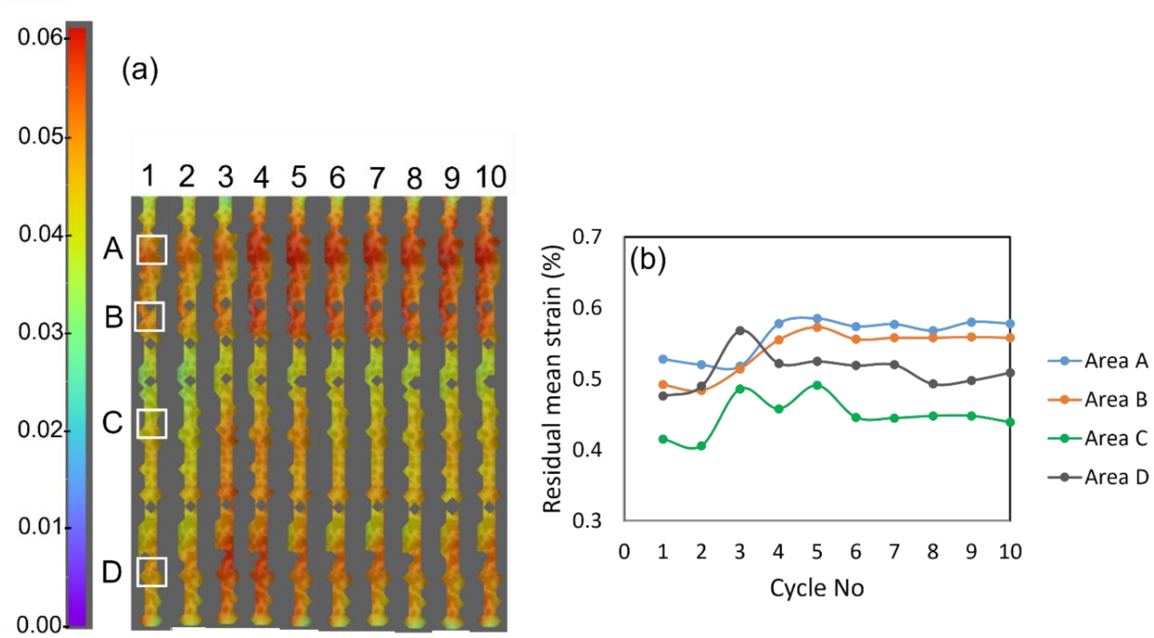

Figure 4-21-(a) The last frames of the cycles 1-10 and 4 selected areas (b) the residual mean strain of each area at the end of the cycles 1-10.

The 30th, 100th and 500th cycles showed the same martensite band pattern as Cycle 4, where the martensite and austenite bands both nucleated at area “A” and the last martensite band disappeared near area “D”. However, it was not possible to generate a DIC strain map for their last frame and evaluate their residual strain. At the end of the 30th cycle, the lower stress dropped below zero. Due to the compressive stress, the wire was bent at the end of the cycles, and the reference point of the DIC camera moved out of view. So, the software was not able to generate a strain map for the last frame of the cycles. Upon next loading, the wire returned to the camera view.

To avoid compression stresses, a higher fatigue mean strain was considered. The DIC maps of the 0.2mm wire revealed that the martensite bands persisted until the end of the lower plateau. Therefore, increasing the lower limit of fatigue will result in some remaining martensite bands at the end of the cycles. Appendix 4-B shows an example of DIC map, where the lower fatigue limit was set slightly above end of the lower plateau. In order to investigate the changes of martensite band patterns in the absence of compressive stress, the stress-controlled DIC measurements were also performed for the 0.2mm wire. The results of the stress-controlled test on the 0.2mm wire are shown in Appendix 4-C.

4.3.4 X-Ray Diffraction

Figure 4-22 shows the XRD pattern of all three wires, before and after 1000 cycles. While the 1mm wire exhibited a small amount of martensite in the as-received sample, the 0.5mm and 0.2mm wires exhibited significant martensite peaks in their as-received state. As shown in Figure 4-22 (a), the 0.5mm wire also displayed some indication of R-phase in its diffraction pattern. However, the R-phase content was not significant, because the tensile behavior of the wires did not exhibit a 2-step plateau (see the tensile behavior of the wires in Figure 2-6 (a) and (b)) and the DSC curve of the 0.5mm wire did not show the R-phase peak (Figure 2-4). The diffraction pattern in Figure 4-22 (a) also revealed that the smaller wires exhibited broader peaks. The DIC maps of the 1mm and 0.5mm wires (sections 4.3.1 and 4.3.2) showed that some areas of these wires did not experience a macroscopic phase transformation. The regions that did not undergo macroscopic phase transformation are labeled as non-transforming regions. Transforming regions refer to the portions of the wire that experienced macroscopic phase transformation in each cycle. Unlike the 1mm and 0.5mm wires, the 0.2mm wire did not display any non-transforming regions. The XRD patterns were obtained from both random transforming and non-transforming regions of the wires. After 1000 cycles, the diffraction pattern of the non-transforming region displayed minor martensite peaks, as depicted in Figure 4-22 (b). The martensite peaks were more pronounced in the transforming region of the 1mm wire after cycling. In the case of the 0.5mm wire (Figure 4-22 (c)), the trend was reversed. The non-transforming region exhibited significant martensite peaks and minor peaks of austenite and R-phase. On the other hand, the transforming region displayed a strong peak of austenite and weak peaks of martensite. In the 0.2mm wire, the martensite peaks noticeably increased after cycling, while the austenite peak decreased, as shown in Figure 4-22 (d).

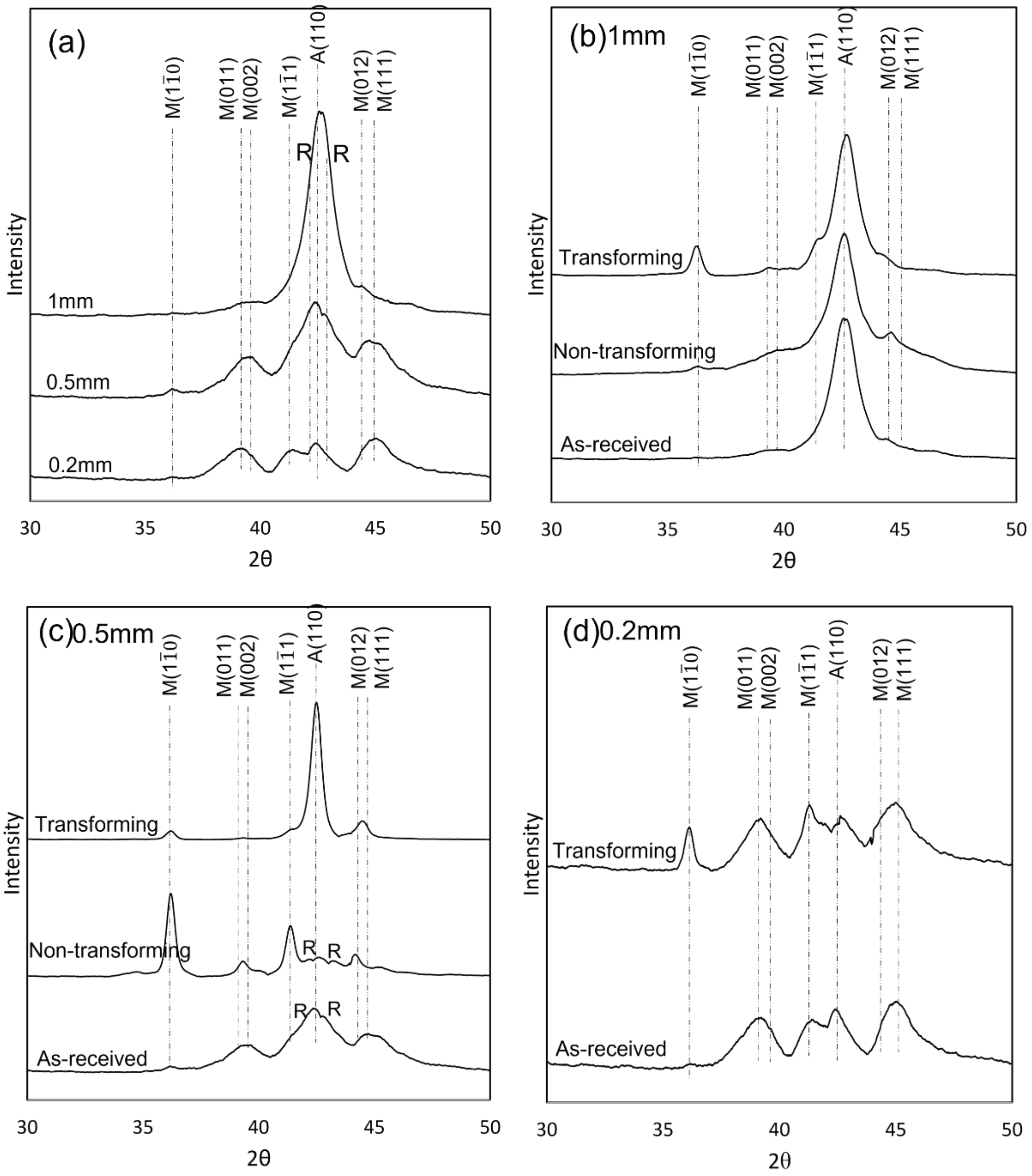

Figure 4-22- XRD patterns of (a) random spots of the as-received samples, (b) the 1mm wire after 1000 cycles, a random spot on the area that was going through phase transformation and the non-transforming region, (c) 0.5mm wire, a random spot of transforming and non-transforming region after 1000 cycles (d) 0.2mm wire, a random spot of the sample after 1000 cycles.

4.4 Discussion

As shown in Figure 4-22 (a), the XRD analysis of the as-received samples revealed that there was an increase in peak broadening as the wire size decreased. It has been shown that the presence of internal defects in metals, resulting from processing, can lead to peak broadening in XRD analysis (111) (112) (252). Additionally, microstructural changes, such as grain refinement and texture development introduced through wire drawing, can contribute to the observed peak broadening in the XRD pattern (111) (112) (252).

The mean strain-time configuration of all three wires showed linear behavior before point “p” (onset of plateau) which is associated to elastic deformation of austenite phase. After point “p” and prior to development of the first martensite bands, small fluctuations were observed, implying that the transformation started at the grain size level. This is consistent with the observation of Daly et al (139) that the phase transformation has started before the macro-bands are seen. Daly et al (139) reported that these small fluctuations in the local strain ultimately led to formation of the localized macro martensite bands. As shown in Figure 4-2 (e), at 4.6 seconds a sudden rise was observed in mean strain of area “C” and “D”, and as their local strain reached around 1.4%, the first macroscopic martensite band nucleated. Zheng et al (190) proposed that the band formation is an indicator of a weak zone, which likely has a higher density of microstructural defects. As exhibited in Figure 4-2 (a), formation of a local macroscopic martensite band is accompanied by a spontaneous elongation and sudden drop in the applied load (251). The other drop in load before point 1 is likely related to nucleation of another martensite band somewhere out of the view. As shown in Figure 4-2 (c), at the cycle peak (point 4), strain was not perfectly uniform throughout the wire and small fluctuations exist. The stress-strain behavior of the selected areas is depicted in Figure 4-3. The figure reveals that both stress and strain exhibit local fluctuations and are not uniformly consistent. This is consistent with the nonhomogeneous nature of nitinol. Upon unloading, the martensite phase initially recovers its elastic strain. Thus, the first portion of the strain-time and stress-strain curves exhibit an elastic behavior immediately after the peak point. The residual strain of the 1st cycle (frame 1 of Figure 4-8) shows that at the end of the cycle, area "E" has the highest residual strain (about 0.3%), which is related to the stop in progression of A/M interface.

At the 2nd cycle (Figure 4-4), before the local strain of this section of the wire reached 1.3%, two martensite bands grew into the region. Considering the macroscopic band pattern of the 2nd cycle, it can be concluded that for this cycle, 1.3% strain is not enough for nucleation of a martensite band. The A/M interfaces stopped before they reached area "C" and "D". Initially, it was assumed that the applied load was not high enough to transform all areas of the wire. But the subsequent cycling showed that even after the upper plateau dropped (as a result of functional fatigue), and the applied load went beyond the plateau stress, some areas still remained untransformed. Area "E" was close to the A/M interface and its strain did not exceed 7% at its peak. Frame 2 of Figure 4-8 shows that the residual strain at area "B" and "E" is growing with a faster rate, which is due to the cessation of the A/M interface in these regions. At the peak of the 2nd cycle, area "A" experienced the highest amount of superelastic strain. Figure 4-8 (b) showed a high amount of residual strain at the end of the 2nd cycle. From these observations, it can be concluded that a higher level of martensite band saturation results in a higher level of defect accumulation in the material.

Figure 4-5 showed that at the beginning of the 3rd cycle, the local strain in area "E" remained noticeably higher than other areas. At 25.6 seconds (point 1), the local strain of area “E” reached 1.6%, while other areas remained below 1.4%. As a result, a macroscopic martensite band formed at area “E”. At this cycle, the A/M interface of the lower band reached the area “D”, causing the local strain of “D” to increase. Consequently, the defect accumulation rate in area “E” decreased (see Figure 4-8 (b), change in slope of the area “E” after the 3rd cycle). At the end of the 3rd cycle, local strain in area “B” and “E” was equal. Upon unloading, the austenite band of area “C” expanded and merged with another growing austenite band near “E”. Figure 4-8 (b) also shows that the residual strain of area “F” is increasing with a higher rate, which may be caused by annihilation of the martensite band near this area. The local behavior of the wire below the field of view might affect the local strain accumulation of area “F” as well. There is a possibility that the martensite band either stopped below area "F" or merged with another band, resulting in an increase in the residual strain of this area.

The 4th cycle showed the same band pattern structure as the 3rd one. Although area “B” and “E” had the same amount of residual strain at the end of the previous cycle, only one martensite band formed near “E”. Frame 4 of Figure 4-8 displayed that at the end of the 5th cycle, the local residual strain of “B” exceeded that of "E", which may provide enough activation energy for formation of another martensite band near this area. As depicted in Figure 4-6, during the 5th cycle, the first martensite band formed at area “B” once its local strain exceeded 2%. At point 2, the strain at area “E” reached 2% and the second martensite band formed. Figure 4-8 shows that after the 5th cycle, residual strain of the area “A” reached the residual strain of area “E”.

Figure 4-8 depicted that after the 7th cycle, the residual martensite of area “A” exceeded the one of “E”. However, the DIC results demonstrated that the band pattern of this region remained unchanged until the 9th cycle. Figure 4-7 (c) and (d) showed that once the local strain of “B” and “E” reached 2.5%, the macroscopic martensite bands nucleated at these areas. Before the local strain of area "A" reached this critical level, the band at "B" expanded into area "A". The results revealed that the critical required strain for formation of martensite band increased with cycling. This observation suggests that an increase in this critical strain level is another indication of functional fatigue.

Figure 4-9 (c) showed that at point 1, the local strain in 4 regions of the wire (“A”, “B”, “D” and near “F”) reached to a critical level, and four bands nucleated. Before the saturation of the martensitic transformation in the bands, as depicted in frame 3, the band that formed at “A” merged with band of “B”, and band that formed at area “D” merged with band of area “F”. As with previous cycles, the A/M bands stopped as they reached area “C”. Area “C” still resist the phase transformation, although the load-displacement curve suggesting that the applied load clearly passed the phase transformation region. The behavior is associated with the microscopic characteristics of the material. There are four possible explanations for this observation:

1- It is likely that a region of material was already in martensitic state before applying load. Therefore, the DIC did not detect the high strain associated with the phase transformation in this region.
2- The grain orientation in this zone is not in favor of phase transformation.
3- The presence of defects may alter the crystal structure of the area and affect its transformation behavior.
4- An intermediate R-phase is present in this region, which does not exhibit a high transformation strain like the austenite phase.

The XRD patterns of the 1mm sample in Figure 4-22 (b) showed that after 1000 cycles, a small amount of residual martensite was present in the macro-scaled non-transforming region. This confirms that the phase transformation occurred at the grain size scale, although the macroscopic bands did not expand in the region. The region undergoing transformation displayed stronger peaks of martensite, which suggests a more intense phase transformation in this region.

Figure 4-10 (a) showed that coalescence of unsaturated martensite bands did not result in high amount of residual strain. The 30th cycle left the highest residual strain near “A”, “B” and “F”, as displayed in Figure 4-10 (a). Despite the A/M interfaces stopping near areas "B" and "D," the results indicated that area "B" had a higher level of defect accumulation compared to area "D”. Point 4 of Figure 4-9 (c) showed that area “B” had a higher saturation level of martensite band at the peak point, which resulted in a higher defect accumulation in this area compared to “D”. The residual strain of "A" and "F" might be impacted by the local behavior outside of the field of view. It is unclear where the martensite bands stop or merge beyond this region. It should be noted that the measurement accuracy of DIC system is within the milli-strain range. So, the values below 0.1% may not be accurate. However, Figure 4-10 (a) and (b) represented a good approximation of the band formation pattern for the 30th and 100th cycles. The residual strain of the Cycle 500 did not follow the martensite pattern formation/annihilation anymore. As discussed in Chapter 2, functional fatigue results in a decrease in plateau stress, which may cause the material to be subjected to stress/strain higher than its plastic deformation limit. Plasticity is always involved with the superelastic behavior of the material (64) (240) (250) (253). Repeated cycling can result in the creation of defects that weaken the superelastic effect and change the balance between plasticity and superelasticity (64) (240) (250) (253). The residual strain pattern of Cycle 500 (Figure 4-10 (c)) displays that the balance between the superelasticity and plasticity has likely changed, with plastic residual strain surpassing the residual strain caused by superelasticity.

The elastic deformation at the beginning of the first cycle (Figure 4-2) suggested a more uniform initial microstructure. However, the initial cycling resulted in the development of inhomogeneous regions. In Chapter 3, it was also shown that grain refinement is the result of inhomogeneous transformation within the grains. Examination of the DIC results of the 1mm wire indicated that where the two martensite bands merged or the A/M interface stopped, the accumulation of the defects considerably increased. The level of saturation in the martensite bands impacts the accumulation of defects. Development of localized defects may provide enough activation energy for nucleation of the new bands. At the end of the 1st cycle of the 1mm wire, although 0.3% strain remained at the region “E”, it did not provide enough energy for nucleation of a band at the 2nd cycle. At the end of the 2nd cycle, 0.56% strain was accumulated in the area “E” that led to nucleation of a martensite band at the 3rd cycle. From these observations, it can be concluded that the areas with high volume of defects and residual strain are probably the most favorable regions for martensite band nucleation. After the 30th cycle, the band pattern of the wire was stabilized, and the wire exhibited the same band structure at the subsequent cycles. Evaluation of the local strain at the peak points of the cycles revealed that the level of saturation is not uniform across the bands, confirming the heterogeneous nature of the martensitic transformation (139) (254).

The results of the DIC analysis on the 0.5mm wire (section 4.3.2) indicate a similar behavior to the 1mm wire. The elastic behavior is uniform across all selected areas prior to the phase transformation, as depicted in Figure 4-11. After point “p”, the strain fluctuations did not surpass 1% and no martensite band formed within the region of interest. Before the strain reaches the critical level for martensite band nucleation, a martensite band expanded into the region and stopped below area “D”. Just prior to the band reaching area "A", a sudden decrease in its local strain was observed, which is due to the complex stress distribution near the A/M interface. The transformation from austenite to martensite involves a change in volume (90) (191). So, the interface experiences significant levels of longitudinal and lateral deformation (255). The higher volume of martensite exerts pressure to the interface, causing the material on the other side of the interface to experience a low level of compressive stress. The maximum strain achieved in the selected areas at the peak of the 1st cycle was 8.4%. This is a higher strain compared to the 7.5% strain recorded at the 1st cycle of the 1mm wire, which is consistent with the calculated global strains of the first cycle depicted in Figure 2-9 (d). The martensite band cessation below area “D” led to a higher accumulation of defect in this area, as shown in Figure 4-15. However, it did not provide enough activation energy for the martensite band nucleation during the 2nd cycle. At the 3rd cycle (Figure 4-12), upon loading, the local strain near area “D” reached 2%, resulting in the formation of a martensite band in this area. This band merged to another band at area “A”, causing the residual strain of area “A” to increase at a higher rate (see slope of the curve “A” in Figure 4-15 (b)). Cycle 4 displayed the same band pattern. Cycle 5 (Figure 4-13) had the same band pattern on loading. However, an austenite band nucleated near area “A” upon unloading. As shown in Figure 4-13 (c), at the maximum load of the 5th cycle (point 4), the strain near area “A” was slightly lower, indicating the lower saturation level of martensite band at this area. Upon unloading, the local strain near area “A” linearly dropped below 6%. It appears that this decrease in the local strain has created a preferred condition for the initiation of an austenite band, followed by a sudden drop in the local strain of the area to 2%. The austenite band merged at area “B”. However, it did not show a significant effect of the residual strain or defect accumulation rate of area “B” in Figure 4-15 (b). This observation confirms that as two bands merge, their initial saturation level determines the volume of the accumulated defects. The coalescence of two highly saturated martensite bands created a higher level of residual defects, compared to two austenite bands or two low strain martensite bands. This finding aligns with previous studies that have shown that the intersection of two martensite bands results in a high stress concentration (90) (191) (256). Additionally, the orientation of the two martensite bands can impact the volume of accumulated defects. The coalescence of two martensite bands with differing orientations can result in a high mismatch between their interfaces, leading to a higher density of dislocations. Cycles 6 and 7 exhibited the same band pattern as the 5th cycle. Figure 4-15 (b) showed that the residual strain of all areas (except for the non-transforming area “E”) converged towards each other. After the 7th cycle, the residual strain of the area “A” surpassed the other ones, which provided enough energy for nucleation of another martensite band near area “A” at the next cycle. As shown in Figure 4-14, when the local strains of areas “A” and “D” reached 3%, a martensite band nucleated. Upon unloading, when the local strain of area “A” passed 6%, an austenite band formed in this area. Figure 4-15 displayed that by the end of the 10th cycle, the residual strain in area “B” reached that of area “D”, which is the result of the coalescence of high-strain martensite bands in this area. The DIC data acquisition was stopped at this point and started over at the 30th cycle. As depicted in Figure 4-16 (d), the first martensite band of the 30th cycle formed at area “D”, similar to the previous cycles. As the local strain near area “B” reached the critical level, the second martensite band nucleated as well. Prior to nucleation of the martensite band at area “A”, the band of area “B” expanded into “A”. Upon unloading, an austenite band formed at area “A”.

The wire maintained this band structure in subsequent cycles, when two martensite bands formed at areas “B” and “D” under loading, followed by band expansion and coalescence near area “C”, and an austenite band formed at the area “A” upon unloading. Figure 4-17 shows that the highest residual strain at the end of the 30th cycle was located where the A/M interface stopped (near “D”). After that, the coalescence of the two martensite bands near “C”, created another high residual strain region. Figure 4-17 (a) suggests that nucleation of martensite and austenite bands in areas “A” and “B” also resulted in some defect accumulation. A small region at the very top of the Figure 4-17 (a) does not exhibit a significant accumulation of defects, suggesting that the martensite band likely stopped before that point and did not expand further above the field of view. This effect was more significant at the end of the 100th cycle (Figure 4-17 (b)). It can be seen from Figure 4-17 (b) that accumulation of defects is more localized after the 100th cycle, compared to the 30th one. Although the band pattern of the 500th cycle followed the same pattern as the 30th cycle, Figure 4-17 (c) shows that the residual strain at Cycle 500 did not follow the band formation/annihilation pattern any longer. The residual strain of the 500th cycle displayed a similar behavior to the one of the 1mm wire (Figure 4-10 (c)), which proved the growing effect of plasticity in the material microstructure.

The XRD pattern of the transforming and non-transforming regions of the 0.5mm wire is displayed in Figure 4-22 (c). The XRD pattern of the non-transforming region did not indicate a significant phase transformation. However, it showed a major martensite peak in $(1\bar{1}0)$ direction, indicating a pre-existing textured martensitic phase in this region before the cycling started. Another explanation for this observation may be related to the localized presence of R-phase in this specific region. As indicated in Appendix 2-B, the R-phase plays a role in shape memory effect rather than superelasticity (136). Additionally, the strain resulting from the martensitic transformation of R-phase is considerably lower compared to that of austenite (136). It is likely that the localized R-phase in the non-transforming region transformed to martensite at a low strain and was not recovered after unloading. A TEM observation may be helpful to investigate the microstructural features of the non-transforming region. The XRD pattern analysis of the as-received 0.5mm sample and its non-transforming region exhibited a small amount of R-phase, whereas the transforming region of the 0.5mm wire did not show any trace of R-phase. This finding further supports the localized non-homogenous nature of the nitinol sample.

Unlike the residual strain in the 1mm (Figure 4-8) and 0.5mm (Figure 4-15) wires, the 0.2mm wire did not reveal a drastic ascending trend at the first 10 cycles (Figure 4-21). It is in agreement with the global strain of the 0.2mm wire shown in Figure 2-9 (i).

As seen in Figure 4-18, all selected areas showed a uniform linear elastic behavior before the superelastic transformation started. Similar to the 1mm and 0.5mm wires, fluctuation in the local strain started after point "p". Before the local strain of the selected areas exceeded 1.3%, a martensite band expanded to the region. Upon unloading, at point 7, the local strain of area "A" dropped below the critical level of 5.3% and an austenite band nucleated. The band expanded and merged with another austenite band near area "D". As illustrated in Figure 4-21, area "C" showed a relatively lower amount of residual defect at the end of the 1st cycle. The higher residual strain of "A" and "B" is likely related to the proximity of these areas to the austenite band nucleation spot, and the strain at area "D" is likely related to the austenite bands coalescence near this area.

The DIC map of the next cycle (Figure 4-19) showed that the accumulation of defects near area “A” provided enough energy for nucleation of a martensite band near this area. Upon unloading, the strain level of areas “A” and “B” dropped below 1.3% and an austenite band formed between “A” and “B”. Area “D” displayed the highest saturation level of martensite band at the peak of the 2nd cycle (Figure 4-19 (c)) which caused an ascending trend in the residual strain of this area (frame 2 Figure 4-21 (a)).

During the 3rd cycle (Figure 4-20), the first martensite band formed at the area “A”, and the highest strain at the peak of the cycle was achieved at the area “D”, similar to the 2nd cycle. The high residual strain of the area “D” (Figure 4-21 (b)) at the end of the 3rd cycle is a result of the high strain achieved at this area along with the effect of coalescence of the low energy austenite bands near area “D”. The results of 0.5mm and 1mm wires also confirmed a slight increase in the local residual strain after coalescence of two low energy bands.

Comparing the residual strain of the three wires revealed that the accumulation of defects in the 0.2mm wire occurred at a significantly lower pace. The DIC of 0.2mm wire was tried five times and none of them showed an A/M interface stop. In all the 0.2mm wires, once the martensite band nucleated, it rapidly grew until it reached another band. Nayan et al (257) presented that the interface friction during the phase transformation results in self-heating within the material. Therefore, the A/M interface movement is impacted by the release of the latent heat of the transformation. As discussed in Chapter 2, the 0.2mm wire showed a better heat effect than the other wires, due to a larger surface area to volume ratio. Due to the localized nature of the martensitic transformation, the temperature distribution is non-uniform (191). The formation of dislocations at the interface zone is determined by the maximum temperature at the A/M interface at the peak of the cycle (134). This may result in high friction energy at A/M interface of the 1mm and 0.5mm wires and hinder the martensite band growth in some regions.

The XRD pattern of the 0.2mm wire is shown in Figure 4-22 (d). Since the DIC map of the 0.2mm wire did not indicate the presence of a non-transforming region, the XRD pattern was collected from a random region of the wire after 1000 cycles. The XRD pattern of the fatigued sample revealed a slight decrease in the austenite peak after 1000 cycles, along with a prominent martensite peak at $(1\bar{1}0)$, suggesting the presence of a textured growth of martensite in this direction.

4.5 Conclusion

The repeated cycling of superelastic nitinol leads to the formation of defects throughout the samples. However, the results indicate that the accumulation of these defects was not homogeneous. It was shown that formation and coalescence of the bands resulted in localized defect accumulation. The amount of defect accumulation depends on the energy level of the bands and interaction between the interfaces. Coalescence of the highly saturated martensite bands leave a higher number of defects behind, compared to the low energy austenite bands. During the initial cycles, all wires experienced changes in the macroscopic band pattern, as well as local fluctuations in the residual strain. This was followed by stability in the band pattern and a strain accumulation rate.

Within the initial cycles, accumulation of defects provided the activation energy for further band nucleation. The areas that A/M interface stopped had relatively high residual strain and; therefore they were more prone to martensite band formation. Once the local strain reached a critical level, a martensite band formed. With repeated cycling, the critical strain level required for band accumulation increased, while the plateau stress decreased.

As discussed in Chapter 2, the A/M interface in the 0.2mm wire had less self-heating effect and therefore less friction energy, compared to the 0.5mm and 1mm wires. The lower friction energy at the interface is likely the reason for the smooth expansion of martensite bands and lower accumulation of damage in the 0.2mm wire. Conversely, the high friction energy at the A/M interface of the 0.5mm and 1mm wires hindered the growth of martensite bands, resulting in higher damage accumulation.

4.6 Future Work

The formation of the first martensite band during the initial load is likely linked to the weak zones in the material, which are characterized by a higher density of microstructural defects in the initial microstructure. To accurately track the progress of the martensitic transformation and identify the location of the first martensite band, the 3-D HEDM technique is needed. This technique can also be used to predict the conditions that drive the formation of the first band. In Chapter 3, it was explained that the annealed sample did not show a significant phase transformation under load, and the non-annealed sample had too many grains for the HEDM technique. However, the grain refinement observed in the annealed sample during the initial cycles indicated that phase transformation was taking place on a smaller scale. By processing the strain data of the grains, it may be possible to identify the conditions that promote the nucleation of the first macroscopic martensite bands. This information can be used to develop a better understanding of the underlying mechanisms that drive the martensitic transformation, and to design more effective materials for a range of applications.

Based on the results obtained from DIC, it was found that in the 1mm and 0.5mm wires, certain regions may not undergo phase transformation, even when subjected to stress levels exceeding the material's stress plateau. Some reasons were suggested to justify these observations. To justify these observations, it is necessary to use Transmission Electron Microscopy (TEM) equipped with Selected Area Electron Diffraction (SAED) to examine the lattice defects and potential existence of R-phase or martensite phase in the material before cycling.

4.7 Research Limitation

The study has some limitations due to the localized phase transformation effect at the grips, which led the cameras to be focused on a small section in the middle of a 25mm sample. Therefore, only a limited section of the wires was studied. The phase transformation in superelastic nitinol is known to be highly localized. Although each test was repeated 4-5 times to ensure the consistency of the results, the sample size is still small, and this may not be representative of the entire population.

Additionally, for the 0.2mm wire, it was observed that the lower plateau was dropping into compressive stresses after initial loads. So, evaluating the evolution of the bands was not feasible, and only the initial cycles were studied. Increasing the lower cycling limit in the 0.2mm wire resulted in a mixed phase state upon unloading. To follow the martensite band annihilation pattern upon unloading, it was necessary to unload the sample until the lower band disappeared.

Appendix 4-A

Displacement-Controlled DIC Measurement of a 1mm Wire, Electropolished with a Neck Zone

Initially, the plan was to create a neck zone on the wires and focus the DIC camera on that specific region to study the formation and annihilation of martensite bands. To achieve this goal, an electropolishing process was established to create a necking zone on the samples. According to standard test methods for tension testing of metallic material (ASTM E8/E8M-16a), “the gauge length for the measurement of elongation of wire less than 4mm (0.125 inch) in diameter shall be as prescribed in product specification”. However, such information was not provided by the manufacturers. Alarcon et al (200) designed hourglass shaped samples, using a nitinol wire 1.78mm in diameter and reducing the diameter continuously down to 1.14 mm at the mid-cross-section (around %36), as shown at Figure 4-23.

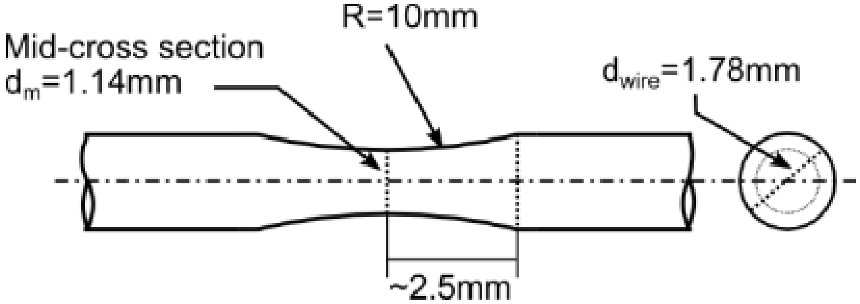

Figure 4-23-Geometry of hourglass shaped samples designed by Alarcon et al (200).

In this experiment, the objective is to achieve a similar shape with about 20-30% reduction in diameter and gauge length of 4-5mm. The electropolishing system used for wire surface treatment in Chapter 2 was utilized to form a neck on the wires. The actual distribution of ions at the electrolyte surface is higher which lead to higher electropolishing rate at the electrolyte/atmosphere interface (201) (258). Taking advantage of this point, a neck was created at the electrolyte/atmosphere interface. To ensure a gradual change in the neck zone, a laboratory jack was used. The applied current and the time of the electropolishing process varies depending on the wire length and diameter. Table 4-1 shows the electropolishing parameters of the 1mm sample that confirmed through experiment. The current was set as the table and the voltage was oscillating between 10-20V to maintain the constant electropolishing rate through a given time. After electropolishing one side of the wire, the wire was flipped, and the same procedure was applied to the other side. After electropolishing, the wires were rinsed with water, ultrasonically cleaned in ethanol, and dried.

Table 4-1- electropolishing variables used to create a neck zone on the wires

Sample size	Current (A)	Time (each side)	Surface treatment
1mm	0.6	3 min+ 30 sec	0.05 A for 30 sec

Figure 4-24 displays the neck zone created on the 1mm wire through the electropolishing process. The specified area inside the rectangular box shows the neck region on the sample. The average diameter of the wire at the neck zone was calculated as 0.825±0.017mm.

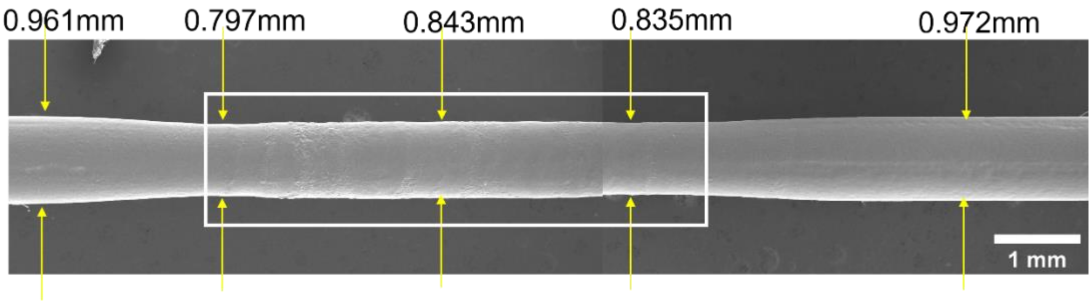

Figure 4-24-The 1mm wire with neck area.

The wire shown in Figure 4-24 was subjected to displacement-controlled fatigue test with the frequency of 0.1Hz. The upper and lower displacements were set at the midpoint of the 1mm wire plateau and below the lower plateau, respectively. The first cycle is depicted in Figure 4-25 (a). The Figure 4-25 (b) shows the detailed progressions of the actual strain field distribution along length of the wire at the points 0-9. The specified area in the frame 0 of Figure 4-25 (b) represents the neck zone. Figure 4-25 (a) displays a small plateau and change in the slope of the elastic region of the austenite at a point that is indicated by the number 1. Frame 1 of Figure

4-25 (b) shows that at this stress level a martensite band formed in the neck area and grows within the neck. As the stress reaches to the main plateau (point 3), the martensite band grows further than the neck region. As seen in Figure 2-9, the maximum global strain achieved at the end of the plateau for a 1mm wire was around 7.5%. At the maximum strain (point 5) the true mean strain in the neck region is measured as 8.5%, which is beyond the plateau strain of the 1mm wire. Upon unloading, the martensite elastically deforms, and the strain decreases within the martensite band. At point 6, the wire is still in its martensitic state. At point 7, an austenite band grows into the martensite at the upper side of the wire. Around point 8, an austenite band nucleates right below the neck region. As frame 9 shows, the reverse transformation is not complete at the end of the cycle. Some residual martensite is left at the neck region implying that the lower plateau of the neck region is below the lower limit of the fatigue test.

To evaluate and compare the local inhomogeneous strain distribution along the wire during the first cycle, five areas of the wire were selected, presented in Figure 4-25 (b). Figure 4-25 (c) shows the calculated mean strain of each area. Before the transformation started, all 5 areas were deforming homogeneously. At point 1, the transformation starts at the neck region and strain localization occurs. The areas “B”, “C” and “D” are located within the neck region, showing a higher strain at the maximum point. The results indicates that the strain within the neck region is inhomogeneous as well, and the upper parts of the neck (areas “B” and “C”) experience higher strain than the lower part (Area “D”). At the end of the cycle, the areas within the neck remained in martensitic state, while areas “A” and “E” were recovered to their original austenitic state.

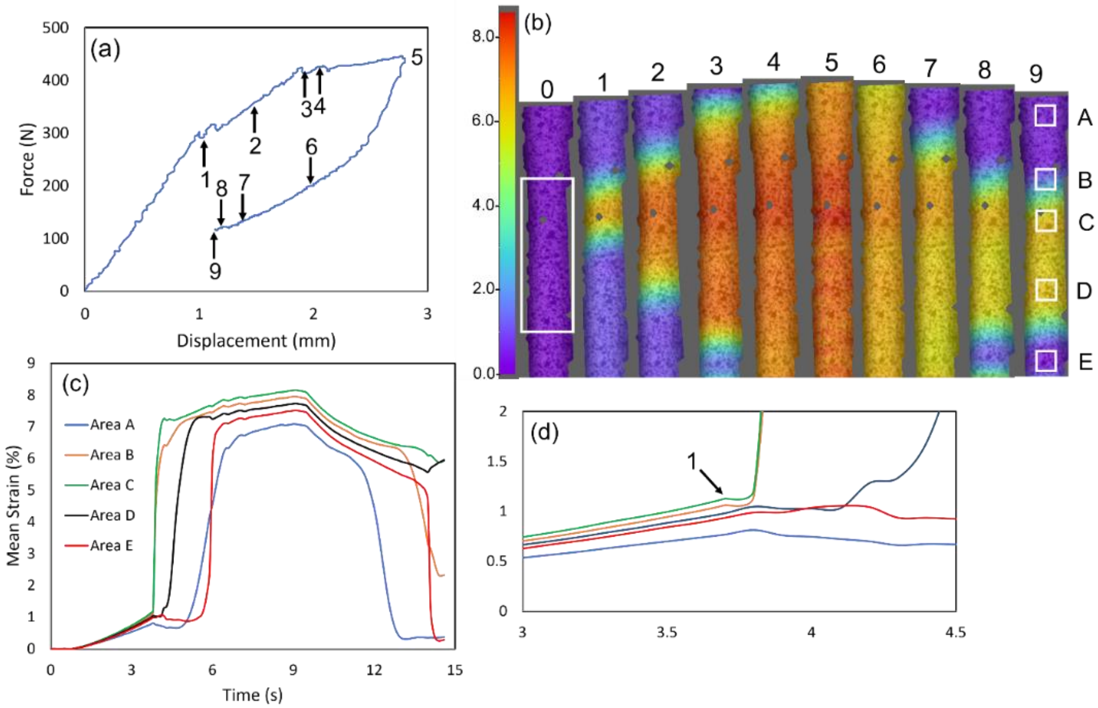

Figure 4-25- (a) The 1st cycle of the 1mm electropolished wire with a neck area, strain controlled (b) progression of the strain distribution along the length of wire at the points 0-9 (c)) the mean strain of the selected areas (d) enlargement of 0-2% strain.

The load-displacement curve and actual strain field distribution of the 2nd cycle is shown in Figure 4-26. The load-displacement curve of the 2nd cycle also exhibits a small plateau at point 1, after this point, the existing martensite band grows. At the maximum point (point 3), the true strain at the upper side of the neck reached 8.5%. At the end of the 2nd cycle (point 7), the neck still contains a martensite band. The region below the neck did not return to its original austenitic state at the end of the 2nd cycle, as depicted in the last frame of Figure 4-26 (b).

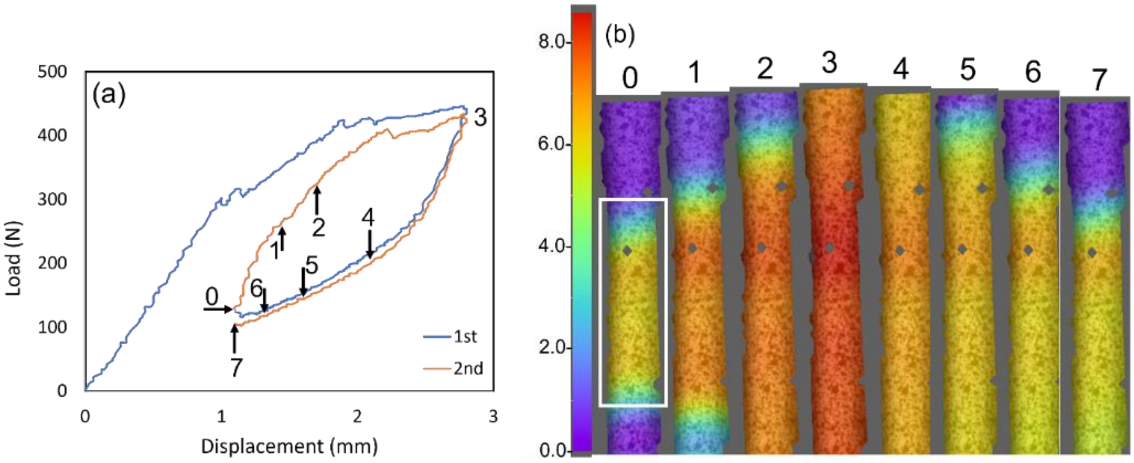

Figure 4-26- (a) The 2nd cycle of the 1mm electropolished wire with a neck area (b) progression of the strain distribution along the length of wire at the points 0-7.

The martensitic transformation of superelastic nitinol is inhomogeneous in nature (139). The test results showed that the neck decreases the onset of superelastic stress and promotes a localized stress concentration. As a result, subsequent tests were conducted on samples without the neck area.

Appendix 4-B

Displacement-Controlled DIC Measurement of the 0.2mm Wire: The Lower Fatigue Limit Was Set Just Above the End of the Lower Plateau

As shown in section 4.3.3, after just 30 cycles, the lower plateau stress of the 0.2mm dropped to below zero. To avoid compressive stresses on the wire, it was decided to slightly increase the lower fatigue limit. However, as displayed in Figure 4-27, at the end of the cycle (point 7), a large amount of residual martensite is left in the wire. The DIC result of the 0.2mm wire showed that the martensite band is persistent until the end point of the lower plateau. Therefore, a slight increase in the lower fatigue limit will result in a significant amount of residual martensite at the end of the cycle.

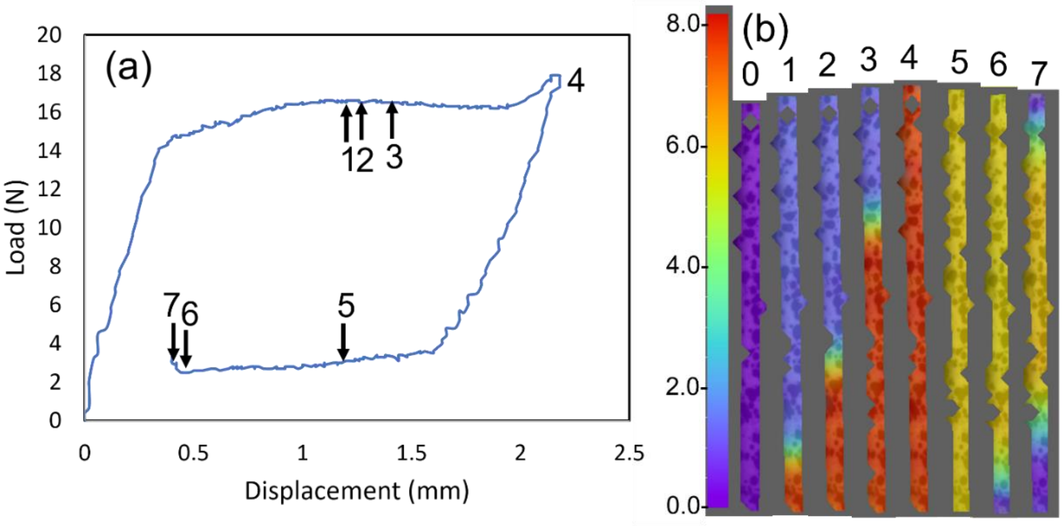

Figure 4-27- (a) The 1st cycle of the 0.2mm wire, displacement-controlled (b) progression of the strain distribution along the length of wire at the points 0-7.

Figure 4-28 shows that at the end of the cycle (frame 6), the residual martensite band shifts up.

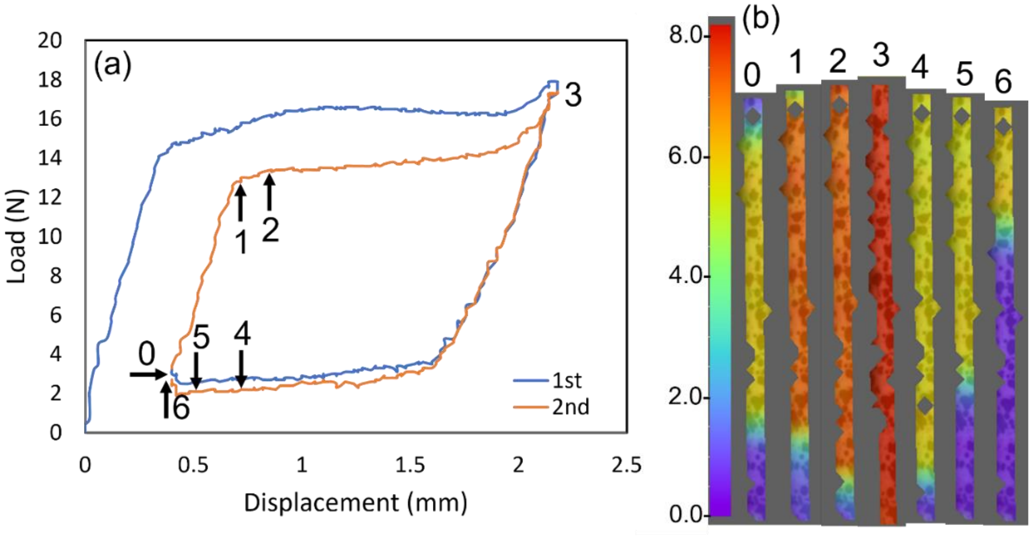

Figure 4-28- (a) The 2nd cycle of the 0.2mm wire, displacement-controlled (b) progression of the strain distribution along the length of wire at the points 0-6 (c) mean strain versus time of the selected areas of the 2nd cycle.

Figure 4-29 illustrates the 3rd cycle and the strain distribution of the 0.2mm wire. As Figure 4-29 (b) shows, the residual martensite band at the end of this cycle fully disappeared, or likely shifted up.

Cycles 4, 5 and 6 depicts a macroscopic martensite band structure similar to the 4th cycle, where the martensite bands all disappeared in this region of wire upon unloading. However, Figure 4-30 shows some residual martensite exist at the end of the 7th cycle.

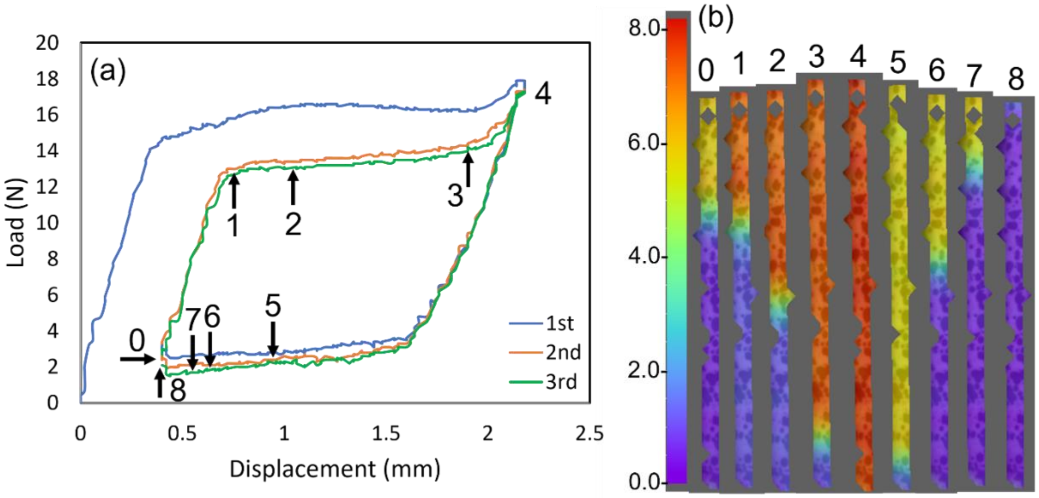

Figure 4-29- (a) The 3rd cycle of the 0.2mm wire, displacement-controlled (b) progression of the strain distribution along the length of wire at the points 0-8.

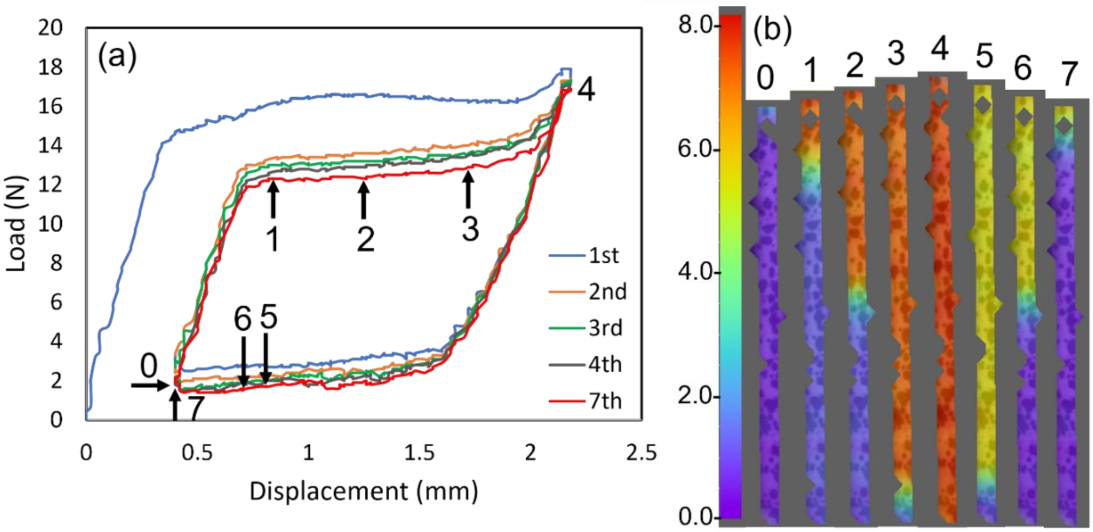

Figure 4-30- (a) The 7th cycle of the 0.2mm wire, displacement-controlled (b) progression of the strain distribution along the length of wire at the points 0-7.

The residual martensite band remained unchanged at the end of the 8th cycle. As shown in Figure 4-31 (b), the residual martensite band was larger at the end of the 9th cycle.

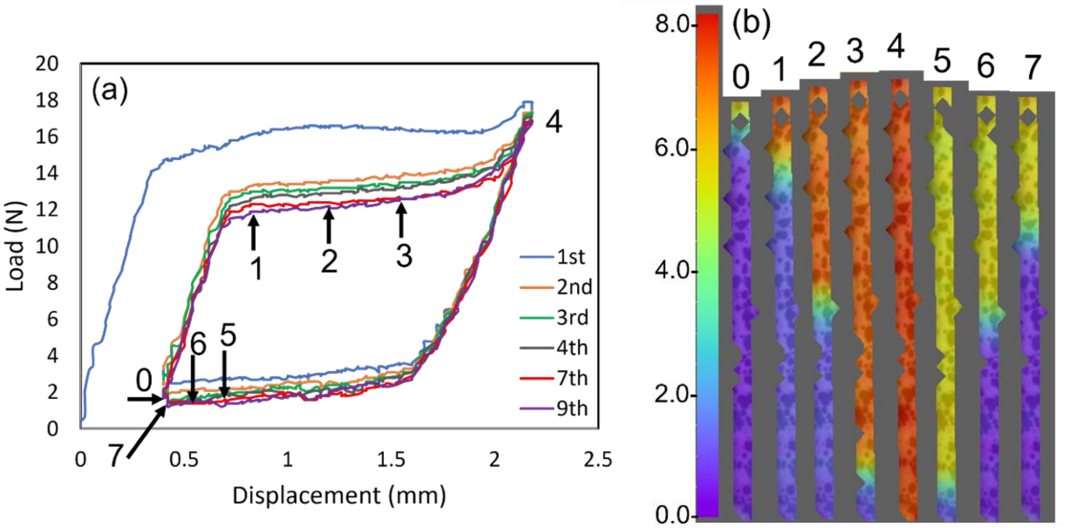

Figure 4-31- (a) The 9th cycle of the 0.2mm wire, displacement-controlled (b) progression of the strain distribution along the length of wire at the points 0-7.

The test result indicated that the martensite was not completely recovered at the end of the cycles in this sample. Residual bands remained in randomly dispersed areas of the wire. Some of the bands were out of view, while others were present and captured by the cameras.

Appendix 4-C

Stress-Controlled DIC Measurement of the As-Received 0.2mm Wire

To avoid compressive stresses at the end of the cycles, the 0.2mm wire was also examined under stress-controlled condition where the upper and lower fatigue limits were set at 500 MPa (slightly above the upper plateau stress of the wire) and 0, respectively. Figure 4-32 (a) shows that at the end of the 1st cycle, the martensite band fully disappear.

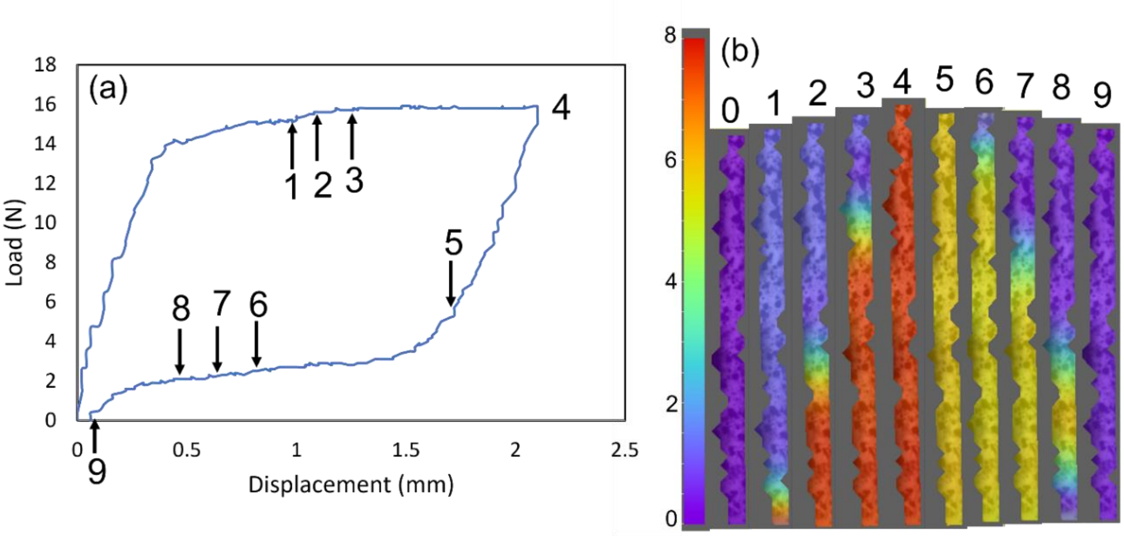

Figure 4-32- (a) The 1st cycle of the 0.2mm wire, stress controlled (b) progression of the strain distribution along the length of wire at the points 0-9.

The 2nd and 3rd cycle displayed the same trend. However, as Figure 4-33 shows, some residual martensite is left at the end of the 4th cycle.

The residual martensite band grew during the subsequent cycles. Figure 4-34 presents the 10th cycle and its strain distribution.

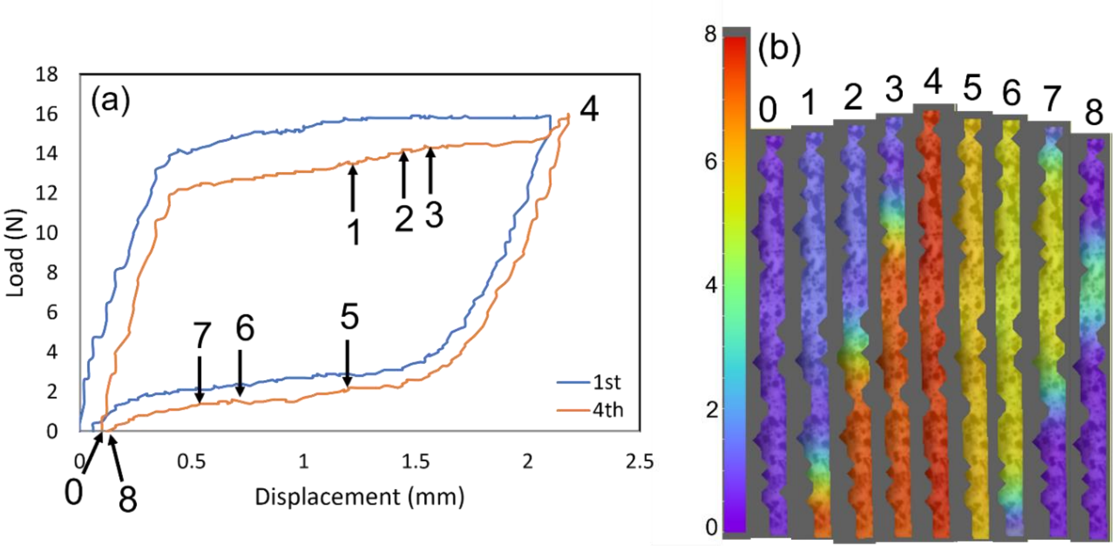

Figure 4-33- (a) The 4th cycle of the 0.2mm wire, stress controlled (b) progression of the strain distribution along the length of wire at the points 0-8.

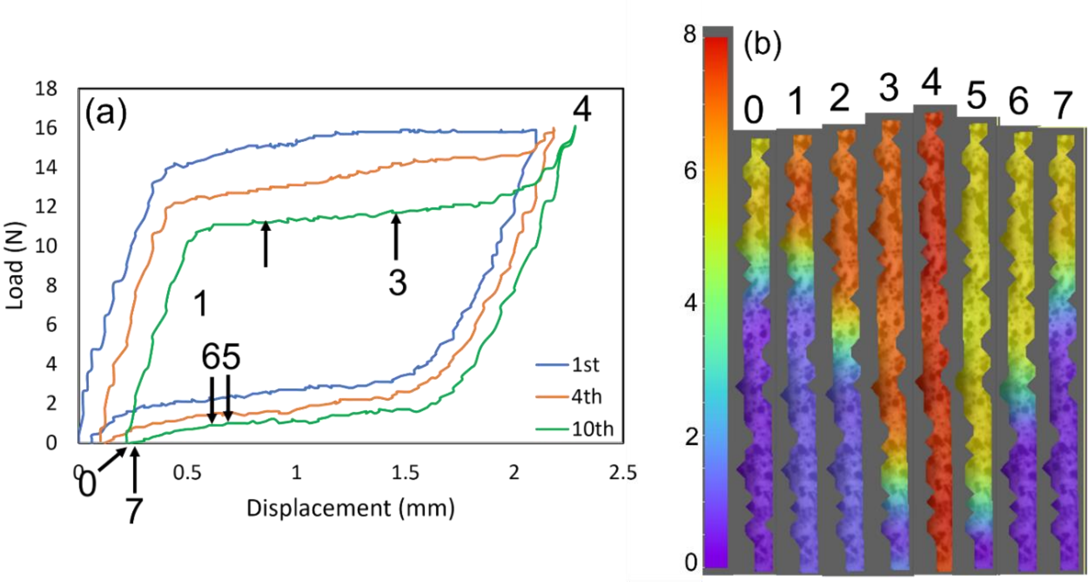

Figure 4-34-(a) The 10th cycle of the 0.2mm wire, stress controlled (b) progression of the strain distribution along the length of wire at the points 0-7.

Figure 4-35 shows the last frame of the cycles 1-10 of the 0.2mm wire cycled under stress-controlled condition.

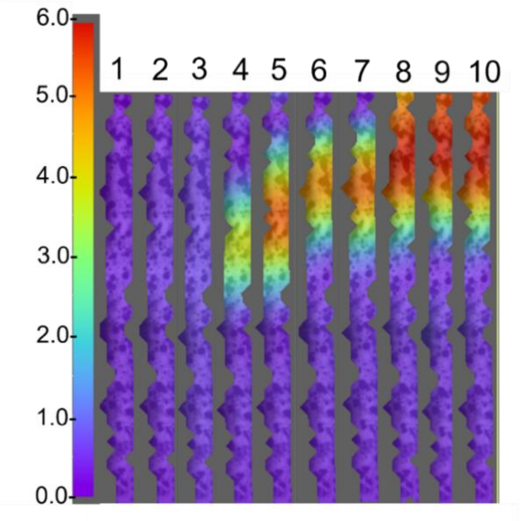

Figure 4-35- The last frames of the cycles 1-10.

Figure 4-36 shows the Cycle 30 along with its DIC measurement exhibiting the strain distribution during the Cycle 30. According to the Figure 4-36 (b), the upper side of the wire did not undergo phase transformation. Given that the martensitic transformation started at the onset of the plateau in Figure 4-36 (a), it is likely that a martensite band existed in the upper region that started growing as the stress reached the critical plateau level.

Figure 4-37 shows the 100th cycle and its strain distribution during cycling. The load-displacement curve of the 100th cycle indicated a significant decrease in superelastic hysteresis loop, implying an intense functional fatigue. Since the start and endpoint of the 100th cycle lays above 4% strain, it is likely that the wire at this cycle was already in martensitic state and the existing martensite band elastically deformed or got saturated at the peak point of the cycle.

The results showed that the functional fatigue in stress-controlled conditions is faster than in displacement-controlled conditions in superelastic nitinol. These observations can be explained as follows: The upper plateau of the superelastic nitinol decreased due to functional fatigue. It is likely that the upper limit of the fatigue test surpassed the yield stress of the material, which resulted in plastic deformation and a faster decrease in its functionality.

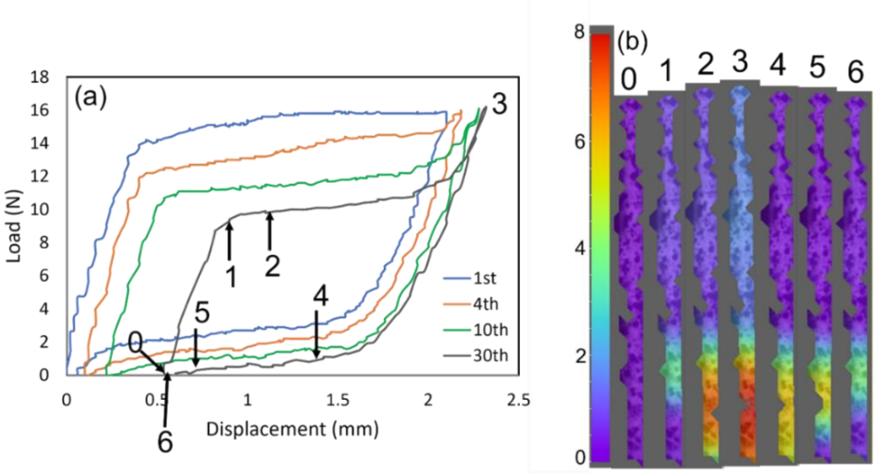

Figure 4-36- The 30th cycle of the 0.2mm wire, stress controlled (b) progression of the strain distribution along the length of wire at the points 0-6.

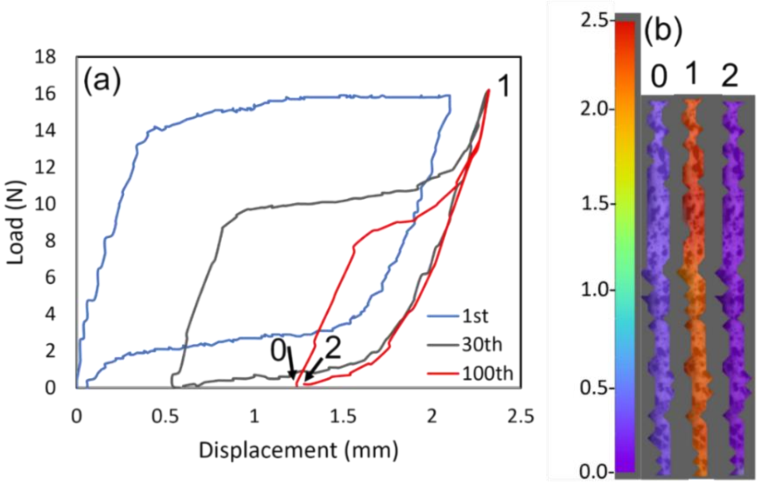

Figure 4-37- (a) The 100th cycle of the 0.2mm wire, stress controlled (b) progression of the strain distribution along the length of wire at the points 0-8.

5 CONCLUSION

This study investigated the impact of wire size and microstructural features on the superelastic behavior of nitinol wires. The microstructural analysis revealed that smaller wires had a higher density of internal cracks and defects, leading to greater susceptibility to surface defects. In other words, the fatigue crack initiation stage was accelerated in the smaller wire, resulting in a shorter life in terms of structural fatigue. However, these wires exhibited better functional fatigue, which can be attributed to their cooling rate effect.

The results showed that the superelastic properties of nitinol are highly dependent on its microstructure, which is influenced by its composition and thermal history. The grain growth heat treatment resulted in the formation of precipitates, which likely altered the material's composition and affected its superelastic temperature range. The annealed sample did not show an evident superelastic response under load, and no martensite grain spots were detected in its ff-HEDM diffraction pattern. However, grain refinement indicates that martensitic transformation is happening at the grain scale level.

In the context of 3-D techniques, functional fatigue is attributed to the permanent grain refinement. However, due to the grain segmentation process, tracking the grain strain after initial cycling becomes impractical. This is primarily because the size of these grains is reduced to a level below the resolution capacity of the ff-HEDM detector, making them impossible to detect. Combining ff-HEDM with other characterization techniques such as TEM or EBSD can overcome the challenges presented by the grain refinement. TEM and EBSD offer high-resolution imaging and orientation mapping capabilities, which assist in monitoring the evolution of the microstructure and grain orientation over time.

The formation of the first martensite band during the initial load was a factor that received less attention. As the applied stress reached the upper plateau stress, local strain fluctuations appeared on the strain map of DIC. The DIC maps displayed that the high strain macroscopic bands (i.e. the martensite bands) formed after a sudden strain increase in a random location, which was attributed to microstructural defects and weak zones. Within the initial cycles, the local accumulation of defects provides energy for the nucleation of new martensite bands in subsequent cycles.

The study also highlights the importance of microstructure and thermal history in determining the superelastic behavior of nitinol and provides insights into the mechanisms of fatigue and defect accumulation in these materials. The accumulation of defects during cyclic loading was found to be non-homogeneous, with localized defect accumulation due to the formation and coalescence of bands. The energy level of bands and interaction between interfaces affected defect accumulation. Although in this study the material is going through a mechanical cycling, the accumulation of the latent heat of transformation resulted in thermal stresses. Therefore, the heat conduction between the sample and the environment plays a key role in the grain refinement and functional fatigue of the wires. Overall, the study emphasizes the importance of microstructural features and wire size in determining the superelastic behavior of nitinol wires.

REFERENCES

1. M. C. Tanzi, S. Fare GC. Chapter 4 - Biomaterials and Applications. In: Foundations of Biomaterials Engineering. 2019. p. 199–287.
2. W. J. Buehler, Hyattsville, and R. C. Wiley R. Nickel-base-alloys. United States; 157,049, 1965.
3. H. M. Walia, W. A. Brantley HG. An initial investigation of the bending and torsional properties of nitinol root canal files. J Endod. 1988;14(7):346–51.
4. K. Otsuka XR. Physical metallurgy of Ti–Ni-based shape memory alloys. Prog Mater Sci [Internet]. 2005;50(5):511–678. Available from: https://doi.org/10.1016/j.pmatsci.2004.10.001
5. C. Wen, X. Yu, W. Zeng, S. Zhao, L. Wang, G. Wan, S. Huang HG and ZC. Mechanical behaviors and biomedical applications of shape memory materials: A review. AIMS Mater Sci. 2018;5(4):559–90.
6. Y. H. Zhi, X. M. Wang, Z. Z. Gao, Y. S. Liu ZFY. Mechanical property analysis of Nitinol defective stent under uniaxial loading/unloading. Materwiss Werksttech [Internet]. 2008;39(7):479–85. Available from: https://doi.org/10.1002/mawe.200800274
7. M. Mehrpouya and H. C. Bidsorkhi. MEMS Applications of NiTi Based Shape Memory Alloys: A Review. Micro Nanosyst. 2016;8(2):79–91.
8. J. M. Jani, M. Leary AS and MAG. A review of shape memory alloy research, applications and opportunities. Mater Des [Internet]. 2014;56:1078–1113. Available from: https://www.sciencedirect.com/science/article/abs/pii/S0261306913011345
9. J. Paine and C. Rogers. High velocity impact response of composites with surface bonded nitinol-SMA hybrid layers. 36th Struct Dyn Mater Conf [Internet]. 1995; Available from: https://doi.org/10.2514/6.1995-1409
10. A. L. McKelvey ROR. Fatigue-crack growth behavior in the superelastic and shape-memory alloy nitinol. Metall Mater Trans A [Internet]. 2001;32:731–743. Available from: https://doi.org/10.1007/s11661-001-1008-7
11. K. Yamauchi, I. Ohkata, K. Tsuchiya SM. Shape Memory and Superelastic Alloys, Applications and Technologies. Woodhead Publishing Series in Metals and Surface Engineering; 2011.
12. R. Chaudhari JJV and DMP. A Review on Applications of Nitinol Shape Memory Alloy. Recent Adv Mech Infrastruct [Internet]. 2021;123–32. Available from: https://doi.org/10.1007/978-981-33-4176-0_10

13. D. Kapoor. Nitinol for Medical Applications: A Brief Introduction to the Properties and Processing of Nickel Titanium Shape Memory Alloys and their Use in Stents. Johnson Matthey Technol Rev. 2017;61(1):66.

14. A. R. Pelton, V. Schroeder, M. R. Mitchell, X. -Y. Gong MB and SWR. Fatigue and durability of Nitinol stents. J Mech Behav Biomed Mater. 2008;1(2):153–64.

15. A. Toro, F. Zhou, M. H. Wu WVG and WZM. Characterization of Non-Metallic Inclusions in Superelastic NiTi Tubes. J Mater Eng Perform [Internet]. 2009;18:448–458. Available from: https://doi.org/10.1007/s11665-009-9410-1

16. T. Nguyen, H. Nguyen, M. Nguyen SK and RM. US patent, Heart valve prosthesis and methods of manufacture and use. United States; US7914569B2, 2011.

17. D. Scheinert, S. Scheinert, J. Sax, C. Piorkowski, S. Bräunlich, M. Ulrich GB and AS. Prevalence and Clinical Impact of Stent Fractures After Femoropopliteal Stenting. J Am Coll Cardiol. 2005;45(2):312–5.

18. D. B. Spenciner JJS. 6.2 - The effect of Nitinol on medical device innovation. In: Titanium in Medical and Dental Applications [Internet]. 2018. p. 571–82. Available from: https://doi.org/10.1016/B978-0-12-812456-7.00026-3

19. T. W. Duerig, K. N. Melton DS and CMW. Engineering aspects of shape memory alloys. Butterworth-Heinemann; 1990.

20. J. McNaney, V. Imbeni, Y. Jung PP and RR. An experimental study of the superelastic effect in a shape-memory Nitinol alloy under biaxial loading. Mech Mater [Internet]. 2003;35(10):969–86. Available from: https://doi.org/10.1016/S0167-6636(02)00310-1

21. X. Huang GJA and KMR. Crystal structures and shape-memory behaviour of NiTi. Nat Mater [Internet]. 2003;2:307–11. Available from: https://doi.org/10.1038/nmat884

22. K. Otsuka and XR. Recent developments in the research of shape memory alloys. Intermetallics [Internet]. 1999;7(5):511–28. Available from: https://doi.org/10.1016/S0966-9795(98)00070-3

23. R. Mirzaeifar, K. Gall, T. Zhu AY and RD. Structural transformations in NiTi shape memory alloy nanowires. J Appl Phys [Internet]. 2014;115(194307). Available from: https://doi.org/10.1063/1.4876715

24. C. H. Fu, M. P. Sealy YBG and XTW. Austenite-martensite phase transformation of biomedical nitinol by ball burnishing. J Mater Process Technol [Internet]. 2014;214(12):3122–30. Available from: https://doi.org/10.1016/j.jmatprotec.2014.07.019

25. C. M. Wayman KO. Shape Memory Materials. Cambridge University Press; 1999.

26. P. Sittner, M. Landa PL and VN. R-phase transformation phenomena in thermo-

mechanically loaded NiTi polycrystals. Mech Mater [Internet]. 2006;38(5–6):475–92. Available from: https://doi.org/10.1016/j.mechmat.2005.05.025

27. T. W. Duerig, D. E. Tolomeo and MW. An overview of superelastic stent design. Minim Invasive Ther Allied Technol. 2000;9(3–4):235–46.

28. Z. C. Lin, D. Mackiewicz, B. Anukhin HMH and KP. Study of anisotropy of nitinol and radiopaque nitinol hypotube. In: California, USA : Proceeding of the International Conference on Shape Memory and Superelastic Technologies. 2006. p. 681–92.

29. Schwartz M. Encyclopedia of Smart Materials. Wiley-VCH; 2002. 1176 p.

30. I. Baker. Fifty Materials That Make the World. Springer; 2018.

31. Lagoudas DC. Shape Memory Alloys: Modeling and Engineering Applications. Springer US; 2008.

32. M. Fouda MT and GE. Calibration of The Hysteresis Loop of SMA Wires Heated by Electric Current. In: 15th International Conference on Applied Mechanics and Mechanical Engineering. Cairo, Egypt; 2012.

33. H. Sehitoglu, R. Hamilton HJM and YC. Hysteresis in NiTi alloys. J Phys IV [Internet]. 2004;115:3–10. Available from: https://doi.org/10.1051/jp4:2004115001%0A

34. G. González-Sanz, D. Galé-Lamuela, D. Escolano-Margarit AB-C. Hysteretic Behavior and Ultimate Energy Dissipation Capacity of Large Diameter Bars Made of Shape Memory Alloys under Seismic Loadings. Metals (Basel) [Internet]. 2019;9:1099. Available from: https://doi.org/10.3390/met9101099

35. F. E. Wang. Bonding Theory for Metals and Alloys. Technology & Engineering, Elsevier; 2005. 256 p.

36. A. L. McKelvey ROR. On the temperature dependence of the superelastic strength and the prediction of the theoretical uniaxial transformation strain in Nitinol. Philos Mag A [Internet]. 2000;80(8):1759–68. Available from: https://doi.org/10.1080/01418610008219082

37. A. R. Pelton JD and SM. Optimisation of processing and properties of medical grade Nitinol wire. Minim Invasive Ther Allied Technol [Internet]. 2009;107–18. Available from: https://doi.org/10.3109/13645700009063057

38. S. Nemat-Nasser and WG. Superelastic and cyclic response of NiTi SMA at various strain rates and temperatures. Mech Mater [Internet]. 2006;38(5–6):463–474. Available from: https://doi.org/10.1016/j.mechmat.2005.07.004

39. O. Tyc, L. Heller MV and PS. Effect of temperature on fatigue of superelastic NiTi wires. Int J Fatigue. 2020;134(105470).

40. Chiang DT and C. Vacuum Arc Melting Processes for Biomedical Ni-Ti Shape Memory Alloy. In: MATEC Web of Conferences. 2015.

41. Pelton AR. Nitinol Fatigue: A Review of Microstructures and Mechanisms. J Mater Eng Perform [Internet]. 2011;20:613–617. Available from: https://doi.org/10.1007/s11665-011-9864-9

42. T. G. Bradley WAB and BMC. Differential scanning calorimetry (DSC) analyses of superelastic and nonsuperelastic nickel-titanium orthodontic wires. Am J Orthod Dentofac Orthop [Internet]. 1996;109(6):589–97. Available from: https://doi.org/10.1016/S0889-5406(96)70070-7

43. H. Sehitoglu, J. Jun, X. Zhang, I. Karaman, Y. Chumlyakov HJM and KG. Shape memory and pseudoelastic behavior of 51.5%Ni–Ti single crystals in solutionized and overaged state. Acta Mater [Internet]. 2001;49(17):3609–3620. Available from: https://doi.org/10.1016/S1359-6454(01)00216-6

44. S. Jiang, J. Yu LH and YZ. Investigation on Deformation Mechanisms of NiTi Shape Memory Alloy Tube under Radial Loading. Metals (Basel) [Internet]. 2017;7(7):268–77. Available from: https://doi.org/10.3390/met7070268

45. Robertson SW. On the Mechanical Properties and Microstructure of Nitinol for Biomedical Stent Applications. University of California, Berkeley; 2006.

46. Fasching DWN and A. A Study of the Effect of Diameter on the Fatigue Properties of NiTi Wire. Mater Eng Perform [Internet]. 2009;18:558–62. Available from: https://doi.org/10.1007/s11665-009-9415-9

47. T. Duerig, A. Pelton DS. An overview of nitinol medical applications. Mater Sci Eng [Internet]. 1999;273–275:149–60. Available from: https://doi.org/10.1016/S0921-5093(99)00294-4

48. D. Aibibu MH and CC. 6-An overview of braiding structure in medical textile: fiber-based implants and tissue engineering. In: Advances in Braiding Technology [Internet]. 2016. p. 171–90. Available from: https://doi.org/10.1016/B978-0-08-100407-4.00006-5

49. D. Stoeckel AP and TD. Self-expanding nitinol stents: material and design considerations. Eur Radiol. 2004;14(2):292–301.

50. T. Kim, K. Schmidt, C. Deemie, J. Wycech, H. Liang and SFG. Highly Flexible Precisely Braided Multielectrode Probes and Combinatorics for Future Neuroprostheses. Front Neurosci. 2019;13.

51. Hendrickson A. Mechanical Design for the Stage. Taylor & Francis; 2012.

52. C. Singh, C. S. Wong XW. Medical Textiles as Vascular Implants and Their Success to Mimic Natural Arteries. J Funct Biomater. 2015;6(3):500–25.

53. K. Lambrighs, I. Verpoest BV and MW. Influence of non-metallic inclusions on the fatigue properties of heavily cold drawn steel wires. Procedia Eng [Internet]. 2010;2(1):173–81. Available from: https://doi.org/10.1016/j.proeng.2010.03.019

54. M. Launey, S. Robertson, L. Vien, K. Senthilnathan PC and ARP. Influence of microstructural purity on the bending fatigue behavior of VAR-melted superelastic Nitinol. J Mech Behav Biomed Mater [Internet]. 2014;34:181–6. Available from: https://doi.org/10.1016/j.jmbbm.2014.02.008

55. S. W. Robertson, J. Stankiewicz, X. Y. Gong and ROR. Cyclic Fatigue of Nitinol. In: Proceedings of the International Conference on Shape Memory and Superelastic Technologies. Baden-Baden, Germany; 2004.

56. C. Cheng. A Review of Peripheral Vascular Deformations due to Respiration and Musculoskeletal Influences. J ASTM Int. 2008;5.

57. G. Choi, L. K. Shin, C. A. Taylor and CPC. In Vivo Deformation of the Human Abdominal Aorta and Common Iliac Arteries with Hip and Knee Flexion: Implications for the Design of Stent-Grafts. J Endovasc Ther. 2009;16(5):531–8.

58. M. J. Mahtabi, N. Shamsaei and MRM. Fatigue of Nitinol: The state-of-the-art and ongoing challenges. J Mech Behav Biomed Mater [Internet]. 2015;50:228–54. Available from: https://doi.org/10.1016/j.jmbbm.2015.06.010

59. M Newby. Estimation of Paris-Erdogan law parameters and the influence of environmental factors on crack growth. nternational J Fatigue [Internet]. 1991;13(4):291–301. Available from: https://doi.org/10.1016/0142-1123(91)90356-4

60. S. W. Robertson, A. R. Pelton ROR. Mechanical fatigue and fracture of Nitinol. Int Mater Rev. 2012;57(1):1–37.

61. A. L. McKelvey and R. O. Ritchie. Fatigue-crack propagation in Nitinol, a shape-memory and superelastic endovascular stent material. J Biomed Mater Res. 1999;47(3):301–8.

62. D. Sornette TM and YB. The Physical Origin of the Coffin-Manson Law in Low-Cycle Fatigue. Eur Lett. 1992;20:433–8.

63. C. Young and G. Subbarayan. Maximum Entropy Models for Fatigue Damage in Metals with Application to Low-Cycle Fatigue of Aluminum 2024-T351. Entropy [Internet]. 2019;21(10):967. Available from: https://doi.org/10.3390/e21100967

64. Y. You, J. Wang, X. Su, X. Guo, Z. Moumni WZ. Effect of plasticity on superelasticity and hysteretic dissipation of NiTi shape memory alloy. Mater Today Commun [Internet]. 2010;24(101137). Available from: https://doi.org/10.1016/j.mtcomm.2020.101137

65. A. R. Pelton, J. Fino-Decker, L. Vien, C. Bonsignore, P. Saffari ML and MRM. Rotary-bending fatigue characteristics of medical-grade Nitinol wire. J Mech Behav Biomed Mater [Internet]. 2013;27:19–32. Available from: https://doi.org/10.1016/j.jmbbm.2013.06.003

66. C. Bonsignore. Present and future approaches to lifetime prediction of superelastic nitinol. Theor Appl Fract Mech [Internet]. 2017;92:298–305. Available from: https://doi.org/10.1016/j.tafmec.2017.04.001

67. R. M. Tabanli, N. K. Simha BTB. Mean stress effects on fatigue of NiTi. Mater Sci Eng A [Internet]. 1999;273–275:644–648. Available from: https://doi.org/10.1016/S0921-5093(99)00340-8

68. M. J. Mahtabi, N. Shamsaei BR. Mean strain effects on the fatigue behavior of superelastic Nitinol alloys: An experimental investigation. Procedia Eng [Internet]. 2015;133:646–54. Available from: https://doi.org/10.1016/j.proeng.2015.12.645

69. K. N. Smith PW and THT. A Stress-strain Function for the Fatigue of Metals. Int J Mater Form. 1970;

70. A. Fatemi, D. F. Socie. A critical plane approach to multiaxial fatigue damage including out-of-phase loading. Fatigue Fract Eng Mater Struct [Internet]. 1988;11:149–65. Available from: https://doi.org/10.1111/j.1460-2695.1988.tb01169.x

71. C. Maletta, E. Sgambitterra, F. Furgiuele RC and AT. Fatigue of pseudoelastic NiTi within the stress-induced transformation regime: a modified Coffin–Manson approach. Smart Mater Struct. 2012;21(112001).

72. H. M. Paranjape, P. P. Paul, H. Sharma, P. Kenesei, J-S. Park, T. W. Duerig, L. C Brinson APS. Influences of Granular Constraints and Surface Effects on the Heterogeneity of Elastic, Superelastic, and Plastic Responses of Polycrystalline Shape Memory Alloys. J Mech Phys Solids [Internet]. 2017;102:46–44. Available from: https://doi.org/10.1016/j.jmps.2017.02.007

73. American Society for Testing and Materials (ASTM) International, Designation. 2018;

74. A. R. Pelton, S. M. Russell JD. The physical metallurgy of nitinol for medical applications. JOM [Internet]. 2003;55:33–7. Available from: https://doi.org/10.1007/s11837-003-0243-3

75. Russell DH and S. Nitinol melting, manufacture and fabrication. Minim Invasive Ther Allied Technol [Internet]. 2000;9(2):61–5. Available from: https://doi.org/10.3109/13645700009063051

76. S. Shabalovskaya JA and JVH. Recent observations of particulates in Nitinol. Mater Sci Eng A [Internet]. 2008;481:431–436. Available from: https://doi.org/10.1016/j.msea.2007.01.177

77. F. Yamashita, Y. Ide, S. Kato, K. Ueda, T. Narushima, S. Kise KI and MN. Effect of Nonmetallic Inclusions on Fatigue Properties of Superelastic Ti-Ni Fine Wire. Metals (Basel) [Internet]. 2019;9(9):999. Available from: https://doi.org/10.3390/met9090999

78. M. Patel DP and RB. The Effects of Varying Active Af Temperatures on the Fatigue Properties of Nitinol Wire. In: ASM Material and processing for medical devices conference and exposition (MPMD). 2005.

79. D. Catoor ZM and SK. Cyclic response and fatigue failure of Nitinol under tension–tension loading. J Mater Res [Internet]. 2019;34:3504–3522. Available from: https://doi.org/10.1557/jmr.2019.254

80. K. Senthilnathan, A. Shamimi, C. Bonsignore, H. Paranjape and TD. Effect of Prestrain on the Fatigue Life of Superelastic Nitinol. J Mater Eng Perform [Internet]. 2019;28:5946–5958. Available from: https://doi.org/10.1007/s11665-019-04334-2

81. H. M. Paranjape, P. P. Paul, B. Amin-Ahmadi, H. Sharma, D. Dale, J.Y. Ko, Y. I. Chumlyakov LCB and APS. In situ, 3D characterization of the deformation mechanics of a superelastic NiTi shape memory alloy single crystal under multiscale constrain. Acta Mater [Internet]. 2018;144:748–57. Available from: https://doi.org/10.1016/j.actamat.2017.11.026

82. K. Mikhail, L. Elena, G. Dmitriy, M. Peter WP. Influence of the Structure on the Strain-Controlled Fatigue of Nitinol. Mater Sci Forum. 2013;738–739:316–20.

83. B. Reinholz and S. Brinckmann. Phase transformations in the proximity of TiC precipitates in a NiTi matrix during fatigue. Int J Fatigue [Internet]. 2012;41:72–82. Available from: https://doi.org/10.1016/j.ijfatigue.2012.01.017

84. M. L. Bowers, X. Chen, M. D. Graef, P. M. Anderson MJM. Characterization and modeling of defects generated in pseudoelastically deformed NiTi microcrystals. Scr Mater [Internet]. 2014;78–79:69–72. Available from: https://doi.org/10.1016/j.scriptamat.2014.02.001

85. Chevalier L. Prediction of defects in metal forming: Application to wire drawing. J Mater Process Technol [Internet]. 1992;32(1–2):145–53. Available from: https://doi.org/10.1016/0924-0136(92)90171-N

86. Dixit US. 1 - Modeling of metal forming: a review. In: Mechanics of Materials in Modern Manufacturing Methods and Processing Techniques [Internet]. 2020. p. 1–30. Available from: https://doi.org/10.1016/B978-0-12-818232-1.00001-1

87. D. Song, G. Kang, Q. Kan CY and CZ. Experimental observations on uniaxial whole-life transformation ratchetting and low-cycle stress fatigue of super-elastic NiTi shape memory alloy micro-tubes. Smart Mater Struct. 2015;24(075004).

88. G. Eggeler, E. Hornbogen, A. Yawny AH and MW. Structural and functional fatigue of NiTi shape memory alloys. Mater Sci Eng A [Internet]. 2004;378(075004):24–33. Available from: https://doi.org/10.1016/j.msea.2003.10.327

89. C. Maletta, E. Sgambitterra, F. Furgiuele RC and AT. Fatigue properties of a pseudoelastic NiTi alloy: Strain ratcheting and hysteresis under cyclic tensile

loading. Int J Fatigue [Internet]. 2014;66:78–85. Available from: https://doi.org/10.1016/j.ijfatigue.2014.03.011

90. Y. Zhang, Z. Moumni, Y. You, W. Zhang JZ and GA. Multiscale TRIP-based investigation of low-cycle fatigue of polycrystalline NiTi shape memory alloys. Int J Plast [Internet]. 2019;115:307–329. Available from: https://doi.org/10.1016/j.ijplas.2018.12.003

91. L. C. Brinson IS and RL. Stress-induced transformation behavior of a polycrystalline NiTi shape memory alloy: micro and macromechanical investigations via in situ optical microscopy. J Mech Phys Solids [Internet]. 2004;52:1549–71. Available from: https://doi.org/10.1016/j.jmps.2004.01.001

92. R. Vaidyanathan, M. A. M. Bourke DCD. Texture, Strain, and Phase-Fraction Measurements during Mechanical Cycling in Superelastic NiTi. Metall Mater Trans A [Internet]. 2001;32:777–786. Available from: https://doi.org/10.1007/s11661-001-0093-y

93. H. M. R. Oliveira, A. D. O. Ramos, E. N. D. Grassi, C. J. D. Araújo WFA. On The Functional Fatigue of Nitinol Shape Memory Wires in Superelastic Regime: an Experimental Investigation. In: 22nd International Congress of Mechanical Engineering. 2013.

94. F. Sczerzenie GP and CB. Comparison of Inclusions in Cold Drawn Wire and Precursor Hot-Rolled Rod Coil in VIM-VAR Nickel-Titanium Alloy. J Mater Eng Perform [Internet]. 2011;20:752–756. Available from: https://doi.org/10.1007/s11665-011-9832-4

95. I. Serrano-Munoz, J. Buffiere, R. Mokso CV and YN. Location, location & size: defects close to surfaces dominate fatigue crack initiation. Sci Rep [Internet]. 2017;7(45239). Available from: https://doi.org/10.1038/srep45239

96. F. R. Phillips, R. W. Wheeler ABG and DCL. Evolution of internal damage during actuation fatigue in shape memory alloys. Int J Fatigue [Internet]. 2019;124:315–327. Available from: https://doi.org/10.1016/j.ijfatigue.2018.12.019

97. A. du Plessis, I. Yadroitsava, S. G. l. Rouxa, I. Yadroitsev, J. Fieres CR and PR. Prediction of mechanical performance of Ti6Al4V cast alloy based on microCT-based load simulation. J Alloys Compd [Internet]. 2017;724:267–74. Available from: https://doi.org/10.1016/j.jallcom.2017.06.320

98. Li SX. Effects of inclusions on very high cycle fatigue properties of high strength steels. Int Mater Rev [Internet]. 2013;57:92–114. Available from: https://doi.org/10.1179/1743280411Y.0000000008

99. S. W. Robertson, M. Launey, O. Shelley, I. Ong, L. Vien, K. Senthilnathan, P. Saffari SS and ARP. A statistical approach to understand the role of inclusions on the fatigue resistance of superelastic Nitinol wire and tubing. J Mech Behav Biomed

Mater. 2015;51:119–31.

100. A. Coda, S. Zilio, D. Norwich and FS. Characterization of Inclusions in VIM/VAR NiTi Alloys. J Mater Eng Perform [Internet]. 2012;21:2572–7. Available from: https://doi.org/10.1007/s11665-012-0366-1

101. F. Sczerzenie GV and CB. The Measurement of Total Inclusion Content in Nickel-Titanium Alloys. J Mater Eng Perform [Internet]. 2012;21:2578–2586. Available from: https://doi.org/10.1007/s11665-012-0377-y

102. J. A. Moore, D. Frankel, R. Prasannavenkatesan, A. G. Domel, G. B. Olson WKL. A crystal plasticity-based study of the relationship between microstructure and ultra-high-cycle fatigue life in nickel titanium alloys. Int J Fatigue [Internet]. 2016;91:183–94. Available from: https://doi.org/10.1016/j.ijfatigue.2016.06.006

103. J. A. Moore, J. Rusch, P. Shabani Nezhad, S. Manchiraju DE. Effects of martensitic phase transformation on fatigue indicator parameters determined by a crystal plasticity model. Int J Fatigue [Internet]. 2023;168(107457). Available from: https://doi.org/10.1016/j.ijfatigue.2022.107457

104. P. P. Paul, M. Fortman, H M. Paranjape, P. M. Anderson, A. P. Stebner LCB. Influence of Structure and Microstructure on Deformation Localization and Crack Growth in NiTi Shape Memory Alloys. Shape Mem Superelasticity [Internet]. 2018;4:285–93. Available from: https://doi.org/10.1007/s40830-018-0172-1

105. A. Scheiner JTM and TPK. A study of the fatigue properties of small diameter wires used in intramuscular electrodes. J Biomed Mater Res. 1991;25(5):589–608.

106. C. Y. Dai, B. Zhang, J. Xu GPZ. On size effects on fatigue properties of metal foils at micrometer scales. Mater Sci Eng A [Internet]. 2013;575:217–22. Available from: https://doi.org/10.1016/j.msea.2013.03.064

107. R. Hofbeck, K. Hausmann BI and HUK. Fatigue of very thin copper and gold wires. Scr Metall [Internet]. 1986;20(11):1601–5. Available from: https://doi.org/10.1016/0036-9748(86)90403-5

108. H. D. Merchant, M. G. Minor YLL. Mechanical fatigue of thin copper foil. J Electron Mater [Internet]. 1999;28:998–1007. Available from: https://doi.org/10.1007/s11664-999-0176-x

109. S. M. Ueland and C. A. Schuh. Superelasticity and fatigue in oligocrystalline shape memory alloy microwires. Acta Mater [Internet]. 2012;60(1):282–92. Available from: https://doi.org/10.1016/j.actamat.2011.09.054

110. H. Soul, A. Isalgue, A. Yawny VT and FCL. Pseudoelastic fatigue of NiTi wires: frequency and size effects on damping capacity. Smart Mater Struct. 2010;19(8).

111. K. Hono, M. Ohnuma, M. Murayama, S. Nishida, A. Yoshie TT. Cementite decomposition in heavily drawn pearlite steel wire. Scr Mater [Internet].

2001;44(6):977–83. Available from: https://doi.org/10.1016/S1359-6462(00)00690-4

112. N. Guo, T. Liu, B. Luan BW and QL. Dislocation density and configuration in fully pearlitic steel during wire drawing. Mater Res Innov [Internet]. 2014;18(sup4):S4-249-S4-254. Available from: https://doi.org/10.1179/1432891714Z.000000000688

113. J. Toribio FA and RR. Evolution of non-metallic inclusions with cold drawing in progressively cold drawn eutectoid pearlitic steel wires. Procedia Struct Integr [Internet]. 2021;33:1209–14. Available from: https://doi.org/10.1016/j.prostr.2021.10.137

114. S. Daly, A. Miller GR and KB. An experimental investigation of crack initiation in thin sheets of nitinol. Acta Mater [Internet]. 2007;55:6322–6330. Available from: https://doi.org/10.1016/j.prostr.2021.10.137

115. K. I. Aycock, J. D. Weaver, H. M. Paranjape, K. Senthilnathan, C. Bonsignore BAC. Full-field microscale strain measurements of a nitinol medical device using digital image correlation. J Mech Behav Biomed Mater. 2021;114.

116. V. C. Shen, C. H. Bumgardner, L. Actis JR and JP. 3D digital image correlation evaluation of arthrodesis implants. Clin Biomech [Internet]. 2020;71:29–36. Available from: https://doi.org/10.1016/j.clinbiomech.2019.10.011

117. J. Park, S. Yoon, T. Kwon KP. Assessment of speckle-pattern quality in digital image correlation based on gray intensity and speckle morphology. Opt Lasers Eng [Internet]. 2017;91:62–72. Available from: https://doi.org/10.1016/j.optlaseng.2016.11.001

118. Y. Su, Q. Zhang XX and ZG. Quality assessment of speckle patterns for DIC by consideration of both systematic errors and random errors. Opt Lasers Eng [Internet]. 2016;86:132–42. Available from: https://doi.org/10.1016/j.optlaseng.2016.05.019

119. G. Crammond SWB and JMD-B. Speckle pattern quality assessment for digital image correlation. Opt Lasers Eng [Internet]. 2013;51(12):1368–78. Available from: https://doi.org/10.1016/j.optlaseng.2013.03.014

120. K. S. Chan, J. W. Tian BY and PKL. Evolution of Slip Morphology and Fatigue Crack Initiation in Surface Grains of Ni200. Metall Mater Trans A [Internet]. 2009;40:2545–2556. Available from: https://doi.org/10.1007/s11661-009-9980-4

121. Z. H. Stachurski GW and XT. Fracture mechanics of metallic glasses. In: An Introduction to Metallic Glasses and Amorphous Metals. Elsevier; 2021.

122. V. Gaur, V. Doquet, E. Persent, C. Mareau ER and JK. Surface versus internal fatigue crack initiation in steel: Influence of mean stress. Int J Fatigue [Internet]. 2016;82:437–48. Available from: https://doi.org/10.1016/j.ijfatigue.2015.08.028

123. E. Kassab, A. Marquardt, L. Neelakantan, M. Frotscher, F. Schreiber, T. Gries, S. Jockenhoevel JG and GE. On the electropolishing of NiTi braided stents – challenges and solutions. Materwiss Werksttech [Internet]. 2014;45. Available from: https://doi.org/10.1002/mawe.201400220

124. K. Khanlari, Q. Shi, X. Yan, K. Hu, C. Tan, P. Kelly, W. Zhang, P. Cao, X. Wang XL. Printing of NiTinol parts with characteristics respecting the general microstructural, compositional and mechanical requirements of bone replacement implants. Mater Sci Eng A [Internet]. 2022;839(142839). Available from: https://doi.org/10.1016/j.msea.2022.142839

125. A. Kokkinos VK and DA. The Effect of Thermal Ageing on The Transformation Temperatures of Superelastic Nitinol Tubing. Int J New Technol Res [Internet]. 2017;3:47–51. Available from: https://doi.org/10.1016/j.msea.2022.142839

126. X. Huang YL. Effect of annealing on the transformation behavior and superelasticity of NiTi shape memory alloy. Scr Mater. 2001;45(2):153–60.

127. F. Jahanbazi Asl MK and FK. The effects of shape-setting on transformation temperatures of pseudoelastic shape memory alloy springs. J Sci Adv Mater Devices [Internet]. 2019;4:568–76. Available from: https://doi.org/10.1016/j.jsamd.2019.10.005

128. M. Carl, J. D. Smith BVD and MY. Effect of Ni-Content on the Transformation Temperatures in NiTi-20 at. % Zr High Temperature Shape Memory Alloys. Metals (Basel) [Internet]. 2017;7(11):511. Available from: https://doi.org/10.3390/met7110511

129. J. J. Zhou, F. C. Ma PL and XKL. Effects of heat treatment on superelasticity and phase transformation of nitinol shape memory alloy wires. Cailiao Rechuli Xuebao/Transactions Mater Heat Treat [Internet]. 2017;38(12):114–20. Available from: http://dx.doi.org/10.13289/j.issn.1009-6264.2017-0339

130. P. Li, Y. Wang, F. Meng LC and ZH. Effect of Heat Treatment Temperature on Martensitic Transformation and Superelasticity of the Ti49Ni51 Shape Memory Alloy. Mater. 2019;12(16).

131. P. Souvatzis, D. Legut OE and MIK. Ab initio study of interacting lattice vibrations and stabilization of the β phase in Ni-Ti shape-memory alloy. Phys Rev B. 2010;81(9).

132. J. Frenzel, A. Wieczorek, I. Opahle, B. Maaß RD and GE. On the effect of alloy composition on martensite start temperatures and latent heats in Ni–Ti-based shape memory alloys. Acta Mater [Internet]. 2015;90:213–31. Available from: https://doi.org/10.1016/j.actamat.2015.02.029

133. Z. Wang, J. Luo, W. Kuang, M. Jin, G. Liu XJ and YS. Strain rate effect on the thermomechanical behavior of NiTi shape memory alloys: A literature review.

Metals (Basel) [Internet]. 2023;13(1):58. Available from: https://doi.org/10.3390/met13010058

134. Q. Kan, C. Yu , G. Kang JL and WY. Experimental observations on rate-dependent cyclic deformation of super-elastic NiTi shape memory alloy. Mech Mater [Internet]. 2016;97:48–58. Available from: https://doi.org/10.1016/j.mechmat.2016.02.011

135. J. F. Grandfield and D. G. Eskin. Essential Readings in Light Metals, Volume 3, Cast Shop for Aluminum Production. Springer International Publishing; 2016.

136. L. A. Santos, P. D. Resende MGAB and VTLB. Effects of R-Phase on Mechanical Responses of a Nickel-Titanium Endodontic Instrument: Structural Characterization and Finite Element Analysis. Sci World J. 2016;

137. C. L. Lach, T. L. Turner KMT and RNS. Effects of thermomechanical history on the tensile behavior of Nitinol ribbon. In: Smart Structures and Materials 2002: Active Materials: Behavior and Mechanics. San Diego, California, United States; 2002.

138. M. M. Islam, P. Bayati, M. Nematollahi, A. Jahadakbar, M. Elahinia MH. Strain rate dependent micromechanical properties of NiTi shape memory alloys: Laser powder bed fusion versus casting. Forces Mech [Internet]. 2021;5(100055). Available from: https://doi.org/10.1016/j.finmec.2021.100055

139. S. Daly GR and KB. Stress-induced martensitic phase transformation in thin sheets of Nitinol. Acta Mater [Internet]. 2007;55(10):3593–600. Available from: https://doi.org/10.1016/j.actamat.2007.02.011

140. Windl MF-XW and W. Lattice stability, elastic constants and macroscopic moduli of NiTi martensites from first principles. Acta Mater [Internet]. 2008;56(20):6232–45. Available from: https://doi.org/10.1016/j.actamat.2008.08.043

141. P. Sittner, L. Heller, J. Pilch, C. Curfs, T. Alonso and DF. Youngs modulus of austenite and martensite phases in superelastic NiTi wires. J Mater Eng Perform [Internet]. 2014;23:2303–2314. Available from: https://doi.org/10.1007/s11665-014-0976-x

142. W. J. Plumbridge. Review: Fatigue-crack propagation in metallic and polymeric materials. J Matreials Sci [Internet]. 1972;7:939–962. Available from: https://doi.org/10.1007/BF00550441

143. M. D. Sangid. The physics of fatigue crack initiation. Int J Fatigue [Internet]. 2013;57:58–72. Available from: https://doi.org/10.1016/j.ijfatigue.2012.10.009

144. H. Itoga, K. Tokaji MN and H-NK. Effect of surface roughness on step-wise S–N characteristics in high strength steel. Int J Fatigue [Internet]. 2003;25(5):379–385. Available from: https://doi.org/10.1016/S0142-1123(02)00166-4

145. M. Nakatani, H. Masuo YT and YM. Effect of Surface Roughness on Fatigue Strength of Ti-6Al-4V Alloy Manufactured by Additive Manufacturing. Procedia Struct Integr

[Internet]. 2019;19:294–301. Available from: https://doi.org/10.1016/j.prostr.2019.12.032

146. N. A. Alang, N. A. Razak AKM. Effect of Surface Roughness on Fatigue Life of Notched Carbon Steel. Int J Eng Technol IJET-IJENS. 2011;11.

147. W. C. Young RGB. Roark's Formulas for Stress and Strain. McGraw-Hill; 2002.

148. Pluvinage G. Fracture and Fatigue Emanating from Stress Concentrators. Springer Netherlands; 2007.

149. Feng Q. Test Size and Volume Effects on Fatigue Behavior of Bulk Metallic Glasses (BMGs). The University of Tennessee, Knoxville; 2012.

150. Z. Zheng, S. Yuan, T. Sun SP. Fractographic study of fatigue cracks in a steel car wheel. Eng Fail Anal [Internet]. 2015;47 A:199–207. Available from: https://doi.org/10.1016/j.engfailanal.2014.09.010

151. S. Gupta, A. R. Pelton, J. D. Weaver, X. Gong and SN. High compressive pre-strains reduce the bending fatigue life of nitinol wire. J Mech Behav Biomed Mater. 2015;44:96–108.

152. O. Tyc JP and PS. Fatigue of superelastic NiTi wires with different plateau strain. Procedia Struct Integr [Internet]. 2016;2:1489–96. Available from: https://doi.org/10.1016/j.prostr.2016.06.189

153. Timoshenko JMG and SP. Mechanics of Materials. United Kingdom: Stanley Thornes; 1999.

154. N. Afzal, I. M. Ghauri FEM and FA. Mechanical response of proton beam irradiated nitinol. Phys B Condens Matter [Internet]. 2011;406(1):8–11. Available from: https://doi.org/10.1016/j.physb.2010.09.040

155. T. W. Duerig KB. The Influence of the R-Phase on the Superelastic Behavior of NiTi. Shape Mem Superelasticity [Internet]. 2015;1:153–161. Available from: https://doi.org/10.1007/s40830-015-0013-4

156. J. Uchil, K.P. Mohanchandra KKM and KG. Thermal and electrical characterization of R-phase dependence on heat-treat temperature in Nitinol. Phys B Condens Matter [Internet]. 1998;253(1–2):83–9. Available from: https://doi.org/10.1016/S0921-4526(98)00378-0

157. M. Kök, F. Dağdelen AA and YA. The change of transformation temperature on NiTi shape memory alloy by pressure and thermal ageing. 9th Int Conf Magn Supercond Mater. 2016;667(012011).

158. X. Ren, N. Miura, J. Zhang, K. Otsuka, K. Tanaka, M. Koiwa, T. Suzuki, Y .I. Chumlyakov MA. A comparative study of elastic constants of Ti–Ni-based alloys prior to martensitic transformation. Mater Sci Eng A [Internet]. 2001;312(1–2):196–206. Available from: https://doi.org/10.1016/S0921-5093(00)01876-1

159. I. Shishkovsky, V. Sherbakoff IY and IS. Peculiar features of electrical resistivity and phase structure in 3-D porous nitinol after selective laser sintering/melting process. J Mech Eng Sci [Internet]. 2012;226(12):2982–2989. Available from: https://doi.org/10.1177/095440621244076

160. L. Bataillard, J-E. Bidaux RG. Interaction between microstructure and multiple-step transformation in binary NiTi alloys using in-situ transmission electron microscopy observations. Philos Mag A [Internet]. 1997;78(2):327–44. Available from: https://doi.org/10.1080/01418619808241907

161. J. Khalil-Allafi, G. Eggeler, A. Dlouhy WWS and CS. On the influence of heterogeneous precipitation on martensitic transformations in a Ni-rich NiTi shape memory alloy. Mater Sci Eng A [Internet]. 2004;378(1–2):148–51. Available from: https://doi.org/10.1016/j.msea.2003.10.335

162. X. B. Wang BV and JVH. R-phase transformation in NiTi alloys. Mater Sci Technol [Internet]. 2014;30:1517–29. Available from: https://doi.org/10.1179/1743284714Y.0000000590

163. J. Khalil-Allafi WWS and DMT. Space group and crystal structure of the R-phase in binary NiTi shape memory alloys. Acta Mater [Internet]. 2006;54:3171–3175. Available from: https://doi.org/10.1016/j.actamat.2006.02.040

164. J. Butlera, P. Tiernan SAMT and AAG. Probing Martensitic Transition in Nitinol Wire: A Comparison of X-ray Diffraction and Other Techniques. API Conf Proceeding [Internet]. 2011;1315(104). Available from: https://doi.org/10.1063/1.3552318

165. M. Iijima, W.A. Brantley, W. H. Guo, W. A. T. Clark TY and IM. X-ray diffraction study of low-temperature phase transformations in nickel–titanium orthodontic wires. Dent Mater [Internet]. 2008;24:1454–1460. Available from: https://doi.org/10.1016/j.dental.2008.03.005

166. V. Cnudde and M. N. Boone. High-resolution X-ray computed tomography in geosciences: A review of the current technology and applications. Earth-Science Rev [Internet]. 2013;123:1–17. Available from: https://doi.org/10.1016/j.earscirev.2013.04.003

167. L. Salvo, M. Suery, A. Marmottant, N. Limodin DB. 3D imaging in material science: Application of X-ray tomography. Comptes Rendus Phys [Internet]. 2010;11(9–10):641–9. Available from: https://doi.org/10.1016/j.crhy.2010.12.003

168. T. Leißner, A. Diener, E. Löwer, R. Ditscherlein, K. Krüger AK and UAP. 3D ex-situ and in-situ X-ray CT process studies in particle technology –A perspective. Adv Powder Technol [Internet]. 2020;31:78–86. Available from: https://doi.org/10.1016/j.apt.2019.09.038

169. J. H. Kinney, Q. C. Johnson, U. Bonse, M. C. Nichols, R. A. Saroyan, R. Nusshardt, R. Pahl and JMB. Three-Dimensional X-Ray Computed Tomography in Materials

Science. MRS Bull [Internet]. 1988;13(1):13–8. Available from: https://doi.org/10.1557/S0883769400066525

170. M. C. Fonseca, B. H. Araujo, C. S. Dias, N. L. Archilha, D. P. Neto, E. Cavalheiro, H. Westfahl AJS and KGF. High-resolution synchrotron-based X-ray microtomography as a tool to unveil the three-dimensional neuronal architecture of the three-dimensional neuronal architecture of the brain. Sci Rep [Internet]. 2018;8(12074). Available from: https://doi.org/10.1038/s41598-018-30501-x

171. L. Salvo, P. Cloetens, E. Maire, S. Zabler, J. Blandin, J. Buffière, W. Ludwig, E. Boller DB and CJ. X-ray micro-tomography an attractive characterisation technique in materials science. Nucl Instruments Methods Phys Res B [Internet]. 2003;200:237–86. Available from: https://doi.org/10.1016/S0168-583X(02)01689-0

172. T. Shearer, R. S. Bradley, L. A. Hidalgo-Bastida, M. J. Sherratt SHC. Three-dimensional visualisation of soft biological structures by X-ray computed micro-tomography. J Cell Sci. 2016;129:2483–92.

173. K. Orhan. Micro-computed Tomography (micro-CT) in Medicine and Engineering. Ankara: Springer; 2020.

174. Xue MVS and J. State of the art of Micro-CT applications in dental research. Int J Oral Sci. 2009;1(4):177–88.

175. J. D. B. O'Sullivan, J. Behnsen, T. Starborg, A. S. MacDonald, A. T. Phythian-Adams, K. J. Else SMC and PJW. X-ray micro-computed tomography (µCT): an emerging opportunity in parasite imaging. Parasitology. 2018;145(7):848–54.

176. R. E. Newnham. Properties of Materials; Anisostropy, Symmetry, Structure. Oxford University Press; 2004.

177. J. S. Park, X. Zhang, P. Kenesei, S. L. Wong, M. Li JA. Far-Field High-Energy Diffraction Microscopy: A Non-Destructive Tool for Characterizing the Microstructure and Micromechanical State of Polycrystalline Materials. Micros Today. 2017;25(5):36–45.

178. J. V. Bernier, R. M. Suter ADR and JA. High-Energy X-Ray Diffraction Microscopy in Materials Science. Annu Rev Mater Res. 2020;50:395–436.

179. A. N. Bucsek, D. C. Pagan, L. Casalena , Y. Chumlyakov MJM and APS. Ferroelastic twin reorientation mechanisms in shape memory alloys elucidated with 3D X-ray microscopy. J Mech Phys Solids [Internet]. 2019;124:897–928. Available from: https://doi.org/10.1016/j.jmps.2018.12.003

180. J. V. Bernier, N. R. Barton UL and MPM. Far-field high-energy diffraction microscopy: a tool for intergranular orientation and strain analysis. J Strain Anal Eng Des [Internet]. 2011;46(7):527–47. Available from: https://doi.org/10.1177/0309324711405761

181. U. Lienert, S. F. Li, C. M. Hefferan, J. Lind, R. M. Suter, J. V. Bernier, N. R. Barton, M. C. Brandes, M. J. Mills, M. P. Miller BJ and WP. High-energy diffraction microscopy at the advanced photon source. JOM [Internet]. 2011;63(70–77). Available from: https://doi.org/10.1007/s11837-011-0116-0

182. J. Oddershede, J. P. Wright, A. Beaudoin GW. Deformation-induced orientation spread in individual bulk grains of an interstitial-free steel. Acta Mater [Internet]. 2015;85:301–13. Available from: https://doi.org/10.1016/j.actamat.2014.11.038

183. N. Y. Juul, G. Winther, D. Dale, M. K. A. Koker PS and JO. Elastic interaction between twins during tensile deformation of austenitic stainless steel. Scr Mater [Internet]. 2016;120:1–4. Available from: https://doi.org/10.1016/j.scriptamat.2016.03.022

184. D. Naragani, M. D. Sangid, P. A. Shade, J. C. Schuren, H. Sharma, J-S. Park, P. Kenesei, J. V. Bernier, T. J. Turner IP. Investigation of fatigue crack initiation from a non-metallic inclusion via high energy x-ray diffraction microscopy. Acta Mater [Internet]. 2017;137:71–84. Available from: https://doi.org/10.1016/j.actamat.2017.07.027

185. R. Pokharel, J. Lind, S. F. Li, P. Kenesei, R. A. Lebensohn RMS and ADR. In-situ observation of bulk 3D grain evolution during plastic deformation in polycrystalline Cu. Int J Plast [Internet]. 2015;67:217–34. Available from: https://doi.org/10.1016/j.ijplas.2014.10.013

186. T. R. Bieler, L. Wang, A. J. Beaudoin PK and UL. In situ characterization of twin nucleation in pure Ti using 3D-XRD. Metall Mater Trans A [Internet]. 2014;45:109–22. Available from: https://doi.org/10.1007/s11661-013-2082-3

187. L. Renversade, R. Quey, W. Ludwig, D. Menasche, S. Maddali RMS and AB. Comparison between diffraction contrast tomography and high-energy diffraction microscopy on a slightly deformed aluminium alloy. Int Union Crystallogr. 2016;3(1):32–42.

188. B. Ghammraoui, V. Rebuffel, J. Tabary, C. Paulus LV and PD. Effect of grain size on stability of X-ray diffraction patterns used for threat detection. Nucl Instruments Methods Phys Res Sect A Accel Spectrometers, Detect Assoc Equip [Internet]. 2012;683:1–7. Available from: https://doi.org/10.1016/j.nima.2012.04.034

189. P. Sittner, O. Molnarova, X. Bian LH and HS. Tensile Deformation of B19’ Martensite in Nanocrystalline NiTi Wires. Shape Mem Superelasticity [Internet]. 2023; Available from: https://doi.org/10.1007/s40830-023-00414-4

190. L. Zheng, Y. He ZM. Investigation on fatigue behaviors of NiTi polycrystalline strips under stress-controlled tension via in-situ macro-band observation. Int J Plast [Internet]. 2017;90:116–45. Available from: https://doi.org/10.1016/j.ijplas.2016.12.008

191. L. Zheng, Y. He ZM. Effects of Lüders-like bands on NiTi fatigue behaviors. Int J

Solids Struct [Internet]. 2016;83:28–44. Available from: https://doi.org/10.1016/j.ijsolstr.2015.12.021

192. A. Bucsek, L. Casalena, D. C. Pagan, P. Paul, Y. Chumlyakov MM and AS. Three-dimensional in situ characterization of phase transformation induced austenite grain refinement in nickel-titanium. Scr Mater [Internet]. 2019;162:361–6. Available from: https://doi.org/10.1016/j.scriptamat.2018.11.043

193. X. Zhang, M. Li, J. Park, P. Kenesei HS and JA. High-energy x-ray diffraction microscopy study of deformation microstructures in neutron-irradiated polycrystalline Fe-9%Cr. J Nucl Mater [Internet]. 2018;508:556–66. Available from: https://doi.org/10.1016/j.jnucmat.2018.06.004

194. T. M. Poletika, S. L. Girsova, A. I. Lotkov ANK and NVG. Structure and Multistage Martensite Transformation in Nanocrystalline Ti-50.9Ni Alloy. Metals (Basel) [Internet]. 2021;11(8):1262. Available from: https://doi.org/10.3390/met11081262

195. Q. Y. Wang, C. Bathias NK and QC. Effect of inclusion on subsurface crack initiation and gigacycle fatigue strength. Int J Fatigue [Internet]. 2002;24(1269–1274). Available from: https://doi.org/10.1016/S0142-1123(02)00037-3

196. O. Molnárová PJ and MC. TEM analysis of deformation bands created by tensile deformation of superelastic NiTi wires. Mater Charact [Internet]. 2020;167(110470). Available from: https://doi.org/10.1016/j.matchar.2020.110470

197. S. Tammas-Williams, P. J. Withers IT and PBP. The influence of prosity on fatigue crack initiation in additively manufactured titanim components. Sci Rep [Internet]. 2017;7(7308). Available from: https://doi.org/10.1038/s41598-017-06504-5

198. I. Kallai, O. Mizrahi, W. Tawackoli, Z. Gazit, G. Pelled DG. Microcomputed tomography–based structural analysis of various bone tissue regeneration models. Nat Protoc. 2011;6:105–10.

199. U. Bonse FB. X-ray computed microtomography (μCT) using synchrotron radiation (SR). Prog Biophys Mol Biol [Internet]. 1996;65(1–2):133–69. Available from: https://doi.org/10.1016/S0079-6107(96)00011-9

200. E. Alarcon, L. Heller, S. A. Chirani, P. Sittner, J. Kopeček LS-S and SC. Fatigue performance of superelastic NiTi near stress-induced martensitic Transformation. Int J Fatigue [Internet]. 2017;95:76–89. Available from: https://doi.org/10.1016/j.ijfatigue.2016.10.005

201. M. Li, J. Wei, L. Ren, Y. Zhao, Z. Shang, D. Zhou, W. Liu, L. Luo XS. Superwetting behaviors at the interface between electrode and electrolyte. Cell Reports Phys Sci [Internet]. 2021;2(3). Available from: https://doi.org/10.1016/j.xcrp.2021.100374

202. P. J. Withers, C. Bouman, S. Carmignato, V. Cnudde, D. Grimaldi, C. K. Hagen, E

Maire, M. Manley ADP and SRS. X-ray computed tomography. Nat Rev Methods Prim [Internet]. 2021;1(18). Available from: https://doi.org/10.1038/s43586-021-00015-4

203. K. Palanikumar, J. P. Davim. 5- Electrical discharge machining: study on machining characteristics of WC/Co composites. In: Machining and machine-tools. Woodhead Publishing Reviews: Mechanical Engineering Series; 2013. p. 135–68.

204. P. Kabirifar, K. Chu, F. Ren QS. Effects of grain size on compressive behavior of NiTi polycrystalline superelastic macro- and micropillars. Mater Lett [Internet]. 2017;214:53–5. Available from: https://doi.org/10.1016/j.matlet.2017.11.069

205. S. QingPing, A. Ahadi LM and CM. Effects of grain size on phase transition behavior of nanocrystalline shape memory alloys. Sci China Press Springer-Verlag Berlin Heidelb [Internet]. 2014;57:671–679. Available from: https://doi.org/10.1007/s11431-014-5505-5

206. X. B. Shi, F. M. Guo, J. S. Zhang HLD and SLC. Grain size effect on stress hysteresis of nanocrystalline NiTi alloys. J Alloys Compd [Internet]. 2016;688B:62–8. Available from: https://doi.org/10.1016/j.jallcom.2016.07.168

207. A. K. Srivastava DS and JVH. Grain growth and precipitation in an annealed cold-rolled Ni50.2Ti49.8 alloy. Intermetallics [Internet]. 2007;15(12):1538–47. Available from: https://doi.org/10.1016/j.intermet.2007.06.003

208. J. Chen HY and QS. Effects of grain size on fatigue crack growth behaviors of nanocrystalline superelastic NiTi shape memory alloys. Acta Mater [Internet]. 2020;195:141–50. Available from: https://doi.org/10.1016/j.actamat.2020.05.008

209. J. E. Schaffer. Structure-Property Relationships in Conventional and Nanocrystalline NiTi Intermetallic Alloy Wire. J Mater Eng Perform [Internet]. 2009;18:582–7. Available from: https://doi.org/10.1007/s11665-009-9369-y

210. B. Xu CY and GK. Phase field study on the microscopic mechanism of grain size dependent cyclic degradation of super-elasticity and shape memory effect in nano-polycrystalline NiTi alloys. Int J Plast [Internet]. 2021;145(103075). Available from: https://doi.org/10.1016/j.ijplas.2021.103075

211. T. Waitz, T. Antretter, F. D. Fischer, H. P. Karnthaler. Size effects on martensitic phase transformations in nanocrystalline NiTi shape memory alloys. Mater Sci Technol [Internet]. 2008;24(8):934–40. Available from: https://doi.org/10.1179/174328408X302620

212. S. Ashbli and C. C. Menzemer. On the Fatigue Behavior of Nanocrystalline NiTi Shape Memory Alloys: A Review. J Nanomed Nanotechnol. 2019;10(2).

213. C. Celada-Casero JS and MJS. The role of the austenite grain size in the martensitic transformation in low carbon steels. Mater Des [Internet]. 2019;167(107625). Available from: https://doi.org/10.1016/j.matdes.2019.107625

214. J. Q. Fonseca and L. Ko. The kinematics of deformation and the development of substructure in the particle deformation zone. IOP Conf Ser Mater Sci Eng. 2015;89(012012).

215. R. D. Jones, F. Di Gioacchino, H. Lim, T. E. J. Edwards, C. Schwalbe, C. C. Battaile WJC. Reduced partitioning of plastic strain for strong and yet ductile precipitate-strengthened alloys. Sci Rep [Internet]. 2018;8(8698). Available from: https://doi.org/10.1038/s41598-018-26917-0

216. Z. G. Voyiadjis and M. Yaghoobi. Chapter 1 - Introduction: Size effects in materials. In: Size Effects in Plasticity, From Macro to Nano. Elsevier Inc; 2019. p. 1–79.

217. W. S. LePage JAS and SHD. Effects of texture on the functional and structural fatigue of a NiTi shape memory alloy. Int J Solids Struct [Internet]. 2021;221:150–64. Available from: https://doi.org/10.1016/j.ijsolstr.2020.09.022

218. X. Bian, L. Heller LK and PS. In-situ synchrotron X-ray diffraction texture analysis of tensile situ synchrotron X-ray diffraction texture analysis of tensile deformation of nanocrystalline NiTi wire in martensite state. Appl Mater Today [Internet]. 2022;26(101378). Available from: https://doi.org/10.1016/j.apmt.2022.101378

219. J. wang, Z. Pan, K. Carpenter, J. Han ZW and HL. Comparative study on crystallographic orientation, precipitation, phase transformation and mechanical response of Ni-rich NiTi alloy fabricated by WAAM at elevated substrate heating temperatures. Mater Sci Eng A [Internet]. 2021;800(140307). Available from: https://doi.org/10.1016/j.msea.2020.140307

220. K. Gall, N. Yang HS and YIC. Fracture of precipitated NiTi shape memory alloys. Int J Fract [Internet]. 2001;109:189–207. Available from: https://doi.org/10.1023/A:1011069204123

221. S. Miyazaki, S. Kimura KO and YS. The habit plane and transformation strains associated with the martensitic transformation in Ti-Ni single crystals. Scr Metall [Internet]. 1984;18(9):883–8. Available from: https://doi.org/10.1016/0036-9748(84)90254-0

222. M. L. Bowers, Y. Gao, L. Yang, D. J. Gaydosh, M. De Graef, R. D. Noebe YW and MJM. Austenite grain refinement during load-biased thermal cycling of a Ni49.9Ti50.1 shape memory alloy. Acta Mater [Internet]. 2015;91:318–29. Available from: https://doi.org/10.1016/j.actamat.2015.03.017

223. H. H. Mulder PET and JB. Anisotropy of the Shape Memory Effect in Tension of Cold-rolled 50.5 Tı 49.2 Ni (at.%) Sheet. Int J Mater Res [Internet]. 1993;84:501–8. Available from: https://doi.org/10.1515/ijmr-1993-840712

224. S. W. Robertson, V. Imbeni H-RW and ROR. Crystallographic texture for tube and plate of the superelastic/shape-memory alloy nitinol used for endovascular stents. J Biomed Mater Res Part A [Internet]. 2006;72:190–9. Available from:

https://doi.org/10.1002/jbm.a.30214

225. L. Lutterotti, R. Vasin HRW. Rietveld texture analysis from synchrotron diffraction images. I. Calibration and basic analysis. Powder Diffr [Internet]. 2014;29:76–84. Available from: https://doi.org/10.1017/S0885715613001346

226. K. S. Ramaiah, A. K. Bhatnagar, R. D. Pilkington AEH and RDT. The effect of sulfur concentration on the properties of chemical bath deposited CdS thin films. J Mater Sci Mater Electron [Internet]. 2000;11:269–77. Available from: https://doi.org/10.1023/A:1008965420050

227. W. Chen, L. Gu, J. han, S. Ge, X. Hua, P. Hu, R. Bai, W. Zhang TC and KW. The Effect of Heat Treatment and Different Degrees of Deformation on the Microstructure and Mechanical Properties of Pure Mo Sheets. Metals (Basel) [Internet]. 2022;12(12):2189. Available from: https://doi.org/10.3390/met12122189

228. J. Q. Cong, F. H. Guo, J. L. Qiao STQ and HJW. Texture Evolution during Recrystallization and Grain Growth in Non-Oriented Electrical Steel Produced by Compact Strip Production Process. Materials (Basel) [Internet]. 2022;15(1):197. Available from: https://doi.org/10.3390/ma15010197

229. P. Barriobero-Vila, G. Requena, S. Schwarz FW. Influence of phase transformation kinetics on the formation of a in a b-quenched Ti–5Al–5Mo–5V–3Cr–1Zr alloy. Acta Mater [Internet]. 2015;95:90–101. Available from: https://doi.org/10.1016/j.actamat.2015.05.008

230. U. Shmueli, H. D. Flack, J. C. HS. Methods of space-group determination. Int Tables Crystallogr. 2016;A:107–31.

231. B. D. Cullity and S. R. Stock. Elements of x-ray diffraction. United Kingdom: Prentice Hall; 2001.

232. C. Yu, J. Lin, P. Huai, Y. Guo, X. Ke, X. Yu, K. Yang, N. Li, W. Yang, B. Sun RX and HX. Structural Phase Transition of ThC Under High Pressure. Sci Rep. 2017;7(96).

233. J. F. Dorrian, R. E. Newnham DKS and MIK. Crystal structure of Bi4Ti3O12. Ferroelectrics [Internet]. 1972;3(1):17–27. Available from: https://doi.org/10.1080/00150197108237680

234. H. Kawada, Y. Fujii, H. Nakao, Y. Murakami, T. Watanuki, H. Suematsu, K. Kikuchi, Y. Achiba II. Structural aspects of C82 and C76 crystals studied by x-ray diffraction. Phys Rev B. 1995;51(14):8723–30.

235. G. Garces, J. Medina, P. Perez, K. Mathis, K. Horvath AS and NS. Influence of quasicrystal I-phase on twinning of extruded Mg-Zn-Y alloys under compression. Acta Mater [Internet]. 2018;151:271–81. Available from: https://doi.org/10.1016/j.actamat.2018.03.060

236. Y. Chen, O. Molnarova, O. Tyc, L. Kaderavek, L. Heller PS. Recoverability of large

strains and deformation twinning in martensite during tensile deformation of NiTi shape memory alloy polycrystals. Acta Mater [Internet]. 2019;180:243–59. Available from: https://doi.org/10.1016/j.actamat.2019.09.012

237. P. Sittner, L. Heller, P. Sedlak, Y. Chen, O. Tyc, O. Molnarova LK and HS. B2→B19→B2T Martensitic Transformation as a Mechanism of Plastic Deformation of NiTi. Shape Mem Superelasticity [Internet]. 2019;5:383–396. Available from: https://doi.org/10.1007/s40830-019-00250-5

238. Y. Chen, O. Tyc, L. Kaderavek, O. Molnarova LH and PS. Temperature and microstructure dependence of localized tensile deformation of superelastic NiTi wires. Mater Des [Internet]. 2019;174(107797). Available from: https://doi.org/10.1016/j.matdes.2019.107797

239. E. Polatidis, M. Šmíd, I. Kuběna, W.-N. Hsu GL and HVS. Deformation mechanisms in a superelastic NiTi alloy: An in-situ high resolution digital image correlation study. Mater Des [Internet]. 2020;191(108622). Available from: https://doi.org/10.1016/j.matdes.2020.108622

240. R. Delville, B. Malard, J. Pilch PS and DS. Transmission electron microscopy investigation of dislocation slip during superelastic cycling of Ni–Ti wires. Int J Plast [Internet]. 2011;27:282–97. Available from: https://doi.org/10.1016/j.ijplas.2010.05.005

241. A. P. Stebner, H. M. Paranjape, B. Clausen LCB and ARP. In Situ Neutron Diffraction Studies of Large Monotonic Deformations of Superelastic Nitinol. Shape Mem Superelasticity [Internet]. 2015;1:252–267. Available from: https://doi.org/10.1007/s40830-015-0015-2

242. D. Lu, Q. Jiang, X. Ma, Q. Zhang XF and LF. Defect-Related Etch Pits on Crystals and Their Utilization. Crystals [Internet]. 2022;12(11):1549. Available from: https://doi.org/10.3390/cryst12111549

243. S. Gall, J. Berghold, E. Conrad, P. Dogan, F. Fenske, B. Gorka, K. Lips, M. Muske, K. Petter, B. Rau JS and IS. Large grained polycrystalline silicon on glass for thin film solar cells. In: 21st European Photovoltaic Conference and Exhibition. Dresden, Germany; 2006. p. 1091–4.

244. G. S. Pandolfi, S. C. Martins VTLB and LAS. Precipitation kinetics of Ti3Ni4 and multistage martensitic transformation in an aged Ni–rich Ni–Ti shape memory alloy. J Mater Res Technol [Internet]. 2020;9(4):9162–73. Available from: https://doi.org/10.1016/j.jmrt.2020.06.046

245. J. Zhu, H. H. Wu, Y. Wu, H. Wang, T. Zhang, H. Xiao YW and SQS. Influence of Ni4Ti3 precipitation on martensitic transformations in NiTi shape memory alloy: R phase transformation. Acta Mater [Internet]. 2021;207(116665). Available from: https://doi.org/10.1016/j.actamat.2021.116665

246. N. S. Moghaddam, S. Saedi, A. Amerinatanzi, A. Hinojos, A. Ramazani, J. Kundin, M. J. Mills HK and ME. Achieving superelasticity in additively manufactured NiTi in compression without post-process heat treatment. Sci Rep [Internet]. 2019;9(41). Available from: https://doi.org/10.1038/s41598-018-36641-4

247. M. E. Mitwally, M. Farag. Effect of cold work and annealing on the structure and characteristics of NiTi alloy. Mater Sci Eng A [Internet]. 2009;519(1–2):155–66. Available from: https://doi.org/10.1016/j.msea.2009.04.057

248. C. Yu, G. Kang QK. A physical mechanism based constitutive model for temperature-dependent transformation ratchetting of NiTi shape memory alloy: One-dimensional model. Mech Mater [Internet]. 2014;78:1–10. Available from: https://doi.org/10.1016/j.mechmat.2014.07.011

249. Novak PS and V. Anisotropy of martensitic transformations in modeling of shape memory alloy polycrystals. Int J Plast [Internet]. 2000;16(10–11):1243–68. Available from: https://doi.org/10.1016/S0749-6419(00)00009-7

250. W. C. Crone HB and AC. Nanoindentation and Microindentation of CuAlNi Shape Memory Alloy. Exp Mech [Internet]. 2007;47:133–142. Available from: https://doi.org/10.1007/s11340-006-8884-0

251. C. Elibol and M. F. Wagner. Virtual Extensometer Analysis of Martensite Band Nucleation, Growth, and Strain Softening in Pseudoelastic NiTi Subjected to Different Load Cases. Mater. 2018;11(8):1458.

252. V. Srivastava and M. Gupta. Impact of Post Hardening Mechanism on Self-Healing Assessment of AA2014 Nitinol-Based Smart Composites. Met Mater Int [Internet]. 2021;27:2666–2681. Available from: https://doi.org/10.1007/s12540-020-00630-y

253. P. Sedmak, P. Sittner JP and CC. Instability of cyclic superelastic deformation of NiTi investigated by synchrotron X-ray diffraction. Acta Mater [Internet]. 2015;94:257–70. Available from: https://doi.org/10.1016/j.actamat.2015.04.039

254. S. Daly, D. Rittel KB and GR. Large Deformation of Nitinol Under Shear Dominant Loading. Exp Mech [Internet]. 2009;49:225–233. Available from: https://doi.org/10.1007/s11340-008-9178-5

255. S. D. Leonardo GP and GB. Standard mechanical testing is inadequate for the mechanical characterisation of shape-memory alloys: Source of errors and a new corrective approach. Mater Des [Internet]. 2022;216(110538). Available from: https://doi.org/10.1016/j.matdes.2022.110538

256. Y. H. Lu LJQ and WYC. In situ study of martensitic transformation and nucleation and propagation of cracks in Cu-Ni-Al shape memory alloy. Mater Sci Technol [Internet]. 2002;18(3):273–8. Available from: https://doi.org/10.1179/026708301225000716

257. N. Nayan VB and UR. Effect of mechanical cycling on the stress–strain response of

a martensitic Nitinol shape memory alloy. Mater Sci Eng A [Internet]. 2009;525(1–2):60–7. Available from: https://doi.org/10.1016/j.msea.2009.07.038

258. S. Maheshwari, Y. Li NA and MJJ. Chapter Three - Density functional theory models for electrocatalytic reactions. Adv Catal [Internet]. 63AD;2018:117–67. Available from: https://doi.org/10.1016/bs.acat.2018.10.003